eman ta zabal zazu

Universidad del País Vasco
Euskal Herriko Unibertsitatea

Ferritin-based Hybrid Nanocomposites for Enzyme-mimetic Catalytic Activity

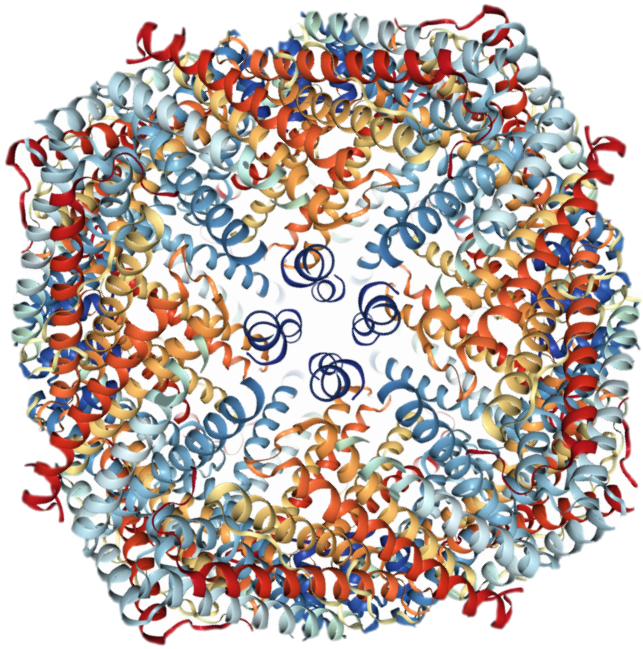

Unai Carmona Igartua

PhD Thesis

Supervisor: Mato Knez

2017

This thesis has been carried out at:

CIC nanoGUNE Consolider

Nanomaterials group

Laburpena

Biomaterialek funtsezko eginkizunak betetzen dituzte nanozientziaren esparruan, prozesu biologikoetan parte hartzen duten molekulek eta bio-egiturek eskala nanometrikoa dutelako. Beraz, ez da harritzekoa nanozientziatik abiatutako biomaterialak erabiltzea konposatu berrien ingenieritzan zein funtzionalitate berriak helburu dituzten ikerketetan.

Entzimen imitazioa susperraldian dagoen ikerketa lerroa da biologian inspiratutako nanozientzian. Honek material berriak aztertzea du helburu, batez ere entzimen katalizatzaile funtzioa imitatu edo simulatu dezaketeenak. Entzimak oso eraginkorrak dira ingurune biokimikoetan, baina industria produkzioa bezalako prozesu exijenteetan alternatiba egonkor eta eraginkorrak behar dira. Zentzu horretan nanopartikula inorganikoen eta proteinen arteko bateraketatik sortutako konposatu hibridoek eraldaketa katalitikorako beharrak bete ditzakete.

Ferritina naturan kopuru handitan eskuragarri dagoen nanometroen eskalako biomateriala da. Berau zeluletako burdinaren metabolismoko funtsezko proteina bat da eta bi funtzio nagusi ditu: burdina garraiatzea eta burdina gorde eta metatzea. Ferritina proteinak 24 azpiunitatez osatutako esfera forma du; kanpo diametroak 12 nm dituelarik eta barruan 8 nm-ko barrunbe hutsa duelarik. Naturan barrunbe hau burdina gordetzeko erabiltzen da, ferrihidrita mineral moduan. Burdinarik gabeko ferritinaren kapsulari apoferritina deritzo. Giza apoferritina bi azpiunitate ezberdinez osaturik dago, funtzionalitate bereiztuekin: H-katea (ingelesezko heavy chain) proteinak ferroxidasa aktibitatea du; L-katea (ingelesez light chain) proteinak aldiz, burdinaren nukleazioan lagundu eta mineralizazioa errazten du.

Apoferritinaren egitura nanozientziako zenbait aplikaziotan erabiltzeko aztertua izan da; horien artean dira sendagaien askatze kontrolatua, entzimen imitazioa edo nanopartikulen sintesia.

Ferritina oinarri duten nanokonposatuak sortzeko bi bide nagusi daude (I. irudia); batetik metalezko nanopartikulak osatzeko erabiltzen dena, inkubazio zuzena deritzona. Metal ioiak apoferritinaren barnera sartzen dira inkubazioan zehar, eta proteinaren purifikazioaren ondoren, apoferritina barnean gelditutako ioiak erreduzituz partikulak osatzen dira. Bestetik, bigarren metodoa aurrez sortutako nanopartikulak edo sendagaiak enkapsulatzeko erabiltzen da. Teknika hau pH-aren aldaketan oinarritzen da. pH 2-an ferritina desegituratu egiten da eta une horretan enkapsulatu nahi den konposatuarekin kontaktuan jartzen da. Azkenik, pH-a 7-8 ra igoz ferritinak bere oinarrizko egitura hartzen du, barruan partikula-zein sendagaiak harrapatuz.

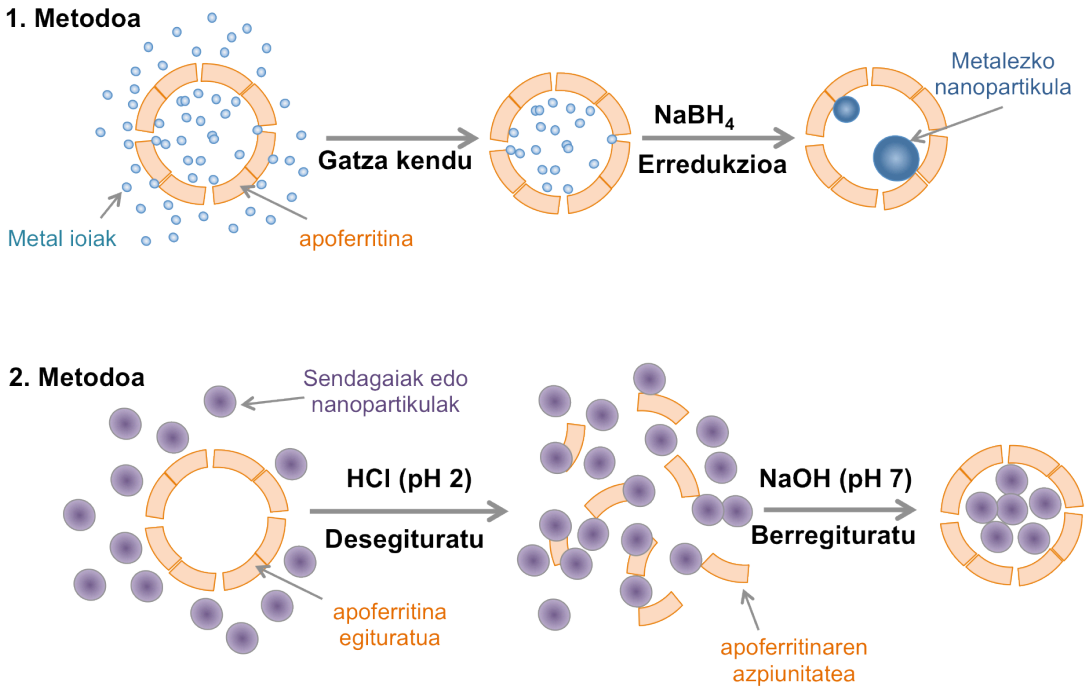

I. irudia. Enkapsulaziorako bi prozesuren irudi eskematikoa. 1. Metodoa: metal ioien eta apoferritinaren arteko inkubazio zuzen bidezko sintesia. 2. Metodoa: pH-aren aldaketak eragindako proteinaren desegite eta berregituraketaren bidezko sintesia.

Orokorrean, sortutako nanokonposatu berri hauen funtzionalitatea ferritina barruan dagoen konposatuak emandakoa izango da. Era honetan, erresonantzia magnetiko bidezko irudigintzan erabiltzen diren manganeso edo gadoliniozko kontraste agenteak sortu daitezke edo doxorrubicina edo cisplatin bezalako minbiziaren kontrako sendagaiak enkapsulatu.

Tesi honetan ferritina naturala eta sintetikoa hiru ikuspuntu ezberdinetatik aztertu dira. Lehenengo, ferritina barruan sintetizatutako nanopartikulen aktibitate katalitikoa ikertu da. Gero, enkapsulatutako platinozko nanopartikulen ferroxidasa aktibitate bioinorganikoa eta biomineralizazioan duten eragina aztertu da. Azkenik, ferritina proteinaren propietate intrintsekoak ikertu dira, horretarako redox erreakzio bat erabiliz.

Hasteko, apoferritina barruan sintetizatutako platinozko nanopartikulen (Pt-apo) aktibitate katalitikoa karakterizatu da, arreta berezia jarriz katalasa eta superoxido dismutasa (SOD) entzimen aktibitatearen imitazioan. Aurretik nanokonposatuak erakutsitako aktibitateak, 3-amino-1,2,4-triazole (3AT), NaN_3 (A inhibitzailea) eta Hg^{2+} inhibitzaileak erabiliz nola aldatzen diren aztertu da. 3AT inhibitzaileak (B inhibitzailea) bi erreakzioak inhibitzeko gaitasuna erakutsi du, NaN_3-ak berriz soilik katalasa inhibitzekoa. Era honetan modu selektiboan bi erreakzioetako baten inhibizioa lortu da bestea aktibo mantentzen den bitartean. Azkenik, erredukzio agenteen bidez, nanopartikulen gainazalaren egitura kimiko eta funtzionala itzulkorra eta iraunkorra dela frogatu da (II. irudia).

Bestetik, apoferritina barruan sintetizatuko urrezko nanopartikulen (Au-apo) eta merkurio ioien (Hg^{2+}) arteko elkarrekintza karakterizatu da. Bi konposatuen elkarrekintzaren ondorioz, katalasaren imitazioan inaktiboa zen urrea aktibatzea lortu da. Ondoren, urrearen gain izandako eragina hobeto aztertzeko urrezko nanopartikulak erabili dira antzeko aktibazioa ikusiz. Behaketa garrantzitsu hau ingelesezko *sputter* teknikaren bidez jarritako urrezko gainazal mehekin esperimentatuz karakterizatu da. Urrezko nanopartikula eta gainazaletan aztertutakoa erabiliz, erreakzio mekanismo bat proposatu da.

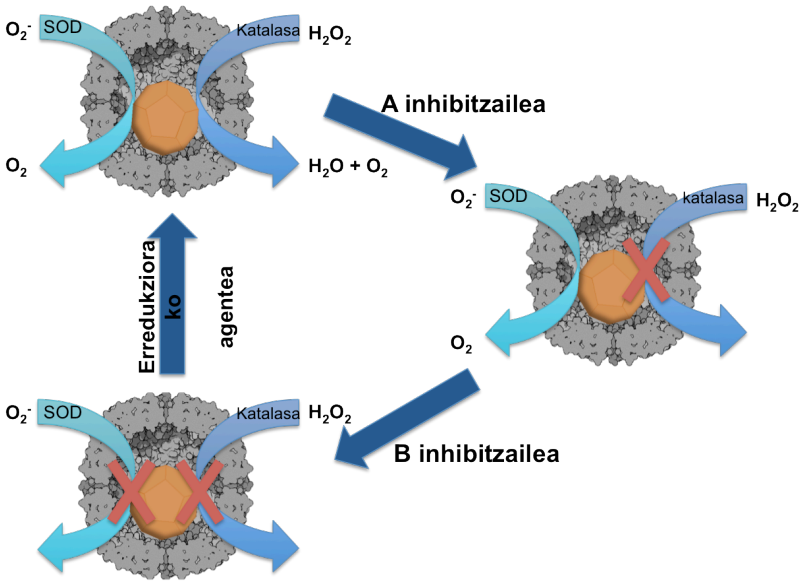

II. irudia. Pt-apo konposatuaren aktibitate katalitikoa eta honen inhibizioa irudikatzeko erabilitako eskema.

Aurretiko bi entzimen imitazioaz gain, enkapsulatutako platinozko nanopartikulen ferroxidasa aktibitate bioinorganikoa ikertu da. Ferroxidasa aktibitaterik gabeko L-kateez osatutako apoferritina homopolimerikoetan sintetizatutako platinozko nanopartikulek ferroxidasa aktibitatea izatea lortzen du. Aktibitate hau platinozko nanopartikuletatik datorren arren, ferritina naturala bailitzan burdina mineralizatzea lortu da.

Ferritinaren proteinetan arreta jarriz, L-kate proteinikoaren ezaugarri intrintseko bat identifikatu eta karakterizatu da, redox erreakzio bat erabiliz. Ferritinaren barruan gertatzen den burdinaren oxidazioa, ferritinaren kanpoan gertatzen den zitokromo c-ren erredukzioarekin lotzea lortu da. L-kateak ez du inolako ferroxidasa aktibitaterik eta beraz ezin du burdina oxidatu; bestetik, H-kate proteinikoak ferroxidasa aktibitatea duen arren, ezin du zitokromo c erreduzitu. L- eta H- kateez osatutako ferritinak soilik izan du zitokromo c-ren erredukzio eraginkorrerako gaitasuna. Azkenik, L-kateak elektroiak eroateko duen gaitasuna bi norantzatan doala frogatu da (III. irudia). Aurkikuntza berri honek ferritinaren inguruan aurrerantzean egingo diren ikerketa biokimikoetarako garrantzi berezia izango du.

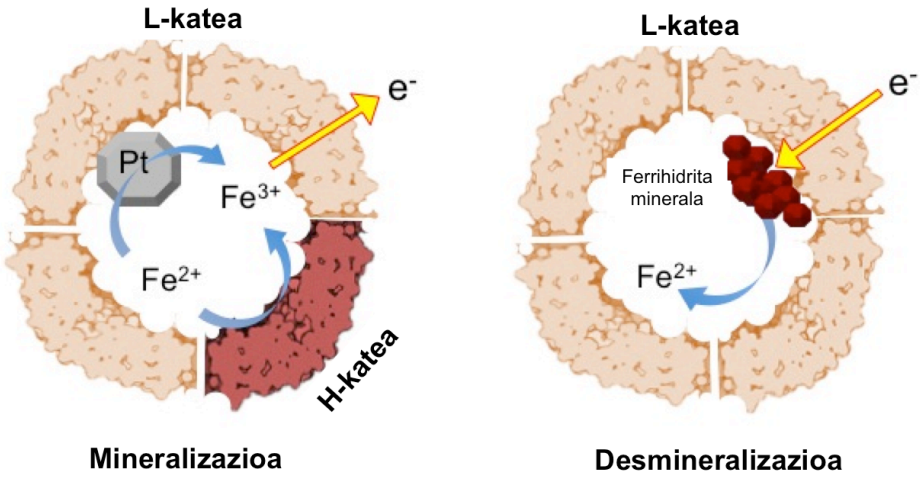

III. irudia. L-kate proteinikoaren ezaugarri intrintseko bat identifikatzeko egindako erreakzioen irudi eskematikoa.

Bukatzeko, uhin luzeera ezberdinetako LED argiak erabiliz, ferritinaren mineralaren desmineralizazioa aztertu da. Kasu honetan, energetikoena den argi urdinak soilik lortu du ferritina barruan ferrihidrita minerala desmineralizatzea. Zelularen metabolismorako burdina funtsezko elementua dela jakinda, argi urdinaz irradiatutako zelulen bideragarritasunean izandako jaitsiera desmineralizazio honen ondorioz izan daitekeela proposatu da.

Abstract

Biomaterials play a crucial role in nanoscience, not at least because many processes in biology involve molecules and assemblies on the nanometre scale. Therefore it is not astonishing that numerous approaches in nanoscience make use of biomaterials with the aim to engineer novel composites with novel or improved functionalities.

One emerging research direction in bio-inspired nanoscience is enzyme mimetics, which studies materials that are able to imitate or simulate the catalytic functionality of enzymes. Even though enzymes are very efficient in a biochemical environment, high-throughput processes, such as industrial production, have a higher demand on efficiency and stability and therefore alternative materials will be appreciated. A combination of inorganic nanomaterials with proteins may be a pathway to satisfy this demand in case these new hybrid materials can fulfil the needs of catalytic conversion.

One biomaterial on the nanoscale, which is naturally available in great amounts, is ferritin. It is a protein essential for the iron metabolism of cells and acts as iron transport and storage unit. The protein is a spherical assembly of 24 subunits with an outer diameter of 12 nm and an internal cavity of around 8 nm. This cavity is naturally used for storage of iron in form of ferrihydrite. The ferritin capsule without embedded iron is called apoferritin. Human apoferritin may consist of two different types of subunits with different functionalities, the heavy chain (H-chain) protein with ferroxidase activity and the light chain (L-chain) protein that promotes the nucleation of iron and the mineral formation.

Apoferritin has been studied for various applications in nanoscience, including drug delivery, enzyme mimetics or as template for nanoparticle growth.

In this thesis natural and synthetic hybrid ferritin are studied from three different perspectives:

On the one hand the catalytic activity of platinum nanoparticle-apoferritin nanocomposites (Pt-apo) is characterized with specific focus on the activities mimicking catalase and superoxide dismutase (SOD). The possibility of tuning the activities with a variety of inhibitors and the possibility to selectively inhibit one of the two reactions are investigated.

On the other hand the interaction of gold nanoparticles encapsulated within apoferritin (Au-apo) with mercury ions (Hg^{2+}) is characterized. Here, a very interesting observation is that such interaction activates the catalase mimicking activity of gold, which without mercury is not present. Based on experiments on thin gold films, a mechanism for the catalytic reaction is proposed.

As a further enzyme mimicking reaction, the bioinorganic ferroxidase activity of encapsulated platinum nanoparticles is studied. After encapsulation of platinum nanoparticles specifically within homopolymeric L-chain apoferritin, the resulting hybrid nanoparticle gains ferroxidase activity and becomes able to mineralize iron in a similar way natural ferritin does.

With view on the ferritin protein, a new intrinsic property of the ferritin L-chain protein is identified and characterized. By separating the redox reaction of iron oxidation and reduction of Cytochrome C (Cyt-c) with either of the two H-chain or L-chain proteins, it was identified that only the L-chain assembly allows for an efficient reduction of Cyt-c and in consequence conduction of electrons. This new finding is considered being of importance for future investigations of biochemical processes in nature that involve ferritin.

Finally, the demineralization of the ferritin mineral induced by illumination with light with various wavelengths is characterized. Here, it was identified that the highly energetic blue light can promote demineralization of the ferrihydrite inside ferritin. With iron being essential for the cellular metabolism, the

demineralization effect may serve as explanation for the viability decrease in cell cultures once those are exposed to blue light.

Contents

Dabilen harriari goroldiorik ez

Chapter 1

Introduction

1.1. Bio-inspired nanotechnology

Biomimetic research imitates and simulates the main principles from nature [1]. The objectives of such research are to create new knowledge for engineering new materials, which will offer new solutions for industry in response to environmental issues or medication [2–4]. Such research witnesses rapid development over the past decades, promising a bright future for both systematics and materials [5].

The characterization of biomaterials and their modification are key issues for any bio-inspired research [6]. With this respect, protein based compounds or natural hybrid materials are in the focus of most of those studies [7,8]. Proteins, lipids, nucleic acids or carbohydrates are among those bio-compounds that can be further engineered in order to tune their functionality or even introduce new functionalities. In principle, most biomaterials can be termed nanomaterials due to their size, since the definition of nanomaterials refers to at least one dimension being below 100 nm [9].

Nanoscience and nanotechology emerged from scientific contributions of several disciplines including, engineering, physics, biology, chemistry and materials science. The main prospect of such research is to gain access to physical or chemical properties of nanomaterials, which are different than the properties of the same material in its macroscopic shape or in bulk. Herein,

biomaterials play an important role for their complex functionalities and great application potential.

The chemistry of each biomolecule has an enormous impact on its functionality. In bio-based nanoscience researchers further adapt the functionalities of biomolecules for certain target applications. Most important examples include:

- **Lipids.** They have an amphiphilic nature and are able to self-assemble. In nature they form cell membranes or membranes for further organelles or sub-cellular structures, like mitochondria or nuclei. In the past decades, natural assembly principles were adapted and various types of liposomes and carriers for drug delivery were developed [10] (Figure 1.1 A and Figure 1.1 B).

- **Proteins.** Those are polypeptide chains that perform functions crucial for life, for example transport or catalysis. Catalytically active proteins are named enzymes. Modifications of proteins allow for their use as carriers in drug delivery systems [7,11,12] or as alternative and improved enzyme substitutes, termed enzyme mimics [13] (Figure 1.1 C and Figure 1.1 D).

- **Sugars or carbohydrates** are typically parts of larger constructs, namely biopolymers named polysaccharides. In nature they often bind to proteins and in this way become constituting parts of glycoproteins. Often, they are involved in signalling. Technologically they are used to modify the surface of diverse nanomaterials for changing their wetting properties, or to modify the surface chemistry of a material, adding functionalities to bind further molecules [14] or particles [15] (Figure 1.1 E and Figure 1.1 F).

- **Nucleic acids** are biopolymers formed by nucleotides, which consist of three components: sugars, phosphate groups and nitrogenous bases. The main function of those biomolecules is to encode and store information about the construction and composition of any cell of any life form. Designing of sequences of nucleotides nowadays enables constructions of three-dimensional nano-scale structures [16] or a variety of approaches towards devices for disease detection [17,18] (Figure 1.1 G and Figure 1.1 H).

The functionality of biomolecules is essential for life. Very often the functionality of biomolecules is linked to metals [19]. Typical examples include oxygen transport by the iron in haemoglobin [20], control of the ionic and osmotic pressure of cells by sodium ions [21], etc. The metal ion usually does not act in its free form. In most of the cases it is bound to organic compounds to form cofactors for proteins.

The fraction of metals compared to the organic fraction in such cases is very low. Nevertheless the combination of both adds great value to the functionality of the material, which encouraged numerous researchers to mimick such materials and to study new functional biocomposites [22].

With regard to those research trends, the present thesis is built upon two main pillars. On one hand, metal-protein (ferritin) compositions are investigated for their catalytic functionalities and on the other hand, the biomolecule, more specifically the ferritin protein, is screened for its functionalities beyond the ones known from literature.

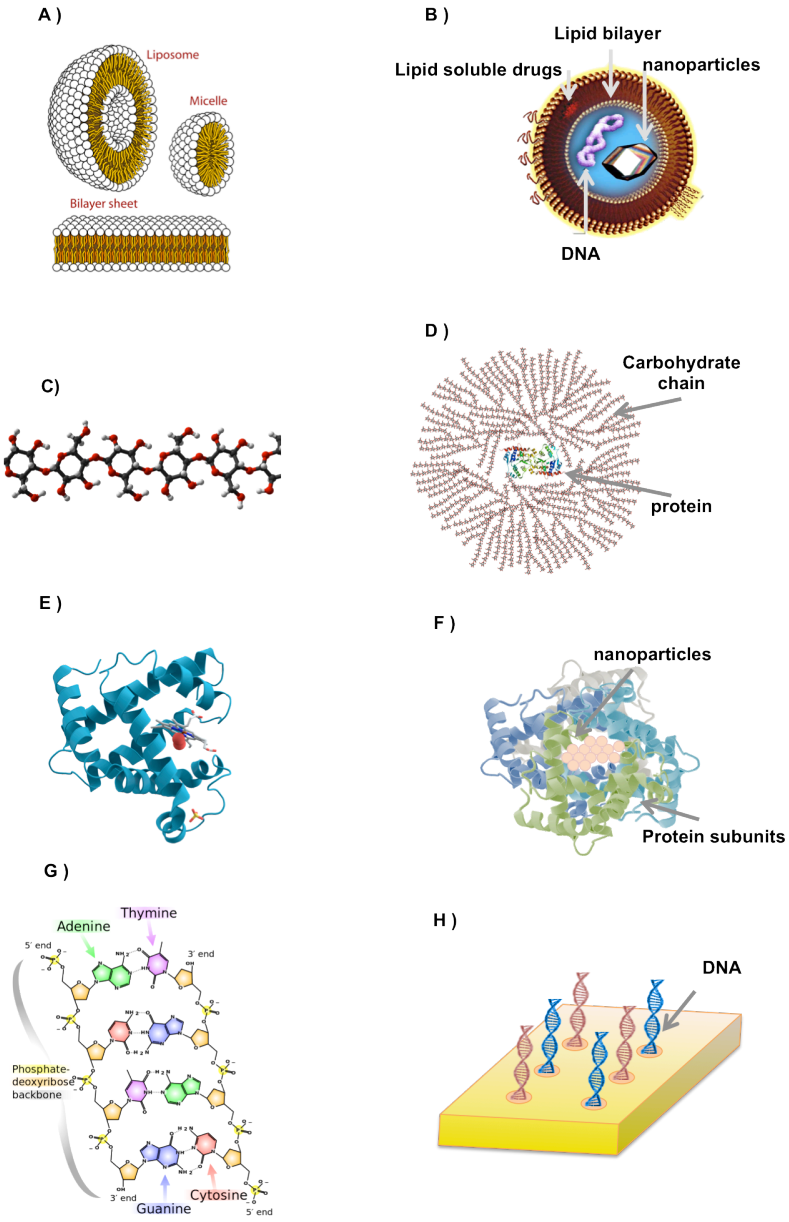

Figure 1.1. Biomaterials used in various applications in nanoscience. A) Lipids in 3 different sizes and shapes [23]. B) Functionalized liposome [24]. C) Carbohydrate chain [25]. D) Carbohydrate cage [26, 27]. E) Protein [28]. F) Protein covering a nanoparticle [29]. G) Deoxyribonucleic acid (DNA) sequences [30]. H) Immobilized DNA [31].

1.2. Proteins: (apo)ferritin

Within the large group of organic biomolecules, proteins fulfil a very important role in any biochemical process. The structure and composition of proteins is very specific for the function they are supposed to have. Before going into detail with the functions or applicability of proteins, their structure or composition should be defined first [32].

Proteins are biopolymers that are composed of monomeric units called amino acids. In eukaryotic organisms 20 different natural amino acids were identified. Amino acids are organic molecules with terminal amine ($–NH_2$) and carboxylic (-COOH) groups, a functional group R that differentiates the amino acids form each other and defines its chemical properties. The molecular fraction R can be $-CH_2$ in Glycine, or a substituted –CHR with more complex organics such as a variety of polar or non-polar, charged or uncharged substituents in the further 19 amino acids (Figure 1.2 A).

For proteins four hierarchical levels of structuring are identified. The primary structure is reflected in the sequence of amino acids. Conventionally, the sequence is described with abbreviated letters representing each of amino acid, starting from the N-terminal group and ending with the C-terminal group. The chemical bond between the amino acids is called peptide bond and is formed between the carboxylic acid group of one amino acid and the amine group of another one (Figure 1.2 B and Figure 1.2 C).

The secondary structure is given by the conformation the protein chain forms. It is resulting from intramolecular interactions between amino acids. Two types of structures are common, α-helixes (Figure 1.2 D) and the β-sheets (Figure 1.2 E), which are arranged and stabilized by folding of the proteins and formation of H-bonds between amino acids in proximity to each other. The tertiary structure is formed by formation of additional H-bonds, disulphide bridges or ionic interactions within the same protein chain and comprises the third dimensionality to a protein (Figure 1.2 F).

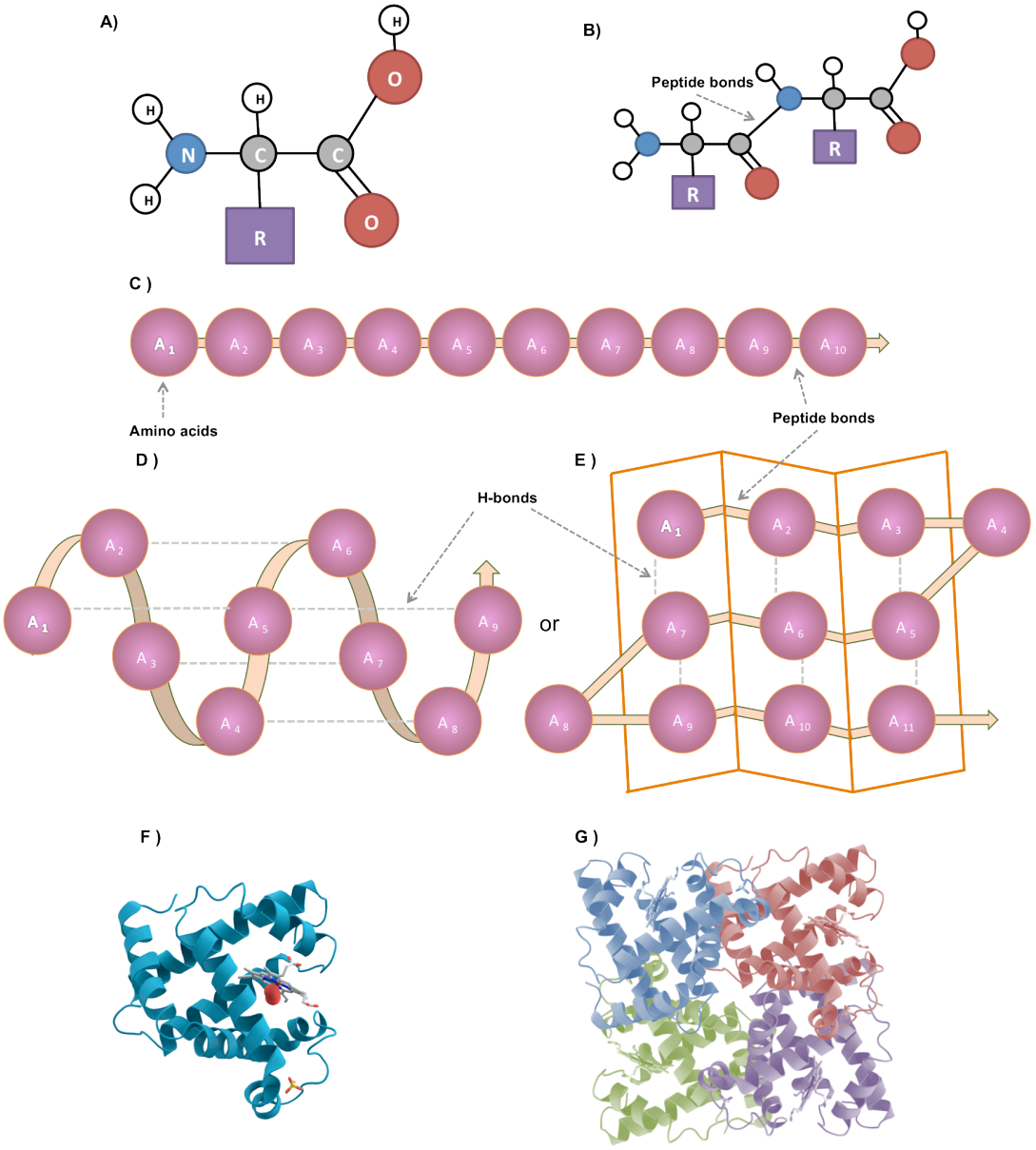

Figure 1.2. Hierarchical levels of the protein structure. A) General structure of an amino acid. B) Peptide bond. C) Primary structure: Amino acid sequence. D) Secondary structure: α-helix. E) Secondary structure: β-sheet. F) Tertiary structure of the protein [28]. G) Quaternary structure: assembly of proteins.

In the last hierarchical level, several protein chains or multiple folded protein subunits can assemble to form protein aggregates with more complex three-dimensional structures. This last level is called the quaternary structure (Figure 1.2 G).

As mentioned above, proteins fulfil a variety of functions including catalysis, signalling, transport or storage of materials [33]. Ferritin is one of such proteins responsible for storage and transport of iron and will be described in more detail.

Ferritin is a spherical protein that is ubiquitous in any kind of life [34]. It is composed of 24 self-assembled subunits. The amino acid sequence of the subunits varies for different organisms, but they maintain a homology in the secondary, tertiary and quaternary structure.

The assembled 24 proteins are forming a spherical structure with an outer diameter of 12 nm and an inner cavity of around 8 nm [35], which can store iron in form of the mineral ferrihydrite. The empty protein sphere is called apoferritin, while the iron-containing sphere is called ferritin. Specifically the human apoferritin protein cage is formed by two slightly differing types of subunits, the heavy chain (H-chain) and the light chain (L-chain) proteins [36]. The ratio of the two subunits within the sphere depends on the organs where the ferritin is located (Table 1.1).

Table 1.1. Percentage of the H- and L-chain subunits within ferritin from various tissues [37].

Ferritin location	**Horse spleen**	**Human spleen**	**Human liver**	**Human heart**	**Human serum**
H-chain	8	10	50	90	0
L-chain	92	90	50	10	100

The sequence homology within the two proteins is around 55 % and the main difference applies to outer and inner surfaces and their functional applicability [38]. At the touching points of the subunits in the apoferritin sphere, characteristic channels are formed. Eight of those are hydrophilic and are located in the threefold symmetry axes. Further six hydrophobic channels are located in the fourfold symmetry axes [39,40].

The two subunits have some functional differences. The most significant difference is that the H-chain protein can bind to two Fe^{2+} ions and catalyze their oxidation to Fe^{3+}, which is subsequently stored as ferrihydrite inside the protein sphere [39,41]. This ferroxidase active site is present in H-chain protein, but not in the L-chain protein. In contrast, the L-chain protein induces the formation of ferrihydrite having a specific nucleation site for the mineral [42]. The iron mineralization process is necessary for effective iron storage inside ferritin and is a critical step in the iron metabolism.

1.3. Iron, iron metabolism and Ferritin

Iron is essential for most living organisms and cells [43], enabling oxygen transport, catalysis or DNA synthesis [44]. Due to its versatile coordination chemistry and redox activity, iron contributes in various ways to biochemical processes.

In excess, however, iron becomes potentially hazardous for cells. It catalyzes the formation of reactive oxygen species (ROS) via the Fenton reaction [45] (Equation 1.1.), which then induce oxidative stress on cells [45]. In the metabolism, iron appears in two distinct oxidation stages, the ferric iron (Fe^{3+}), which is less reactive and more stable, but at the same time not soluble and difficult to be absorbed, and the ferrous iron (Fe^{2+}), which is soluble, but more reactive [46]. This makes the iron acquisition, use and release a very complex biochemical process [47].

Equation 3.1: Fenton reaction

$$(1) \qquad Fe^{2+} + H_2O_2 \rightarrow Fe^{3+} + OH^- + OH^{\cdot}$$

The iron metabolism in the cells has been intensively studied for decades [48]. The individual steps from the dietary uptake to the utilization in various cellular processes have been investigated in depth, but still the mechanism for many processes is not fully resolved [49]. Generally, two types of cells should be distinguished in the iron metabolism; cells that uptake iron from intestinal lumen in the duodenum [46] (first part of the intestine in which iron is directly absorbed) and cells that uptake iron through transferrin [50]. In both of those cases, specific facilitating proteins or organelles are needed. Following proteins or organelles are involved in the iron metabolism:

- **Transferrin (Trf)** is a serum glycoprotein with 80 kDa molecular weight and two specific sites for ferric ion binding. Its main role is to first bind the iron in the vicinity of the cells in the *duodenum* or red blood cell recycling macrophage and to transport the iron to tissues with extensively dividing cells or any other cells in need of iron [51–53].

- **Transferrin receptor** is formed by two monomers of 760 amino acids each. It is located in the cell membrane and has an intracellular region, a transmembrane domain (the brighter part in the representation Figure 1.3) and an extracellular part. Its main function is to bind the Trf, with each monomer of the extracellular glycosylated part being able to bind one Trf. Once bound, the iron will be internalized by endocytosis. In a similar way as Trf, ferritin proteins can also bind to the receptor and become internalized [52–54].

- **Ferroportins** are proteins located in the cell membrane and are part of the family of transmenbrane proteins. Their main function is to transport iron from the inside to the outside of a cell. They play an essential role in duodenal cells being able to release iron, to reduce the internal iron release and to make iron available for its distribution to other cells by Trf [55,56].

- **Ferritin** is a protein constituted by 24 subunits. Its main function is to store iron. It is able to oxidize iron, to internalize it into cells and reduce the generation of ROS that are generated by the excess of the intracellular iron reacting with H_2O_2 via the Fenton reaction [34].

- **Mitochondrion** is an organelle that acts as energy supplier for the cells. It is responsible for the formation of haeme cofactors [57].

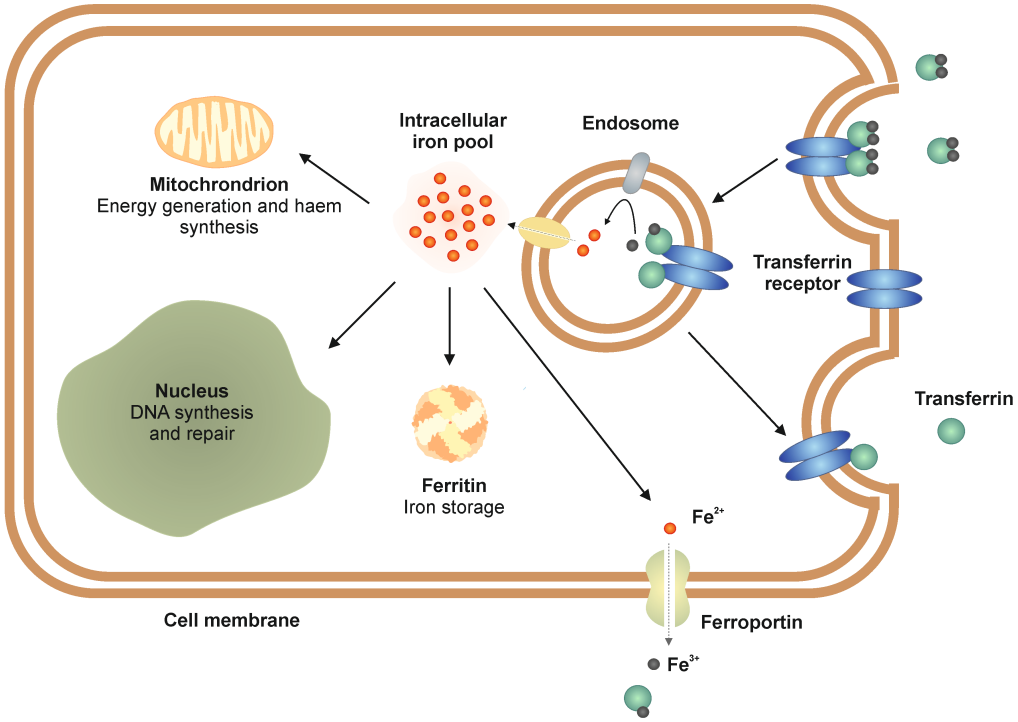

Figure 1.3. Simplified schematic overview of the iron metabolism within a cell.

The iron metabolism is illustrated in Figure 1.3 in a simplified form. In this metabolism ferritin requires an effective biomineralization process to store the excess of iron inside the apoferritin in form of the ferrihydrite [58].

1.3.1 Ferritin Biomineralization

The mineralization process consists of two mains steps. Initially, Fe(II) enters the ferritin. Once inside, the oxidation and nucleation of iron occur and the ferrihydrite nanoparticle is formed [59].

The most likely pathway for the uptake of iron by the ferritin is diffusion through the channels at the 3-fold symmetry axes. Those channels are hydrophilic and possess some specific amino acids with carboxylated residues [60], which form a charge gradient to allow transport of iron ions [61,62].

Inside the protein, the Fe^{2+} ions will become oxidized [63] and nucleation of the ferrihydrite will occur. Two ways have been identified for this process.

- Iron will be oxidized by oxygen at the H-chain ferroxidase site. The resulting Fe^{3+} will migrate to the nucleation sites at the L-chain subunits to nucleate and precipitate [63–65].
- The other pathway involves the surface of the mineral core. In this process both the oxidation and the nucleation will take place at the surface of the ferrihydrite mineral. This process is faster than the previous, but requires an initial formation of the mineral [66].

1.3.2 Demineralization

The iron within the protein is stored as a particle, but the cells cannot use the iron-containing mineral directly. To make the iron available, a process reverse to the biomineralization, the demineralization process, is required. Fe^{3+} is highly insoluble, thus a reduction to Fe^{2+} is required before the release [67]. This iron reduction occurs at the surface of the mineral core and the reduced iron is released upon chelation. This method is proposed and well described in the review article of R. Watt et al [67].

The demineralization process can vary depending on the environmental conditions. Also external factors can influence the demineralization process, for example, ultraviolet light or ionizing laser pulses can be used for iron reduction and demineralization [12,67].

1.4. Ferritin in nanoscience

Besides the described biological functions of storage and transport of iron, ferritin can also be used for many other purposes [68,69]. The inner cavity of

8 nm in diameter, the permeation channels and its ability to be disassembled and reassembled simply by varying the pH make ferritin an excellent tool for many investigations in nanoscience [70,71]. Ferritin is equally suitable as template for nanoparticle synthesis and as carrier for controlled drug delivery.

There are two common routes for the synthesis of ferritin-encapsulated compounds, either through direct incubation or through pH-mediated disassembly and reassembly.

The direct incubation technique is inspired by the iron biomineralization process within the ferritin [72], where apoferritin is incubated with metal salt solutions. In a similar way to the natural process, the metal is internalized through the hydrophilic channels. Typically, the metal ions inside the apoferritin require an additional reducing agent like $NaBH_4$ or H_2 to nucleate and form a nanoparticle. The reaction conditions define the composition of the nanoparticle being either a metal [73,74], metal oxide [75] or further compounds like sulphides [76], etc (Figure 1.4 Method 1).

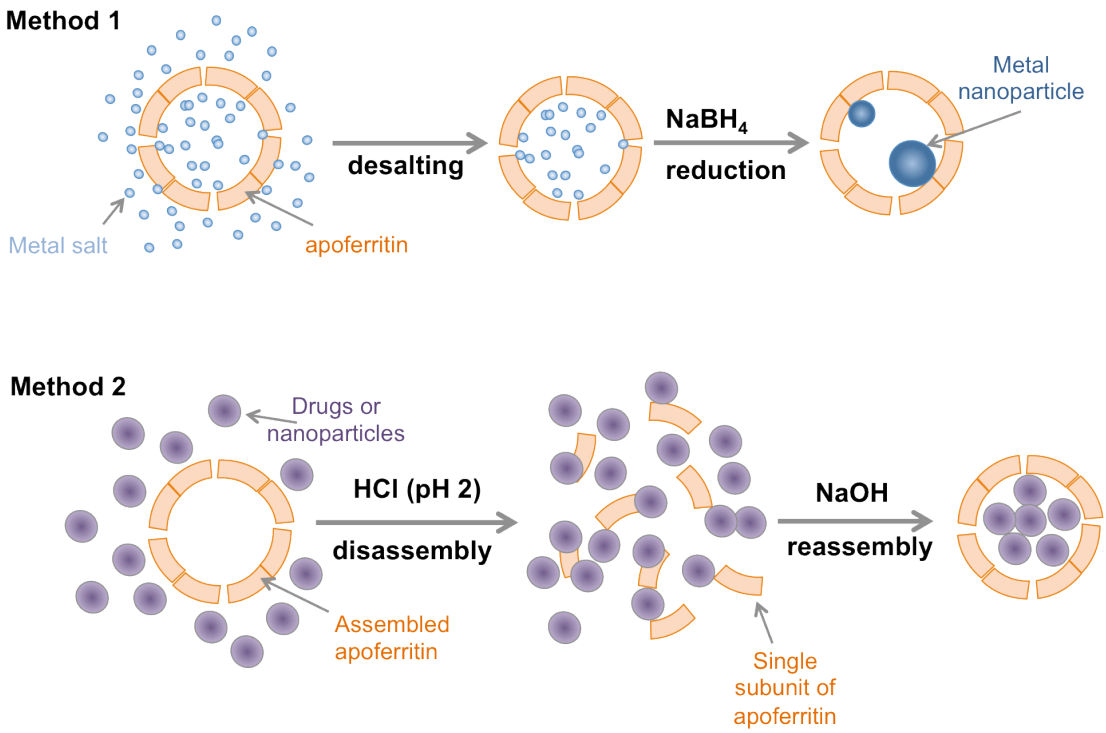

Figure 1.4. Schematic representation of the two possible encapsulation processes. Method 1: direct incubation of apoferritin with metal ions. Method 2: disassembly and reassembly mediated by changing the pH.

This first method is only applicable with ions and particles that are small enough to enter the protein through the available channels.

For larger particles or complexes the second method needs to be applied. Here, at pH 2 the quaternary structure of ferritin is first disassembled without denaturation of the protein. Then the material to be encapsulated is mixed with the protein-containing solution and finally, by increasing the pH to physiological values, the protein is reassembled. In this way a fraction of the material will be encapsulated [37,77]. Due to the change in pH many pH sensitive compounds cannot be synthetized in this way. Nevertheless the process was shown to be effective for encapsulation of numerous drugs or nanoparticles (Figure 1.4 Method 2).

1.4.1 Applications of ferritin based hybrid compounds

Most of the developed composites target applications in the biomedical field. In most of the cases the specific functionality of each nanoparticle or molecule will define the functionality of the whole compound. Before further detailing on the applications of the synthetized ferritin based compounds, several attributes common for all the compounds should be mentioned. Generally, the biomolecules complement properties which inorganic nanoparticles usually don`t have. The most important property for bio-related research is biocompatibility.

Once the nanoparticle is inside the protein shell of apoferritin, the biocompatibility of the nanoparticle increases considerably [78,79]. This is resulting from the increased water solubility, the reduced cytotoxicity of the compound and the biological functionality given by the encapsulating protein.

The latter point leads to the possibility of any encapsulated material to become internalized by receptor-mediated endocytosis [80–82]. This process has been widely studied, resulting in the identification of various receptors for H- or L-ferritins on different cell types [77].

These factors make ferritin a particularly suitable candidate for drug delivery [83] applications or gene therapy [84]. In those cases the ferritin cavity can be loaded with an anticancer drug or a designed nucleic acid and

internalized. The ferritin capsule protects the sensitive molecules and prevents them from degradation or modification in a cellular environment. Furthermore, an internalization with H-chain ferritin into nuclei of cells has been recently demonstrated [77,84].

Besides targeting therapies, many compounds are designed for a use in diagnosis. Classical clinical imaging techniques such as Magnetic Resonance Imaging (MRI) can be improved with specific contrasting agents [85,86], for example Gd (III)-complexes encapsulated with apoferritin [87]. Also, nanoparticles of certain iron or manganese oxides have been studied as contrasting agents for MRI after encapsulation with apoferritin [88].

Another area of application of ferritin-derived composites relates to catalysis [89–91]. Apoferritin provides an excellent template for the size controlled synthesis of catalytic metallic nanoparticles [92]. The outer protein further helps to solubilize the particles making an application of the catalysts in aqueous environment easier.

Such composites can sometimes mimic specific catalytic reactions of enzymes. The catalytic activity is given by the corresponding properties of the metal inside apoferritin [93,94]. Earlier works done in our group have shown that intracellular ROS levels could be decreased using hybrid nanocomposites based on ferritin [95].

1.5. Present work

This thesis has three main sections, with the common element for all of them being ferritin or apoferritin. The perspective to approach the ferritin activity was different in each individual part. Figure 1.5 outlines the cross-disciplinary nature of the thesis.

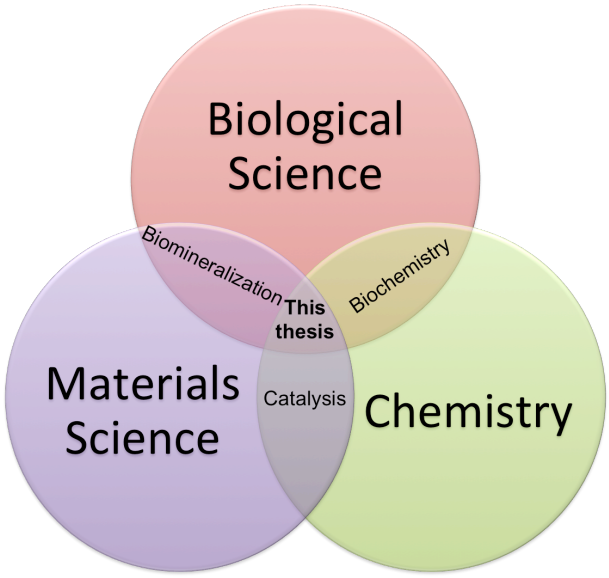

Figure 1.5. Topical spread and interdisciplinary nature of the thesis.

In the first part (**Chapter 3**), the catalytic activity of metallic (Pt and Au) nanoparticles encapsulated within apoferritin is evaluated. In this part the ferritin acts as template for the metal nanoparticle synthesis only.

In the second part (**Chapter 4**) the ferroxidase-mimicking activity of apoferritin encapsulated platinum is matter of *in vitro* studies with cell cultures. For that purpose, the biocompatibility and the ability of the ferritin to be internalized into the cells is of crucial importance.

In the third part (**Chapter 5**) some intrinsic properties of the ferritin protein are evaluated in more detail. Our specific interests relate to the functional differences between L-chain and H-chain proteins.

Chapter 2

Materials and Methods

2.1 Materials and instruments

Most of the proteins and chemicals in this thesis were purchased from Sigma Aldrich (Spain). Some specific proteins or specialized chemicals were purchased from other companies as indicated where they were mentioned; the specific and recombinant human heavy-chain ferritin (huFH), human light-chain ferritin (huFL), human heavy-chain apoferritin (apo-huFH) and human light-chain apoferritin (apo-huFL) were purchased from MoLiRom (Italy). Most of the kits for bio-characterization, like Pierce® 660 nm Protein Assay Kit, Bradford Reagent and Cell Counting Kit 8 (CCK 8) were purchased from Thermo Scientific (Spain).

Ultraviolet-visible (UV-Vis) absorption spectra were measured with a NanoDrop 2000c spectrometer (Thermo Scientific). Platinum determination was done with atomic absorption spectroscopy (AAS) by the company BioSolutions (Halle, Germany). Electron microscopy was done with a TEM (Titan G2 60-300 operating at 80 KeV) and a SEM (FEI, Quanta 250 FEG). Further used instruments will be specified where those were used.

2.2 Synthesis and sample preparation

2.2.1 Metal Nanoparticles within Apoferritin

Platinum or gold nanoparticles encapsulated within apoferritin (Pt-apo and Au-apo) were synthesized according to the following procedure.

Solutions with a concentration of 500 mM potassium platinum (II) chloride (K_2PtCl_4) or 50 mM potassium gold (III) chloride ($KAuCl_4$) were obtained by dissolving the corresponding salt in phosphate-buffered saline (PBS). Then a mixture of 10 % (v/v) buffer and 10 µM apoferritin was added to the solution. This final mixture was incubated for 2 h at 30 ºC. The excess metal salt was removed by passing the solution through a desalting column (40 kDa Molecular Weight Cut-Off (MWCO) from Thermo Scientific). The collected solution, containing the apoferritin encapsulated metal salt, was reduced with preloaded $NaBH_4$ and incubated for 20 min at 30 ºC. For purification of the nanocomposite solution, the solution was passed again through a further desalting column (40 kDa MWCO).

A similar procedure was followed for the synthesis of platinum-gold bimetal nanoparticles encapsulated within apoferritin (PtAu-apo). A solution with a concentration ratio of 1:100 of $KAuCl_4$ and K_2PtCl_4 was prepared and used for the initial incubation. For enabling a meaningful comparison between PtAu-apo and Pt-apo, a concentration of K_2PtCl_4 of 500 mM was used in both cases. After determining the protein concentration, the synthesized samples were stored at 4 ºC until further use.

2.2.2 H/L heteropolymeric apoferritin

The synthesis of heteropolymeric apoferritin with 10, 50 and 90 % L-chain protein content (mixture of H and L-chain proteins of ferritin) were obtained with the following procedure:

Starting from recombinant pure H and L apoferritins, a proportional mixture was prepared. Then the apoferritins were disassembled by adding 1 M HCl solution until pH 2 was reached. Once the solution was stabilized at pH 2 the sample was shaken. Afterwards the pH was increased by adding 1 M NaOH

until pH 8 was obtained, which resulted in reassembly of the protein. After 30 min, the heteropolymeric H/L apoferritin was purified using spin columns (40kDa MWCO). After determining the protein concentration, the samples were stored at 4 ºC.

2.2.3 Sputtered gold on a silicon wafer

Silicon wafers were first cleaned with isopropanol and subsequently sputter-coated in two steps. At first, 10 nm of titanium was deposited, followed by 40 nm of gold. The instrument used for this process was a LEICA EM MED020 sputter coater.

2.2.4 Gold sample pre-treatment

Samples pretreated with mercury: The gold covered silicon wafers were used to analyze the catalytic activity of gold in presence of mercury ions. For that, the gold samples where submerged in a solution containing 2 mM $HgCl_2$, 2 mM H_2O_2 and 10 mM PBS buffer over night. Before any further analysis the samples were cleaned by rising with water and isopropanol.

The same method was applied for commercial gold nanoparticles. The only difference in the procedure relates to the duration of the treatment, being 1 h instead of overnight.

Samples treated with ammonia: Some of the samples pretreated with mercury as well as some untreated gold samples were exposed to ammonia vapor. For that, the samples were placed on top of an open bottle of ammonia (28 %) in a well-operating chemical hood for less than 2 s.

2.3 Characterization methods

2.3.1 UV-Vis absorption spectroscopy

UV-Vis spectroscopy is a characterization technique commonly used in chemistry and biology. The technique is based on the detection of the absorbed wavelength of UV-Vis irradiation, which is specific to the molecules present in the analyte.

The absorbance is calculated from the ratio between the transmitted light (I_{out}) and the incident light (I_{in}) with the following equation:

$$A = \log\ (I_{in}/I_{out})$$

Before any absorbance measurement, the background spectrum must be measured in order to subtract any absorbance arising from the cuvette or the buffer.

This spectroscopic method is commonly used for the determination of the concentration of a substrate. The correlation of the concentration of a substrate with its absorbance is given by the *Lambert-Beer Law* (Equation 2.1.).

Equation 2.1. Lambert-Beer Law

$$A = \varepsilon \times l \times C$$

Herein A is the absorbance of the analyte, ε the absorbance coefficient (l/mol·cm), l the length of the optical pathway (cm) and C the concentration of the analyte (mol/l).

We applied this spectroscopic method for determining the protein concentration, for quantifying the amount of decomposed H_2O_2 and for following the reduction of Cytochrome c. While in some cases the spectra of the product were analyzed directly, in several other cases commercial kits were used to determine the desired component. Those cases will be individually explained in the following. In all cases the NanoDrop 2000c spectrometer from Thermo Scientific was used for recording the spectra.

This instrument is very versatile in its application. It is able to measure spectra of samples in quartz or poly-(methyl methacrylate) PMMA disposable cuvettes (Figure 2.1 A), but is also able to measure spectra of small amounts of the analyte, for example droplets with volumes of 2-3 µl (Figure 2.1 B). For measuring reaction kinetics, the analyte can be stirred within a cuvette and the temperature can be controlled.

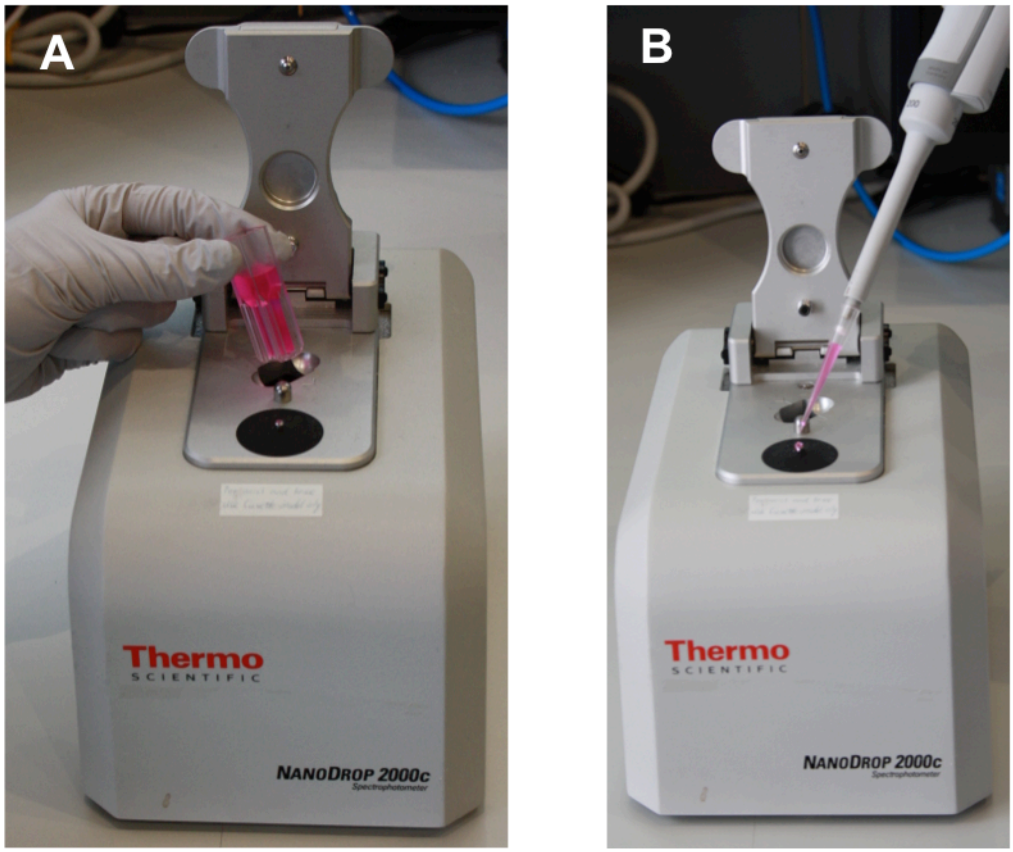

Figure 2.1. Photograph of a NanoDrop 2000c in A) cuvette measurement mode, and B) droplet measurement mode.

Protein determination

Protein determination or quantification was performed with two different methods. The selection of the method was depending on the component to be analyzed and consideration of foreseeable interferences.

The **Pierce® 660 nm Protein Assay Kit** (Thermo Scientific) is a commercially available colorimetric detection method. The main advantages are that the solution is ready-to-use and the higher compatibility with buffers, detergents and reducing agents in comparison to other protein quantification techniques like Bradford.

The tests were done according to the manufacture`s protocols. In summary, a protein-containing sample was mixed with a 15-fold volume of the assay solution. Then the mixture was incubated for 5 minutes at room temperature (RT) before the absorbance at a wavelength of 600 nm was measured by UV-

Vis spectroscopy. The protein concentration was determined using a standard curve established by Bovine Serum Albumin (BSA) standard solutions (Thermo Scientific).

The **Bradford protein assay** is a protein quantification technique based on the complex formation of the dye, Brilliant Blue G, and the protein. The tests were performed following the procedure established by the manufacturer. The absorption peak of the Bradford Reagent at 595 nm wavelength in presence of the protein was used to determine the protein concentration. The test consists of mixing 1 part of the analyte with 30 parts of the Bradford Reagent. The mixture was incubated at RT for 5 min before measurement. The data was compared with a standard curve of BSA with a known amount, which was used as reference.

Catalase mimicking reaction

The catalase-like activity was followed by measuring the remaining hydrogen peroxide concentration in the reaction sample upon its decomposition over time. For the quantification a commercially available assay kit, the PeroXOquant^{TM} Quantitative Peroxide Assay Kit from (Thermo Scientific), was used.

The assay kit is based on indirect quantification and was used according to the manufacturer`s instructions. This assay quantifies the Fe^{3+} - xylenol orange complex with a maximum absorption value at 560 nm. This complex forms in presence of hydrogen peroxide from the analyte and ammonium ferrous (II) sulfate (25 mM) and xylenol orange (125 M) from the assay kit. The Fe^{2+} is oxidized to Fe^{3+} by the hydrogen peroxide, which is subsequently complexed by xylenol. The quantity of the formed complex is proportional to the hydrogen peroxide present in the aliquot.

The reaction performed to investigate the catalase mimic was as follows:

In a pH constant environment, buffered with PBS at pH 7.4, the analyte containing 2-5 mg/ml protein concentration of Pt-, Au- or PtAu-apo or a corresponding amount of Au-nanoparticles was added. The reaction was started with the addition of 2 mM H_2O_2 to the solution. Before the

measurement, aliquots were taken at 0, 10, 20, 30 and 60 min and were diluted with water first in a 1:20 volume ratio and finally added to the assay kit solution in a 1:10 volume ratio. For the hydrogen peroxide quantification the final solution was incubated for 15 minutes at RT and the absorption at 560 nm was measured. The concentration of H_2O_2 was calculated using a previously measured standard curve.

Xylenol orange assay:

The assay was performed at 30 ºC with a mixture of 0.1 mg/ml protein, 50 mM Tris-HCl buffer at pH 7.0 and 40 µM $(NH_4)_2Fe(SO_4)_2$. The reaction started with the addition of Fe^{2+}. A 10 µl aliquot was taken from the reaction at 0, 5, 10, 20, 30 and 40 min and mixed with 100 µl of a solution of 125 µM Xylenol Orange (XO) and 25 mM H_2SO_4. After incubation at RT for 20 min, the concentration of ferric ions in the aliquots was determined by measuring the absorbance at 595 nm [96]. The autoxidation of the ferrous ions was controlled in the same assay conditions, but without addition of proteins. The aqueous solutions of $(NH_4)_2Fe(SO_4)_2$ with 25 mM H_2SO_4 were freshly prepared for each assay.

The Zn^{2+} induced inhibition was measured with 10 mM $ZnCl_2$ in the reaction mixture. The influence on the XO assay was determined by adding 10 µl of 550 mM $ZnCl_2$ to 100 µl 125 µM XO with 25 mM H_2SO_4 and the absorbance at 595 nm was measured for 15 min.

Ferroxidase mimicking activity

Ferroxidase catalyzes the oxidation of iron from Fe^{2+} to Fe^{3+}. The mimic of this reaction by our composites was followed with UV-Vis spectroscopy in ambient conditions. The baseline was measured with 0.5 mM apoferritin protein and 10 mM Tris-HCl buffer at pH 7.0. The reaction started with the addition of $(NH_4)_2Fe(SO_4)_2$ in water to reach a final concentration of 40 mM and the changes in the absorption were recorded.

Cytochrome C reduction activity by ferritin

Cytochrome C (Cyt-c) is a protein with characteristic UV-Vis absorption signals for each of the oxidation states. The oxidized form of Cyt-c has two dominating absorption peaks at 409 and 533 nm and the reduced form at 415 and 550 nm. The kinetics spectroscopy method was used to follow the formation of reduced Cyt-c. The experiment set up was as follows:

Inside a closed quartz cuvette, containing a mixture of 10 µM oxidized Cyt-c, 10 mM Tris-HCl buffer at pH 7.0 and 0.5 mg/mL protein, an inert gas environment was formed by purging with 200 sccm 99.9999 % N_2. After 5 minutes of stabilization time absorption spectra were recorded and used as baseline. Further absorption spectra were recorded in intervals of 30 s during the first 120 s and in intervals of 15 s during further 900 s to follow the kinetics of the reduction reaction. Immediately after the measurement point at 90 s iron was added to the cuvette in form of $(NH_4)_2Fe(SO_4)_2$ to a final Fe^{2+} concentration of 50 µM. With the addition of iron, the Cyt c reduction started.

Finally, the reaction yield was calculated photometrically. The concentration of the oxidized form of Cyt c was calculated at the starting point using the absorption peak at 409 nm ($\Delta\varepsilon = 1.06 \times 10^5\ M^{-1}\ cm^{-1}$). For the reduced form, the peak at 550 nm ($\Delta\varepsilon = 21.1 \times 10^3\ M^{-1}\ cm^{-1}$) [97] was used (Figure 2.2).

The superoxide dismutase (SOD) inhibition test was performed by adding 10 µg/mL of recombinant bovine SOD (≥ 2500 units/mg) directly to the reaction mixture.

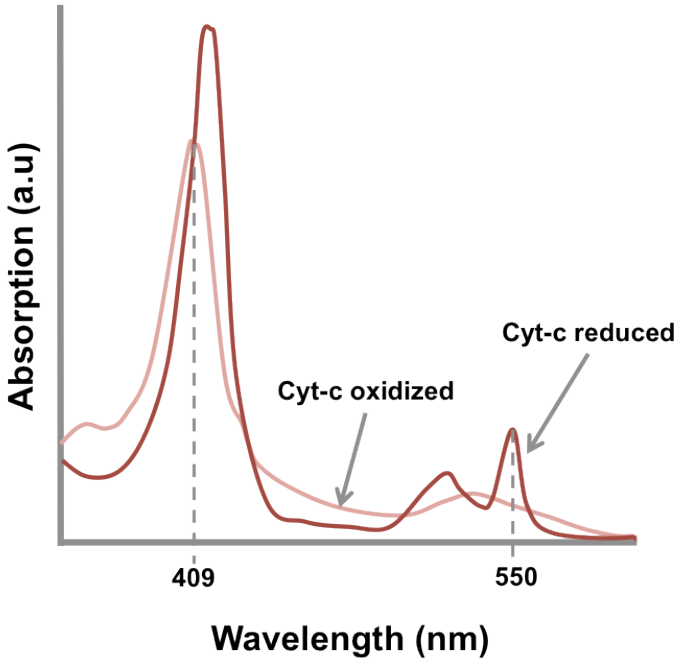

Figure 2.2. Cytochrome c absorption spectra in its reduced and oxidized forms.

Demineralization of Fe in Ferritin

Demineralization of ferritin is a process that involves reduction of the iron within the ferritin. The demineralization was characterized by measuring the amount of Fe^{2+} ions released from the ferritin by complexing it with 3-(2-Pyridyl)-5,6-di(2-furyl)-1,2,4-triazine-5`,5`-disulfonic acid (Ferene S) that selectively makes a complex with Fe^{2+} [98]. The complex can be detected by measuring its characteristic absorption at 593 nm with UV-Vis spectroscopy. The demineralization process has been done with two different techniques, the classical *chemical demineralization* and with *light induced demineralization*. In the following both techniques will be described.

Chemical demineralization was done using nicotinamide adenine dinucleotide (NADH) and flavin mononucleotide (FMN) as reducing agents. The reduction was performed at RT in inert conditions. For this purpose, the sample was purged with N_2 for several minutes before the experiment and continuously during the experiment. The experiment was performed with 75 µg/ml ferritin, 10 mM 2-(N-morpholino)ethanesulfonic acid (MES) buffer, 2.5 mM Ferene S, 200 µM FMN and 2 mM NADH. The demineralization kinetics was followed by measuring absorption spectra at 593 nm in intervals

of 30 s. The baseline was recorded from the solution containing all components except NADH. The reaction started with the addition of NADH.

Light induced demineralization was performed by illumination of the cuvettes with light emitting diodes (LED) having various wavelengths of emitted light, including BLUE (465 nm), GREEN (569 nm), YELLOW (588 nm), and RED (626 nm). The working solution was prepared from 75 µg/ml ferritin, 10 mM MES, TRIS or PBS buffer and 2.5 mM Ferene S. The reaction was performed in an inert environment (purged with N_2 for 5 min before starting the reaction and continuously during the reaction). Background spectra were taken before switching the light on and afterwards every 60 s during the reaction. The kinetic process was followed with recording the absorption peak of Ferene S at 593 nm.

Analysis of the SOD activity

For analyzing the SOD activity, the Assay Kit WST was used. It is based on the reaction between Dojido`s water-soluble tetrazolium salt (WST-1) and O_2^- superoxide ions. In this reaction O_2^- will be reduced and WST-1 formazan will be formed. The formation of WST-1 formazan is proportional to the amount of superoxide. The SOD activity of the nanoparticle-apoferritin composite will suppress the reaction by decreasing the amount of superoxide available for the reaction. This will cause an intensity decrease of the absorption peak of WST-1 formazan at 440 nm. Therefore, the SOD activity can be quantified by measuring the intensity variation of the WST-1 formazan peak.

The measurement was done in a 96 well-plate with the following layout for each sample:

Blank 1: dd H_2O + WST-working solution + Enzyme working solution

Blank 2: sample (ferritin composite) + WST-working solution + dilution buffer

Blank 3: dd H_2O + WST-working solution + dilution buffer

Sample: sample + WST-working solution + Enzyme working solution

The enzyme working solution and WST-working solution were freshly prepared following the manufacturer's instructions. The reaction mixtures in the plate were incubated for 20 minutes at 37 ºC before measuring the absorbance with the microplate-reader (Victor X5, PerkinElmer).

The SOD activity was calculated from the absorbance values with the following Equation 2.2:

Equation 2.2. SOD activity calculation

$$SOD\ activity = \frac{(A_{blank\ 1} - A_{blank\ 3}) - (A_{sample} - A_{blank\ 2})}{(A_{blank\ 1} - A_{blank\ 3})} \times 100$$

2.3.2 Gel electrophoresis (Native and SDS PAGE)

Polyacrylamide gels were used to separate, identify and purify proteins by electrophoresis. It is a simple and rapid technique to resolve and quantify single proteins. Two types of polyacrylamide gel electrophoresis (PAGE) were used: a) *native PAGE,* where the protein conformation or protein bonds to other compounds can be detected, and b) *sodium dodecyl sulphate-polyacrylamide gel electrophoresis (SDS-PAGE),* which is used with denatured proteins for their later identification by *Western Blotting* (Figure 2.3).

Western blotting is a commonly used analytical technique in biology, generally for protein detection, determination and quantification. The western technique requires a previous separation of proteins by gel electrophoresis. Thereafter the proteins are transferred from the gel to a nitrocellulose membrane by applying an electric field. The membrane is then treated with signal blocking proteins, usually BSA or fat free milk, and later with specific antibodies before the final protein detection is done with a second antibody.

Native PAGE:

Continuous native PAGE according to McLellan [99] was used to analyze the stability of the protein. Tris/Boric acid buffer (50 mM Tris, 25 mM boric acid, pH 8.7) was used both for the gel formation and as the running buffer.

Apoferritin, ferritin or metal containing apoferritin were mixed in a 1:1 ratio with the sample buffer and analyzed with a continuous 4 % native gel. The sample buffer was prepared from 10 % Tris/Boric acid buffer, 30 % glycerol, 2 % bromophenol blue (0.5 %) and purified H_2O (Millipore). Following the PAGE, the gel was stained with Imperial™ Protein Stain (Thermo Scientific).

SDS PAGE:

Proteins from cells were separated with a 14 % SDS-polyacrylamide gel adding a maximum of 25 µg of the protein to each well. After electrophoresis, the gel was stained with Imperial™ Protein Stain (Thermo Scientific). The intensity quantification of the proteins was performed with the Kodak Molecular Imaging Software.

Protein detection with Western Blotting:

The cellular membrane fractions were collected with the Mem-PER Plus Membrane Protein Extraction Kit (Thermo Scientific). 25 µg membrane proteins were separated with 4-20 % gradient Tris- glycine polyacrylamide gels for SDS-PAGE (Thermo Scientific) and electroblotted onto polyvinylidene fluoride (PVDF) (BioRad) with Trans-Blot® Turbo™ Transfer System (BioRad). PVDF membranes were blocked for 2 h at room temperature in 5 % BSA–Tris-buffered saline/Tween 20 (TBST; 25 mM Tris HCl, pH 7.5/150 mM NaCl/0.05 % Tween 20). Following this, the membranes were incubated overnight at 4 °C with 1 µg/ml rabbit anti-ferroportin and anti-transferrin receptor antibodies. The following day, the membranes were washed four times with TBST and incubated at room temperature for 1 h with a peroxidase-conjugated anti-rabbit antibody (Thermo Scientific) in a 1:1000 dilution as the secondary antibody. The rabbit anti- Na^+/K^+ ATPase antibody with a 1:15000 dilution from Abcam was used to detect ATPase in the cell membrane fractions. For the enhanced chemoluminescence detection the Amersham ECL Prime detection reagent was used and the signal was recorded with the C-DiGit Blot Scanner (LiCor Bioscience)

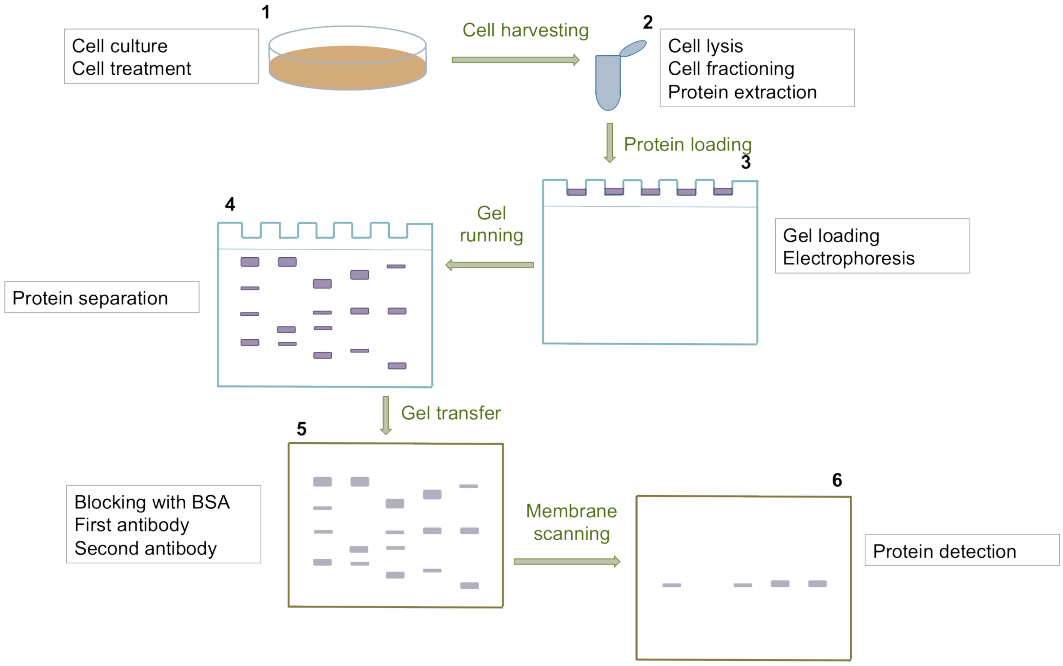

Figure 2.3. Schematic of the procedure for protein detection, starting from the cell culture.

2.3.3 Atomic Absorption Spectroscopy (AAS)

Atomic Absorption Spectroscopy is an analytic technique for the quantification of the metal content in a sample. Having a very high sensitivity, it is able to detect values lower than parts per billion (ppb). Also traces of elements can be detected. In AAS the sample is atomized and irradiated optically. The absorption of the irradiated light by the metal atoms in the gaseous state is measured and the concentration is quantified with the Lambert-Beer Law.

The samples measured for this thesis were platinum nanoparticles within apoferritin with a protein concentration of 0,8 mg/ml. Measurement and determination of the concentration were done by the company BioSolutions in Halle, Germany.

2.3.4 Physical characterization

TEM, SEM, EDX and XPS

Electron microscopy is a sensitive technique for physical and chemical characterization of nanostructures or nanocomposites. Common optical microscopes are limited to a resolution of 200 nm, as a consequence of operation with visible light. Electron microscopy uses an electron beam with

100 000 times shorter wavelength than visible light and in this way allows resolutions even to the atomic scale.

Electron microscopy is used in two different ways; in transmission (TEM) the electron beam is passing through the sample and being detected. Areas in the sample with higher atomic mass will scatter the electrons locally, which will show a darker contrast on the detector plate. In (SEM) the electrons back scattered from the sample are detected, giving information on the morphology of the sample (Figure 2.4).

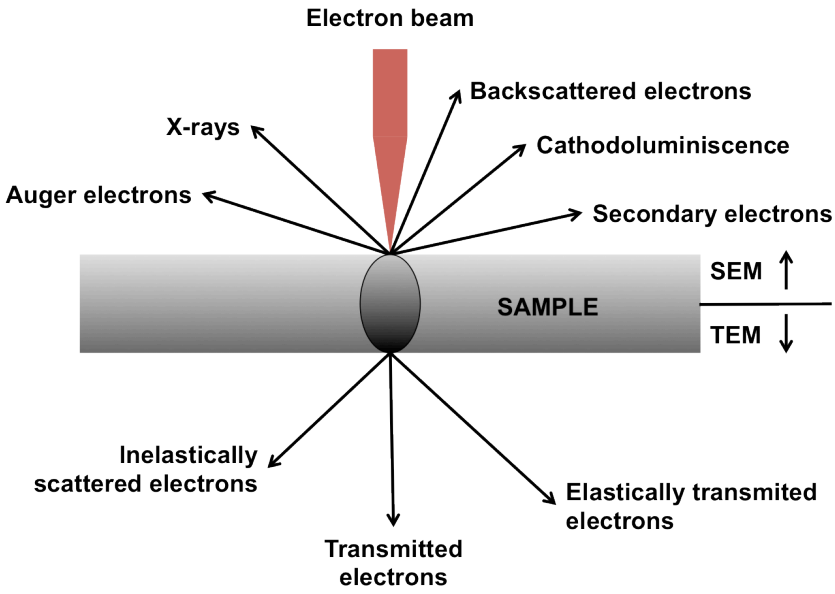

Figure 2.4. Schematic representation of interactions of the electron beam with a sample and the resulting transmitted or backscattered electrons or rays.

TEM can reach higher resolutions in imaging than a typical SEM, but the latter is more convenient for characterization of the morphology and topology of a sample.

Pt-apo samples were characterized by TEM. The samples were pretreated with 1.5 % uranyl acetate and 250 µg/ml Bacitracin for negative staining, since the protein have a low atomic mass and therefore a weak contrast. Adding stains with a higher atomic mass is commonly used to visualize proteins in TEM. For a characterization by SEM, gold was sputtered on the surfaces in order to enhance the backscattering events and suppress surface

charging upon irradiation with the electron beam, which normally occurs with non-conductive samples and hinders an appropriate imaging.

Both electron microscopes are equipped with *Energy-dispersive X-ray spectroscopy (EDX) detectors* that were used for the elemental analysis of the samples.

Energy-dispersive X-ray spectroscopy (EDX)

EDX is a powerful analysis technique that allows both qualitative and quantitative elemental analysis. Owing to the interaction between the electron beam and the sample, electrons from the inner shell of an atom are expelled. An electron from the higher valence level will drop down to fill the empty space. As a result of the energy difference, an X-ray will be emitted which will be detected. As those X-rays are characteristic for each element, it allows the elemental analysis to be carried out.

X-ray photoelectron spectroscopy (XPS)

X-ray photoelectron spectroscopy (XPS) is a technique to analyze the elemental composition and the chemical and electronic states of materials at the very surface of a sample. An X-ray beam interacts with the electron shells of the atoms located close to the surface of a sample. The electrons become excited and escape from the sample as a result of the photoelectric effect. Those electrons are recorded by the detector. Depending on the binding energy of the detected photoelectrons, the type of atom and its binding state to neighboring atoms can be identified.

For XPS analysis, solutions of the analyte were deposited on a piece of Si wafer and dried in air. The XPS spectra were acquired with a spherical analyzer of the type EA 125 (Omicron) and a non-monochromatic Al-Kα (1486.6 eV) source. The measuring equipment was calibrated before use with the 4f line of a gold sample. All measurements were done at a working pressure less than 5×10^{-9} mbar and pass energy of 50 eV. Survey spectra (not shown) were made with a step size of 0.5 eV and an exposure time of 0.5 s per measurement point. High-resolution spectra of the Pt 4f lines were recorded with a step size of 0.1 eV and an exposure time of 10 times 0.5 s per

measurement point. To eliminate the charging effect of the surface, all spectra were corrected with the help of the C 1s line. The position and intensity of each XPS line were determined by Voigt approximation with a linear background.

2.4 In-Vitro Characterization

2.4.1 Cell Culture

The cell culture investigations were performed with the human colon adenocarcinoma cell line Caco-2 obtained from ATCC. The cells were cultured in minimum essential medium (MEM) supplemented with 10 % fetal Bovine Serum (FBS) (Biochrom), 1 % nonessential amino acids and 50 mg/ml gentamicin (37 ºC, 90 % humility, 5 % CO_2).

For passaging and seeding, the cells were released with trypsin/EDTA (0.05%/0.02%) solution once the cell confluence was about 80-90 %. The cells were subsequently seeded to 6-, 24- or 96-well plates at a concentration of $0.75x10^5$ cells/cm^2. The cell culture medium was replaced one day after the seeding and further every two days. The plates were cultured for 8 days for all the assays.

2.4.2 Cell Viability

The cell viability was determined with the **Cell Counting Kit-8** (CCK-8). Cell viability was measured after each treatment of the cells. The treatments included the addition of iron and various ferritins and as well as treatments with blue light.

After the treatment, the cells were washed twice with PBS and incubated with 10 % CCK-8 solution in the culture medium for two hours. The quantification was done by measuring the absorbance at 450 nm using a microplate reader (Victor X5, PerkinElmer). The viability of untreated cells was set as 100 %.

2.4.3 Cellular iron content: Ferene S assay

The effects of metal nanoparticle containing apoferritin, apo-huFH, apo-huFL, huFH and Deferoxamine (DFO) on cells have been analyzed in an iron-

excess environment. The cells were treated for two consecutive days with the final concentration of 0.1 μM protein or 200 μM DFO. On the second day the cells were treated with 100 μM ferric citrate with or without ascorbic acid (200 μM) for 24 h.

The total cellular iron content was measured by incubating with 6 M guanidinium-HCl, 1 mM Ferene-S (3-(2-pyridyl)-5,6-di(2-furyl)-1,2,4triazine-5',5''-disulfonic acid) and 250 mM ascorbic acid for 2 h at room temperature. Ferene-S and Fe^{2+} form a complex with the maximum UV-vis absorbance being at 600 nm. The measurements were carried out with a microplate-reader (Victor X5, PerkinElmer).

Chapter 3

Catalysis

The first part of this chapter describes the inhibitory effect of 3-amino-1,2,4-triazole (3AT), NaN_3 or Hg^{2+} on the catalase and SOD enzyme mimetic activities of platinum nanoparticles synthetized within apoferritin (Pt-apo). A selective and specific inhibition of the mimetic activities through the choice of the inhibitor provides a novel way of tuning the activity of nanoparticles and suppressing undesired reactions. A strategy for recovery of the activity with a reducing agent will be demonstrated. The recovery treatment restores the surface chemistry of the nanoparticles and may even act as a general method for restoring the activity of numerous other nanoparticles.

This first section describes the work published in the journal Chemical Communications from the Royal Society of Chemistry (RSC)[100]. Graphs, figures and parts of the text of the publication are reused in this thesis with permission of the publisher.

Article:

Tuning, inhibiting and restoring the enzyme mimetic activities of Pt–apoferritin. **Unai Carmona**, Lianbing Zhang, Le Li, Wolfram Münchgesang, Eckhard Pippel and Mato Knez. Chem. Commun., (**2014**), 50, 701-703

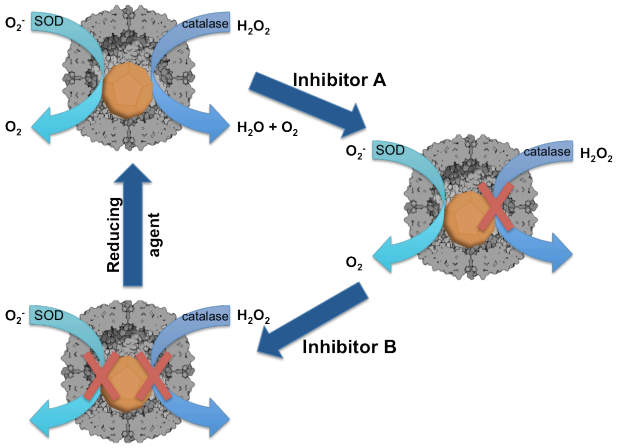

Schematic overview of the investigated catalytic reactions

In the second part, the catalase-like activity of apoferritin encapsulated metal nanoparticles is studied. The catalase-like activity of platinum- and gold-containing hybrid compounds is analyzed and special attention is paid to their reactivity upon contact with the heavy metal mercury. A mechanism for the reaction is proposed.

An article is currently in preparation with the information and data described in the second part of this chapter.

3.1 Pt-apoferritin

The catalytic properties of many nanoparticles and the special interest in them for chemical or biological applications were discussed in the introduction chapter [101,102]. Often these catalytic reactions resemble the ones occurring with enzymes, including hydrogenation, oxidation and further reactions like C-C coupling, etc [103,104]. Although the catalytic reactions of nanoparticles often mimic enzymatic reactions, the reaction mechanisms, which inorganic nanoparticles and biomolecules undergo, are different. For example, the catalytic activities of nanoparticles are usually not specific to a substrate, while those of enzymes typically are. Pt-nanoparticles, for example, can mimic various enzymatic activities, such as oxidase, catalase and superoxide dismutase (SOD) [105–107], while the individual enzymes usually have only one of those activities. Also, biological enzymes usually have natural inhibitors, which regulate their catalytic activities, while possible inhibitors for nanoparticle-activated reactions still must be investigated.

Heavy metals and many synthetic chemicals, such as sodium azide, can specifically or generally inhibit enzymatic activities [108]. In view of potential future applications in enzyme mimetics, it is important to understand whether or not enzyme inhibitors act on nanoparticles in a similar way as they do on biological enzymes.

3.1.1 Sample preparation

Before the investigation of the enzyme-like activity of various hybrid bioinorganic compounds, those compounds were synthesized following protocols from earlier work of the group [95]. The synthesis is described in chapter 2. Direct incubation of metal salts of platinum, gold or a combination thereof with apoferritin and their subsequent reduction, was identified as the most efficient pathway. In Figure 3.1 the simplified schematic of the process is shown.

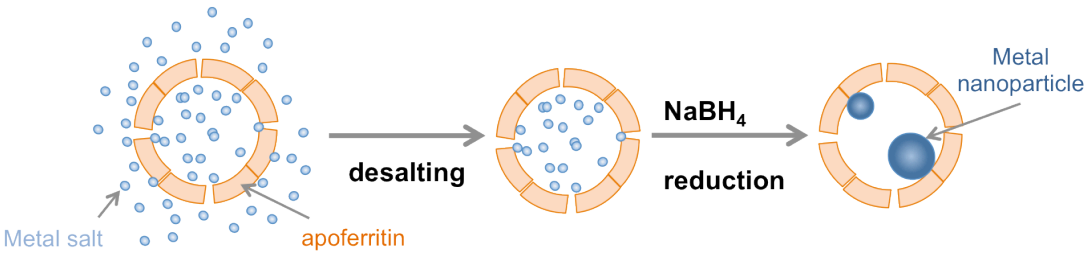

Figure 3.1. Schematic representation of the preparation of platinum nanoparticles within apoferritin (Pt-apo).

The resulting composite was characterized by UV-Vis spectroscopy and TEM. Figure 3.2 shows the resulting TEM images and size exclusion chromatography spectra [82]. The protein concentration was measured with the Bradford method and the protein stability was analyzed by native gel electrophoresis. Table 3.1 summarizes the characteristics of each compound.

Table 3.1. Synthesized compounds.

Name	Metal salt	Protein	Buffer	Reduction agent	Final protein concentration	Yield %
Pt-apo	K_2PtCl_4 (500mM)	Apo-hoSF	PBS	$NaBH_4$	4,4 mg/mL	80
Au-apo	$KAuCl_4$ (50mM)	Apo-hoSF	PBS	$NaBH_4$	4,4 mg/mL	80
PtAu-apo	K_2PtCl_4 (500mM) $KAuCl_4$ (50mM)	Apo-hoSF	PBS	$NaBH_4$	4,0 mg/mL	75

Briefly, after the synthesis a minimum of 4 mg/mL protein concentration was measured for each of the samples, which was sufficient to reach a final protein recovery between 75 and 80 %. The nature of the buffer used for the synthesis has an influence on the size of the nanoparticles, which was subject of earlier investigation (Master thesis U.Carmona) [109]. Here, as buffer for the synthesis of the nanoparticles PBS was chosen.

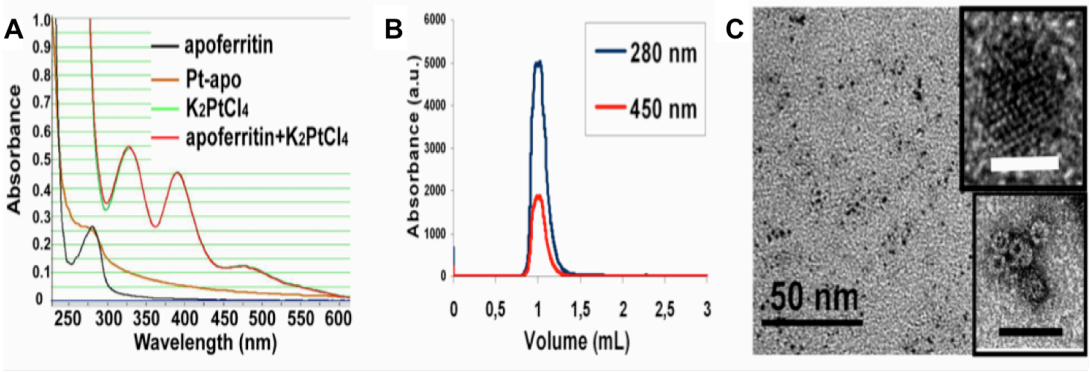

Figure 3.2. A) UV-vis absorption spectra of apoferritin, K_2PtCl_4 and Pt-apo. Apoferritin and Pt-apo were purified with a spin column before the measurements. The reference absorption spectrum was measured with purified water. B) Co-elution of Pt (450 nm) and apoferritin (280 nm) with size exclusion chromatography. C) TEM images of Pt-apo (Upper inset: high resolution electron micrograph of a platinum nanoparticle, scale bar: 2 nm; lower inset: TEM image of negatively stained Pt-apo, scale bar: 50 nm).

The characterization techniques demonstrate the presence of platinum within the apoferritin structure. Furthermore, they show that the final reduction of the platinum ions inside the apoferritin was done successfully. The procedure did not affect the apoferritin shape and size, which remained intact according to the TEM images. With those compounds, we investigated the catalase mimicking reaction. Natural catalase reaction degrades H_2O_2, which is one of the most oxidative compounds occurring in organisms [110,111]. The procedure followed for the kinetic analysis of the catalase activity was described by Zhang et al [95].

The protein stability of the compounds was measured using native gel electrophoresis. The corresponding image is shown in Figure 3.3. Untreated ferritin and apoferritin mark the control bands. No significant changes were observed besides the already mentioned effect of the buffer on the size of the nanoparticle. The protein remained its size and charge.

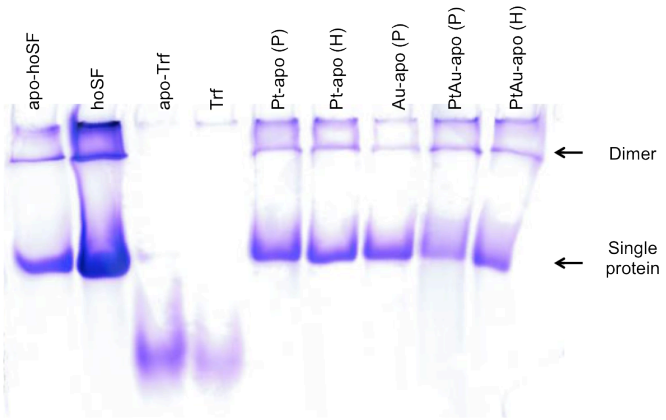

Figure 3.3. Native PAGE: 4% native gel was stained with Imperial™ Protein Stain (Thermo Scientific) after the electrophoresis. Transferrin (Trf) was used as control. (H) and (P) indicate the buffer (HEPES or PBS) used for the synthesis [109]. (Reproduced from the Master thesis U. Carmona)

3.1.2 Tuning, Inhibiting and Restoring

In this section the catalase and SOD enzyme mimetic activities of Pt- were characterized. The main objective was to analyze the influence of various inhibitors on the compound's activity. For this purpose several natural inhibitors for catalase or SOD activity were chosen, NaN_3 as general inhibitor, $HgCl_2$ as heavy metal based inhibitor for both catalase and SOD, and 3AT as catalase-specific inhibitor [112]. To follow the reaction, the initial concentration of the substrate H_2O_2 was measured and set to 100 %. After 10, 20 and 30 min of reaction time the remaining H_2O_2 was determined and the degradation quantified.

Before starting with Pt-based catalysts, the effects of apoferritin and the inhibitors on the hydrogen peroxide decomposition reaction were analyzed. Figure 3.4 shows that those three components did not contribute to the decomposition of H_2O_2. The concentration of H_2O_2 remained stable between ca. 90 % and 100 % over the whole measurement period.

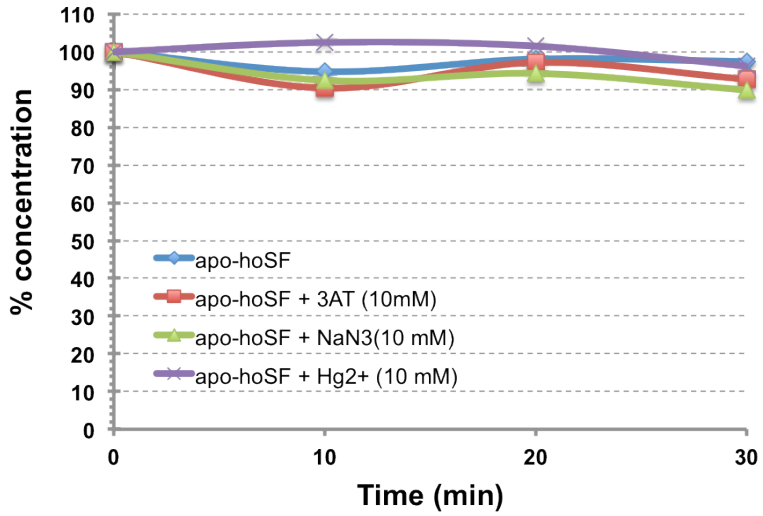

Figure 3.4. Activity of horse Spleen apoferritin (apo-hoSF): H_2O_2-content in the reaction solution in presence of various inhibitors as function of time. Assay conditions: 30 ºC, pH 7.4, 1.875 mg/ml Pt-apo, and 2 mM initial H_2O_2.

Once contribution of the inhibitors and apoferritin to the hydrogen peroxide decomposition were excluded, the same experiments were done in presence of Pt-apoferritin.

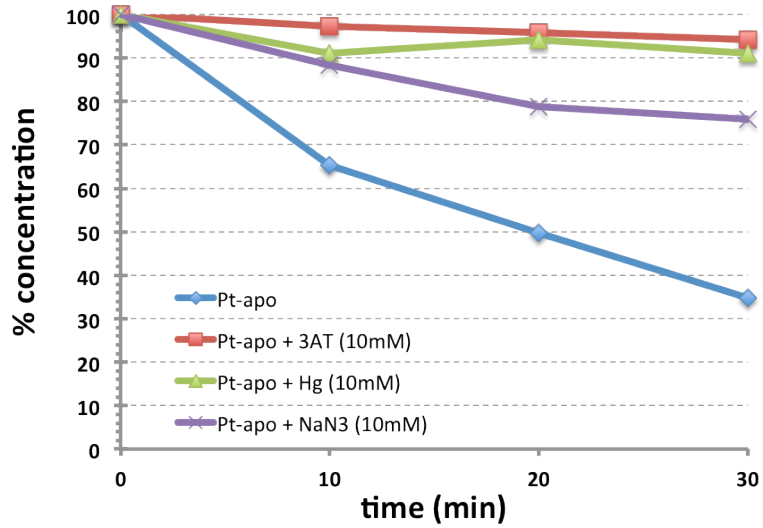

Figure 3.5. Activity of Pt-apo: H_2O_2-content in the reaction solution in presence of various inhibitors as function of time. Assay conditions: 30 ºC, pH 7.4, 1.875 mg/ml Pt-apo, and 2 mM initial H_2O_2.

The graph in Figure 3.5. shows that in absence of inhibitors 65 % of the initial hydrogen peroxide was decomposed by Pt-apo within 30 min. In presence of 10 mM NaN_3, less than 25 % of the initial H_2O_2 were decomposed within 30 min. The inhibitory effect was even more pronounced with 10 mM Hg (II) or

3AT, being nearly quantitative with those two reagents. All three inhibitors exhibited a concentration-dependent inhibition (Figure 3.6).

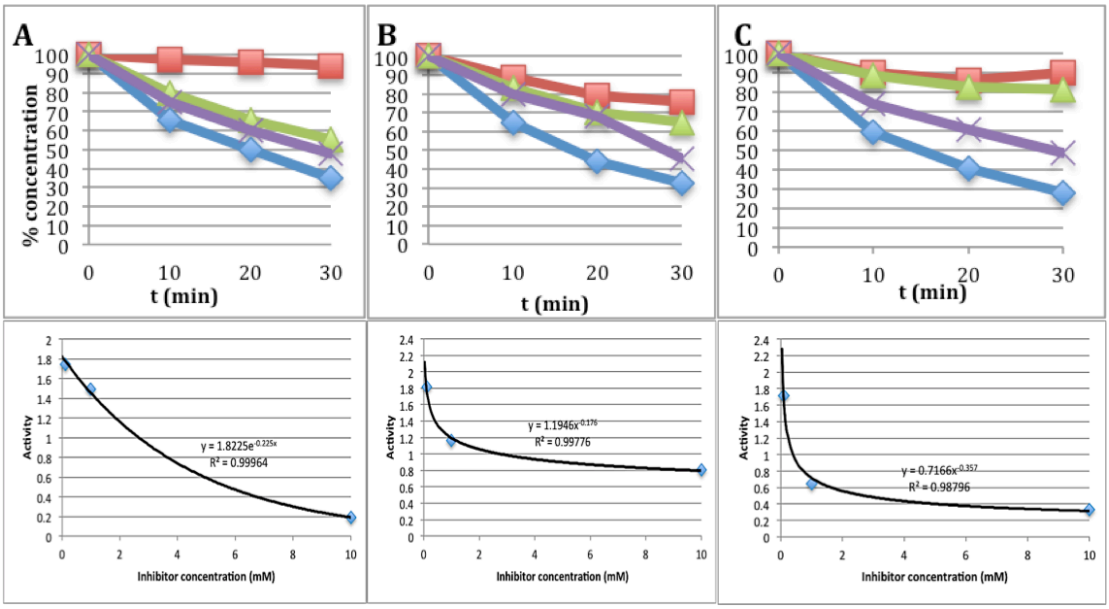

Figure 3.6. Peroxide decomposition activities in presence of inhibitors (upper row) and activity vs. inhibitor concentration (lower row). A) 3AT. B) NaN_3. C) Hg^{2+}. Common assay conditions: 30 ºC, PBS pH 7.4, 1.5 mg/ml Pt-apo and 2 mM H_2O_2. Blue curve: without inhibitor; red curve: 10 mM inhibitor; green curve: 1 mM inhibitor; purple curve: 0.1 mM inhibitor.

The activity versus inhibitor concentration curves in Figure 3.6 indicate different inhibition mechanisms among the samples. The amount of inhibitor necessary to reduce the activity of Pt-apo can be extracted from the curves. Around 1 mM NaN_3 or Hg^{2+} is sufficient to reduce the activity by more than 50 %. In case of 3AT, the tenfold concentration (10 mM) was necessary to reach similar values.

To obtain more information about the reaction mechanisms, Pt-apo was incubated over night with 10 mM inhibitor and subsequently purified with a spin column before the catalase activity was analyzed. This test allows determining the affinity or type of interaction between the inhibitor and the platinum surface that is likely to be the active side for the enzymatic activity. Figure 3.7 shows that without further inhibitor added to the assay solution, the pretreated Pt-apo decomposed less than 40 % of the initial H_2O_2. This indicates that the inhibitor competes with the substrate for the adsorption sites

on the Pt-nanoparticle surface in a dominant way. Thus, the inhibitory effect can be explained with a reduced active surface.

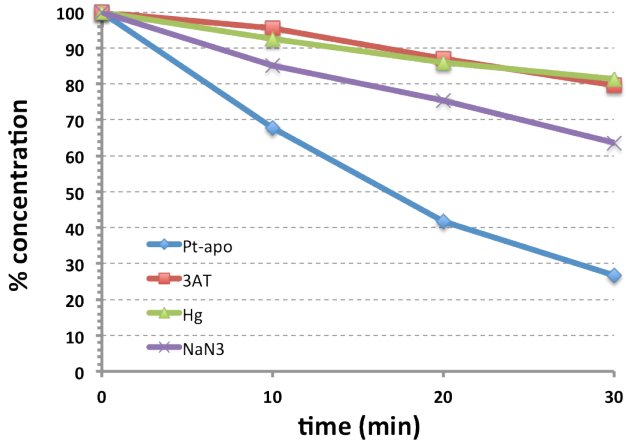

Figure 3.7 H_2O_2-decomposition activity of Pt-apo and inhibitor-pretreated Pt-apo. Assay conditions: 30 ºC, pH 7.4, 1.5 mg/ml Pt-apo or pretreated Pt-apo, and 2 mM H_2O_2.

In the next step, the inhibitory effect of NaN_3 or 3AT on the SOD activity of Pt-apo was analyzed in order to verify whether or not the inhibition is reaction specific. Hg^{2+} could not be evaluated, since it readily inhibits the superoxide generation in the SOD assay system (Assay Kit-WST), even without addition of the nanocomposite. NaN_3 did not inhibit the SOD activity of Pt-apo, while 3AT inhibited 20 % of the relative SOD activity (Figure 3.8)

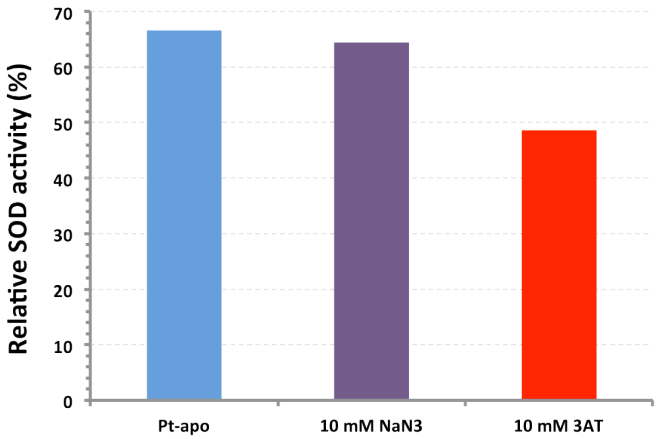

Figure 3.8. Inhibition effect of 10 mM 3AT or NaN_3 on the SOD activity of Pt-apo.

In a further experiment, Pt-apo was treated with the aforementioned two inhibitors and H_2O_2 over night and the relative SOD activity was tested after purification. While more than 20 % of the SOD activity was inhibited upon 3AT treatment, the activity of NaN_3- and H_2O_2-pretreated Pt-apo did not significantly alter in comparison to untreated Pt-apo (Figure 3.9). Together with the previously described catalase inhibition, these results indicate that inhibitors can influence the enzyme mimetic activities of nanoparticles in a reaction-specific manner. This provides a novel combinatorial way to make nanoparticles tunable and flexible catalysts by using inhibitors to selectively suppress their activity, inhibiting the catalase activity with NaN_3, or inhibiting both catalase and SOD activities with 3AT.

The competitive adsorption of 3AT on NPs can explain its inhibition of both catalase and SOD mimetic activities. However, the same theory alone cannot justify the selective inhibitory effects of NaN_3 [113]. It has been observed that superoxide can form singlet oxygen in absence of the enzyme [114]. NaN_3, but not 3AT, is a strong quencher of singlet oxygen. In our case, the singlet oxygen may form during the SOD-like reaction and react with NaN_3 adsorbed on the NP surfaces, which will probably remove the adsorbed azide and abrogate the inhibition. Since superoxide and singlet oxygen are not involved in the catalase reaction, azide ions will remain absorbed and cause the inhibition.

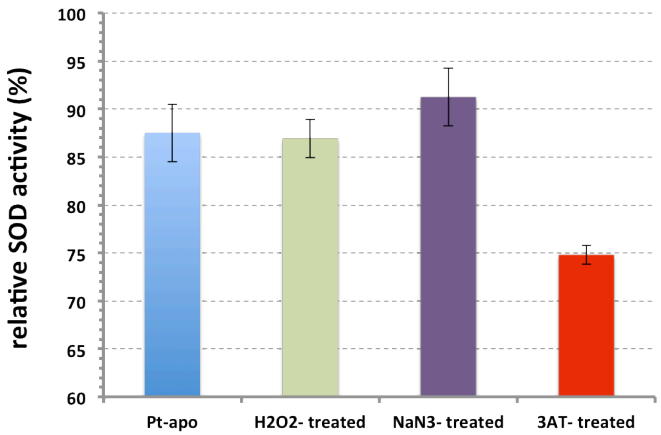

Figure 3.9. Inhibition of the SOD activity of Pt-apo upon its pretreatment with H_2O_2, NaN_3 or 3AT. The concentrations of H_2O_2, NaN_3 and 3AT for the pretreatment: 8, 100 and 100 mM, respectively.

Inhibition of biological enzymes is often irreversible, resulting in a permanent loss of activity [115]. Enzyme mimetic nanoparticles, composed of a robust protein and even more robust inorganic core might be superior to their biological counterparts and the previously described inhibition of the activity might potentially be reversible. Many established methods for protein purification provide the possibility to easily recycle Pt-apo from a reaction mixture. This is, in turn, advantageous for investigating the activity recovery of Pt-based catalysts.

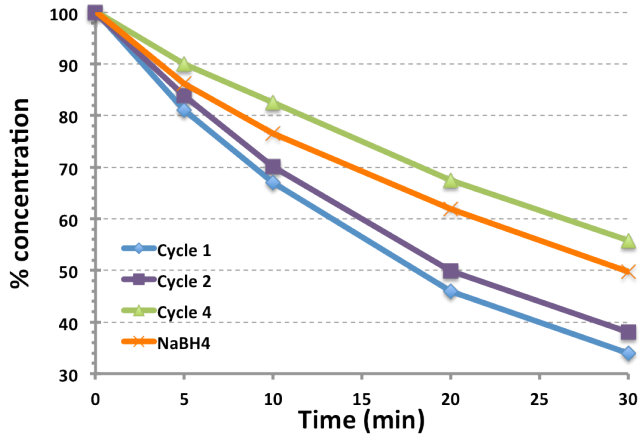

Figure 3.10. The change of the catalytic activity of Pt-apo after multiple reaction cycles and final treatment with $NaBH_4$ (orange line, not normalized with the Pt amount). After each cycle the Pt-apo was separated from the reaction mixture with a spin column.

The H_2O_2 decomposition activity of Pt-apo decreased with each of the four serial reaction cycles (Figure 3.10). Figure 3.11 shows that no significant change in the particle size occurred and most of the apoferritin still showed an intact protein shell. Since H_2O_2 is an oxidizing agent, the reason for the reduction of the catalytic efficiency could be an oxidation of the surface or adsorption of oxygen or some other oxygen species onto the Pt catalyst during the reaction [116,117].

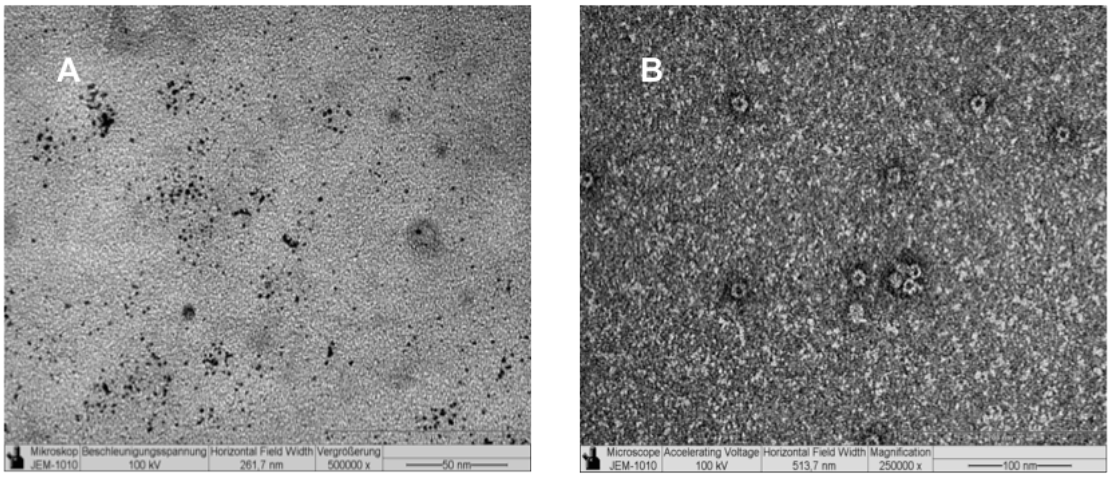

Figure 3.11. TEM images of A) Pt-apo after the peroxide decomposition reaction. B) The intact protein shell was visualized by negative staining with 1.5 % uranyl acetate.

An adsorption of oxygen species during storage was excluded with a reference measurement of the bare sample after 4 weeks of storage resulting in almost identical kinetics (Figure 3.12).

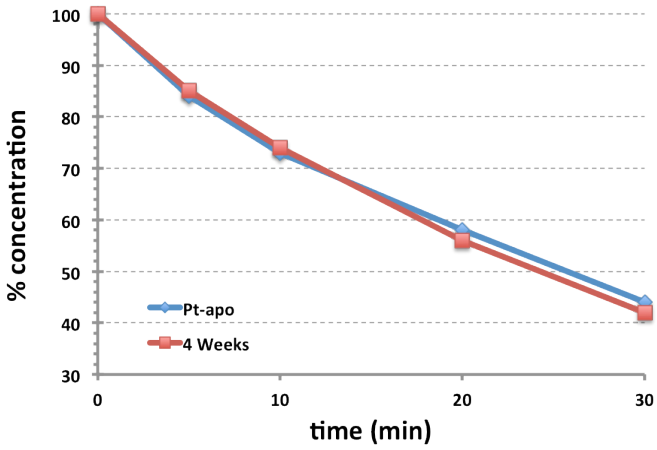

Figure 3.12. Activity change of Pt-apo after storage in water at 4 ^{o}C for 4 weeks.

If the assumption of poisoning in the oxidative environment holds, a removal of the adsorbed oxygen species would logically restore the catalytic activities. In order to prove this, Pt-apo was first treated with 1.32 mM H_2O_2 in sum (equal to four reaction cycles) and subsequently treated with the reducing agent $NaBH_4$ for 5 min. Following this treatment the peroxide decomposition activity of Pt-apo was measured for comparison. The activity of Pt-apo after reduction indeed increased again as compared with the fourth cycle (Figures 3.13 and 3.10).

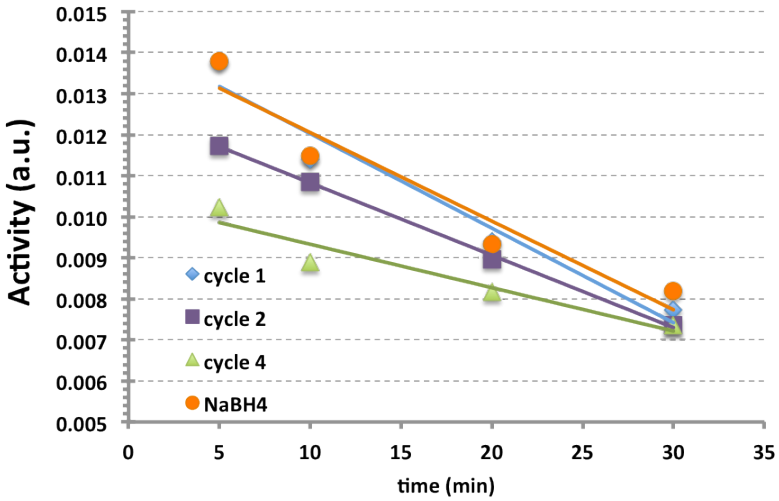

Figure 3.13. Change of the catalytic activity of Pt-apo after multiple reaction cycles and final treatment with $NaBH_4$ (orange line). The activity of Pt-apo was normalized with the Pt quantity determined by atomic absorption spectroscopy (AAS) (Table 3.2). The normalization was done by calculating the percentage of decomposed H_2O_2 per minute per ppm Pt for the corresponding time.

Table 3.2: Concentration of platinum measured with atomic absorption spectroscopy (AAS).

Sample	**Cycle1**	**Cycle2**	**Cycle4**	**NaBH4**
Platinum concentration (ppm*)	288.48 ±16.11	281.15 ±25.04	199.09 ±37.76	207,36 ±17.31

* parts per million (ppm); the protein concentration of the samples was 0.8 mg/ml.

A similar effect was also observed if another common reducing agent, H_2 gas, was used (Figure 3.14). After the removal of the oxygen on the surface, the catalytic activity increased and resembled closely the activity of untreated Pt-apo.

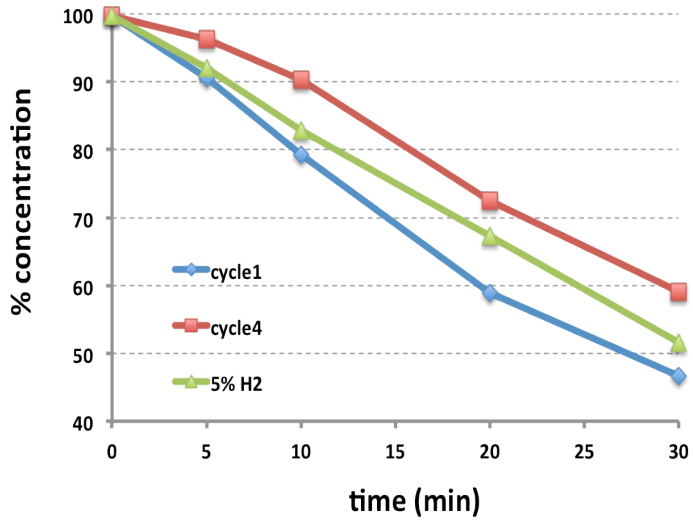

Figure 3.14. A) Recovery of the activity of Pt-apo for the H_2O_2 decomposition reaction with hydrogen gas (5 % in Argon) after 4 reaction cycles.

The changes of the surface of the Pt induced by a potential adsorption or oxidation, as well as after treatment with $NaBH_4$, were investigated with XPS. The Pt $4f_{7/2}$ peak position of Pt-apo shifted from 71.4 eV to 71.9 eV after the H_2O_2 decomposition reaction and shifted back to 71.5 eV after treatment with $NaBH_4$ (Figure 3.15). The XPS measurements demonstrate that the changes induced by the decomposition reaction could be recovered after treatment with $NaBH_4$. This indicates that a reversible surface chemistry is the origin of the restorable activity.

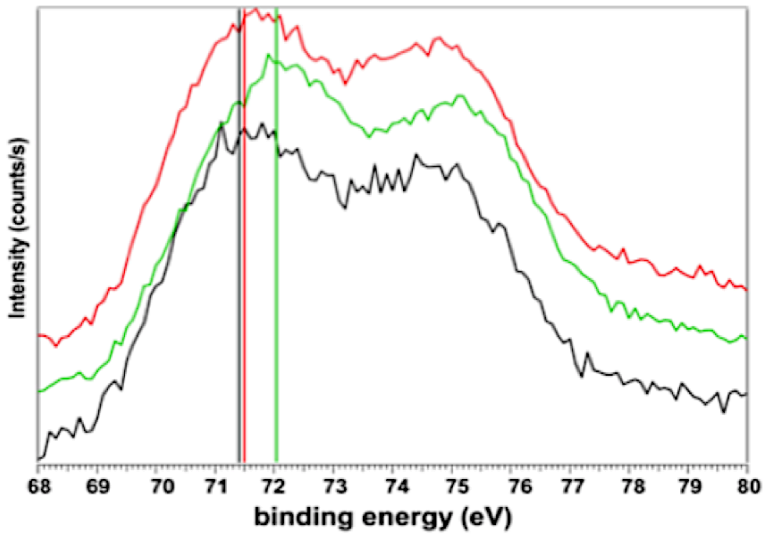

Figure 3.15. XPS Spectra of initial Pt-apo (black), after the reaction with H_2O_2 (green), and after treatment with $NaBH_4$ (red). The spectra show the Pt $4f_{7/2}$ and the Pt $4f_{5/2}$ photoelectron spectral lines with the corresponding background. The corresponding Pt $4f_{7/2}$ position is indicated with vertical lines in the same color.

Finally, the reducing agent was tested for its ability to restore the inhibited SOD activity of 3AT- and NaN_3- treated Pt-apo compounds. The effects of the reducing agent on the protein fraction of the hybrid composite were clearly not the reason for the recovery (Figure 3.16).

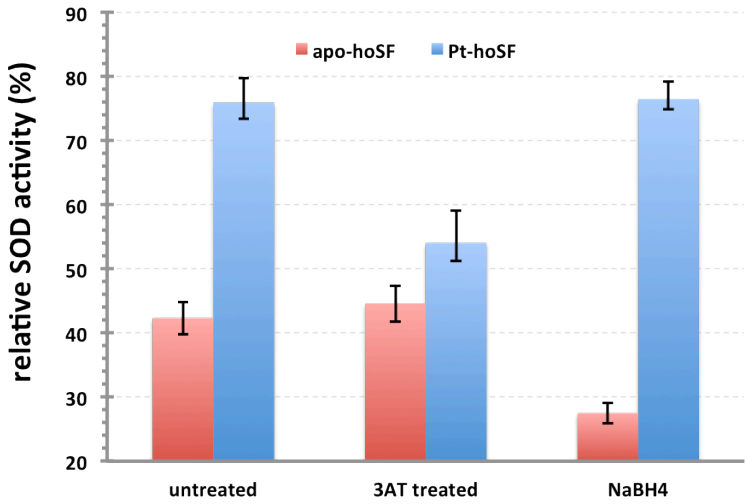

Figure 3.16. SOD activity of untreated, 3AT-treated and $NaBH_4$-treated (after 3AT pre-treatment) Pt-apo. Protein concentration: 550 µg/ml apo-hoSF, 44 µg/ml Pt-apo.

3.1.3 Summary

In summary, the enzyme mimetic activities of ferritin-encapsulated platinum nanoparticles can be inhibited with inhibitors typically active with biological enzymes. NaN_3 inhibited only the catalase activity of Pt-nanoparticles, but not the SOD activity, while 3AT inhibited both catalase and SOD activities, indicating the possibility to achieve selective and specific activity suppression with inhibitors. This opens the door towards controlling the activities of nanoparticles in a reaction specific manner with further inhibitor screening, which is greatly interesting for nanoparticle engineering for targeting enzyme mimetics. The demonstrated activity recovery of catalytic activities with $NaBH_4$, restoring the chemical properties of the nanoparticle´s surface, promise to be a more universal technique for the regeneration of the nanoparticles, which is not limited to catalytic applications.

3.2 Au-apoferritin

In the following section the catalase–like enzyme mimetic activity of gold treated with mercury ions is studied [118]. The reason for this study results from the observation that mercury ions show peculiar behavior in the decomposition of H_2O_2 if combined with gold nanoparticles, which justifies a more in-depth analysis.

Many studies in literature investigated the combination of gold, mercury and H_2O_2 for the sake of mercury detection or hydrogen peroxide decomposition [118–120]. However, none of those shows a conclusive reaction mechanism of the involved catalytic processes. Moreover, the studies are often contradictory. In the following, a reaction mechanism will be proposed based on our experiments on the catalase activity.

We used the previously described platinum (Pt-apo), platinum-gold (PtAu-apo) and gold (Au-apo) nanoparticles. The synthesis of the particles is described chapter 2.

Those synthesized hybrid components were analyzed for their catalase activity or H_2O_2 decomposition in presence and absence of mercury (II) chloride ($HgCl_2$). For this purpose, the initial concentration of the substrate H_2O_2 was measured and the decomposition percentage was calculated after measuring the remaining H_2O_2 after one hour of reaction time, similar to the previous chapter.

3.2.1 Hg effect on Au apoferritin

An evidence of Hg^{2+} influencing the catalase activity of Au-apo is shown in Figure 3.17. Without Hg^{2+}, Pt-apo showed the highest activity among the three types of nanoparticles decomposing more than 75 % of initial peroxide within one hour. For comparison, PtAu-apo decomposed less than 50 % and Au-apo only 4 % of the H_2O_2. Adding 1 mM Hg^{2+} changed the reactivity of the composites significantly.

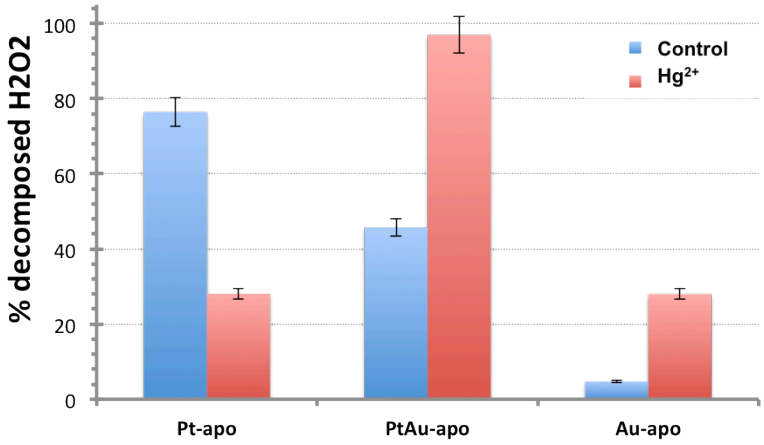

Figure 3.17. Percentage of decomposed H_2O_2 after one hour of reaction time. For the reactions Pt-apo, PtAu-apo or Au-apo (0.5 mg/ml), 10 mM PBS buffer and 2 mM H_2O_2 were used; 1 mM $HgCl_2$ was added to the reactions marked with red bars.

In the case of Pt-apo, the reactivity of the compound upon addition of Hg^{2+} decreased to very low reaction rates showing a clear inhibitory effect. A similar observation was done in the previously described section. In contrast, the reactivity of PtAu-apo and Au-apo was greatly enhanced with the addition of $HgCl_2$. In detail, PtAu-apo without Hg^{2+} decomposed 45 % of the initial H_2O_2, while upon adding Hg^{2+} it decomposed more than 95 % of the H_2O_2. More interestingly, Au-apo showed almost no activity prior to adding Hg^{2+}, but became active in presence of Hg^{2+} with a decomposition rate of more than 25% (Figure 3.17).

To verify the observed effect, the behavior of the mercury ions only within the reaction setup as well as in the detection method were analyzed first (Figure 3.18 A). After that the activity of apoferritin in contact with mercury ions was studied (Figure 3.18 B). Those tests showed that Hg^{2+} does not affect the peroxide decomposition and the reactivity of apoferritin. Thereafter, the reactivity of the hybrid nanoparticles was evaluated. The experiments showed that the enhancement of the reactivity must be due to some interaction between the gold nanoparticle and mercury.

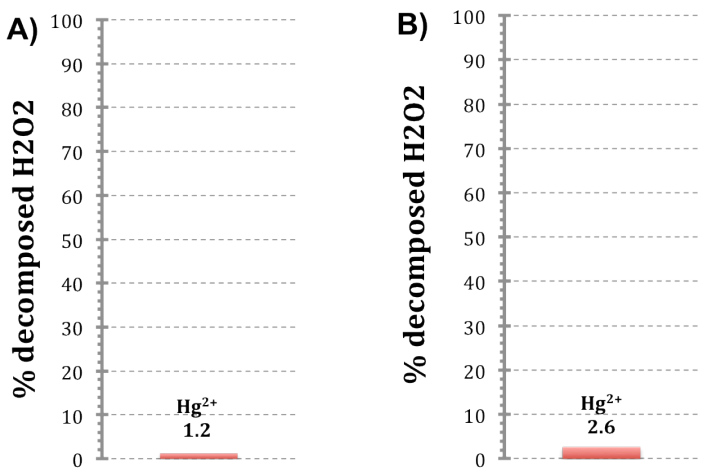

Figure 3.18. Percentage of decomposed H_2O_2 after one hour of reaction time. A) Control experiment without apoferritin under following conditions; 10 mM PBS buffer, 2 mM H_2O_2 and 1 mM Hg^{2+}. B) Control experiment with 0.5 mg/ml apoferritin, 10 mM PBS buffer, 2 mM H_2O_2 and 1mM Hg^{2+}.

The catalase activity of commercial PBS-stabilized gold nanoparticles was tested in similar conditions. Two further tests with commercial gold nanoparticles were performed, one without mercury, to be used as control, and one with 1 mM $HgCl_2$ added. The gold nanoparticle concentration used for the assay was calculated from the intensities at the UV-Vis spectra peaks.

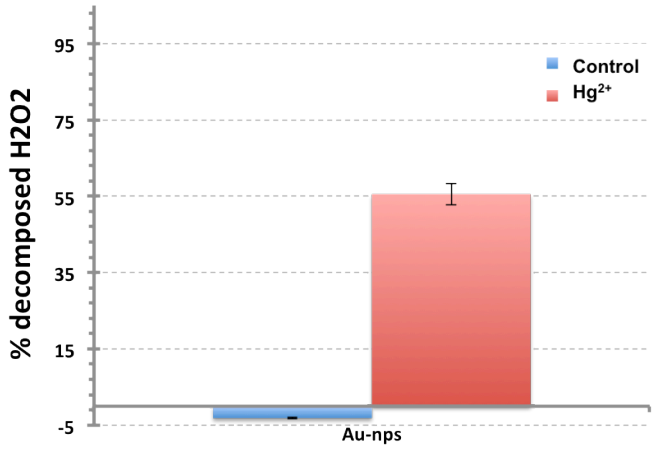

Figure 3.19. Percentage of decomposed H_2O_2 after one hour of reaction time. Control with commercial PBS-stabilized 10 nm Au nanoparticles in 10 mM PBS buffer and 2 mM H_2O_2; 1 mM of $HgCl_2$ was added for the test with Hg^{2+}.

The results presented in Figure 3.19 show that addition of Hg^{2+} results in significant enhancement on the peroxide decomposition activity. Even after 1 h of incubation, no H_2O_2 decomposition was observed from the control

sample. In presence of Hg^{2+}, more than 55 % of the initial H_2O_2 was decomposed, in analogy to the previous experiment performed with apoferritin-encapsulated gold nanoparticles.

The gold nanoparticles were characterized by SEM (Figure 3.20). The images show that without addition of Hg^{2+} the gold nanoparticles remain intact in the reaction conditions. The size and morphology of the nanoparticles were not affected (Figure 3.20 A). In contrast, a change in morphology was observed once Hg^{2+} was introduced into the reaction (Figure 3.20 B). Namely, the nanoparticles agglomerated and partly merged. A similar observation was recently done by Schopf C et al. upon exposing gold nanorods to Hg^{2+} [121].

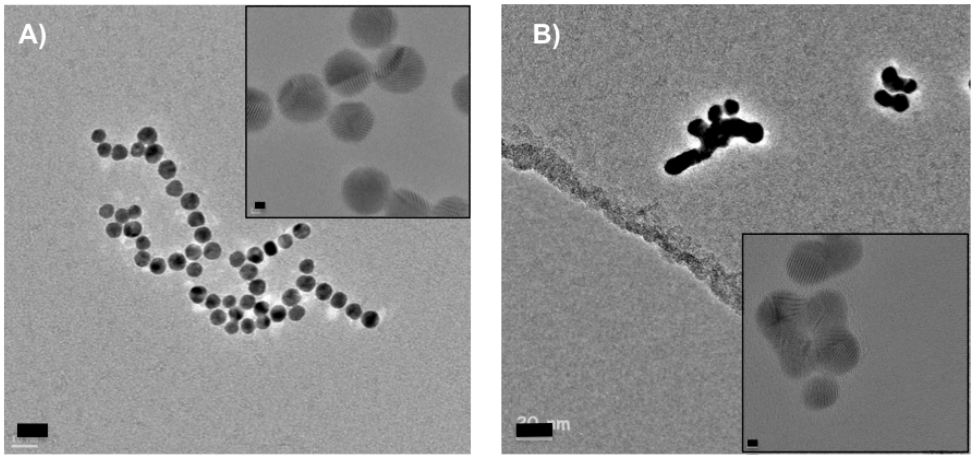

Figure 3.20. SEM images of PBS-stabilized Au nanoparticles after 1 h of reaction time with 2 mM H_2O_2 in PBS, A) without and B) with added Hg^{2+}. The insets show magnified images of the nanoparticles. (scale bar 10 nm; inset: 2 nm)

A reaction between Hg^{2+} and the Au nanoparticles clearly occurs, most likely even before initiating the peroxide decomposition activity. For a similar observation, Yi Juan Long et al. proposed that the Hg^{2+} becomes first reduced to Hg^0 by the citrate present on the surface of the Au nanoparticle and then the peroxide decomposition occurs with this composite [120]. However, in our system the commercial nanoparticles are stabilized with PBS and in case of Au-apo by the protein cover and not citrate. Therefore such interpretation is not applicable to our case.

3.2.2 Hg effect on sputtered Au

To further evaluate the material system, Au was sputter-deposited on silicon samples. Such deposited gold does not have stabilizing buffers or proteins, but neat gold surfaces are subjected to the reaction. The sample morphology was initially characterized by Atomic Force Microscopy (AFM) (Figure 3.21).

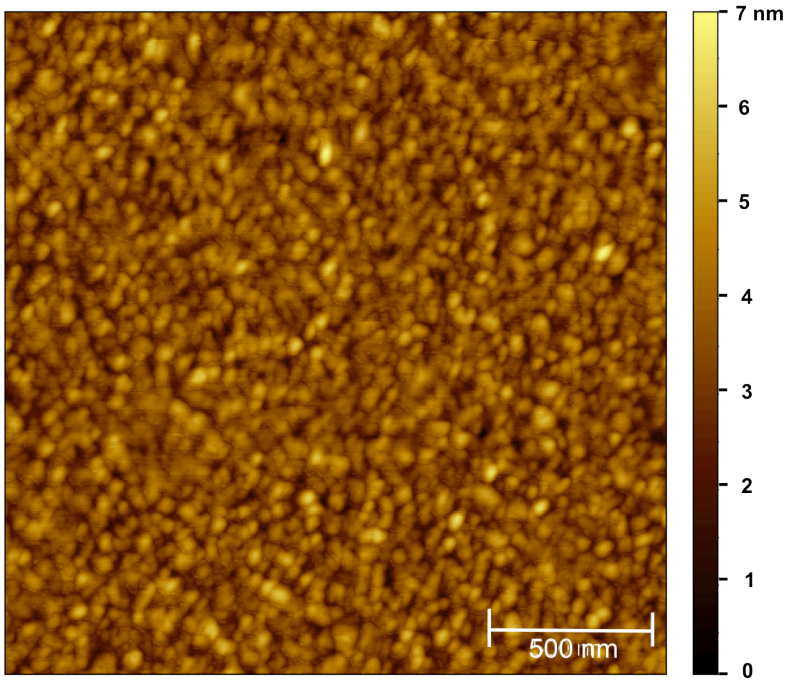

Figure 3.21. AFM image of the sputter-deposited gold surface.

The topological surface analysis of the gold samples showed uniform roughness. The nanoparticles forming the gold layer had an average size of 60 nm. While the size of the nanoparticles was larger than that of commercial PBS-stabilized nanoparticles, they are within the same order of magnitude, so the results from those analyses may be extrapolated to the commercial nanoparticles or Au-apo samples.

The sputter deposited gold samples were incubated in the same conditions as the nanoparticles. For the peroxide decomposition test, samples with and without added mercury were used. After one hour of reaction time, no serious visual changes were observed, thus longer incubation periods were applied.

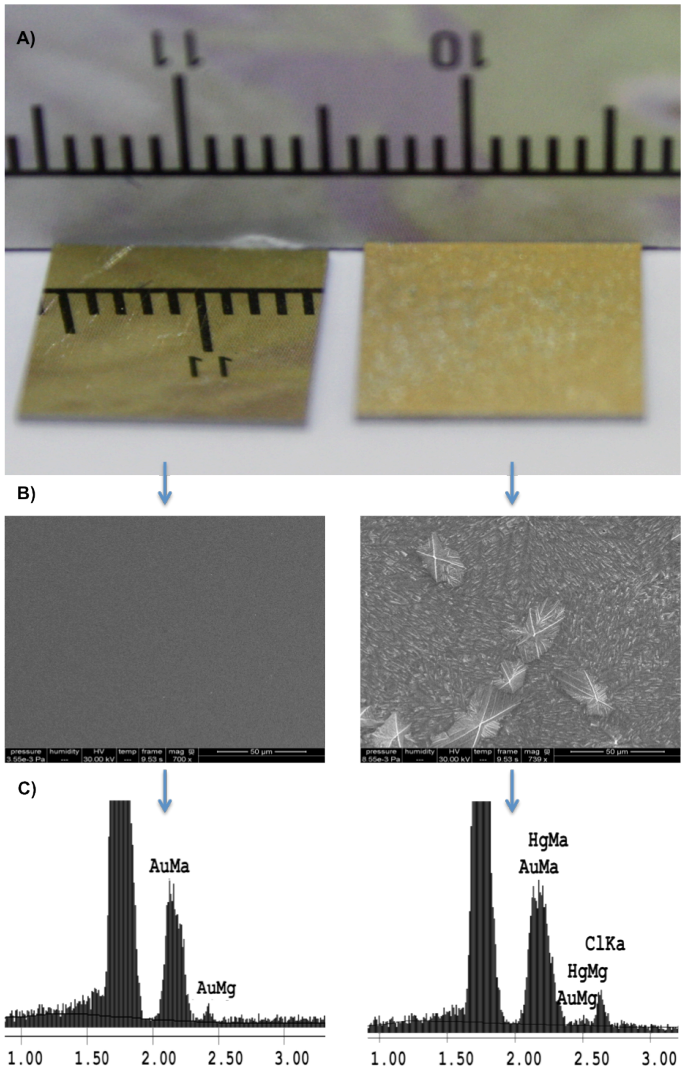

Figure 3.22. A) Photograph of sputter-deposited gold on Si. Both samples were treated with PBS, H_2O_2 and the right sample additionally with Hg^{2+}. B) SEM images of the samples shown in A). (Scale bar: 50 µm). C) EDX spectra of the samples shown in A).

In Figure 3.22A gold-sputtered silicon wafers are shown. The left sample was treated with PBS and H_2O_2, but not Hg^{2+} It shows no alteration in appearance, but remained mirror-like. The right sample was treated with Hg^{2+}, PBS and H_2O_2. After the overnight reaction some white precipitate was observed. The SEM images show some crystal formation covering the gold surface and the EDX spectra confirm that the crystals contain mercury and chlorine (Figure 3.22 C). The crystal formation may result from mercury (I) chloride (Hg_2Cl_2), which has a much lower solubility in water than other mercury salts. This insoluble salt probably precipitates onto the gold surface.

Hg_2Cl_2 is very difficult to solubilize. In order to prove the insolubility of the precipitate, the samples were rinsed in large amounts of water for one week. Only limited solubility of the precipitate was observed (Figure 3.23).

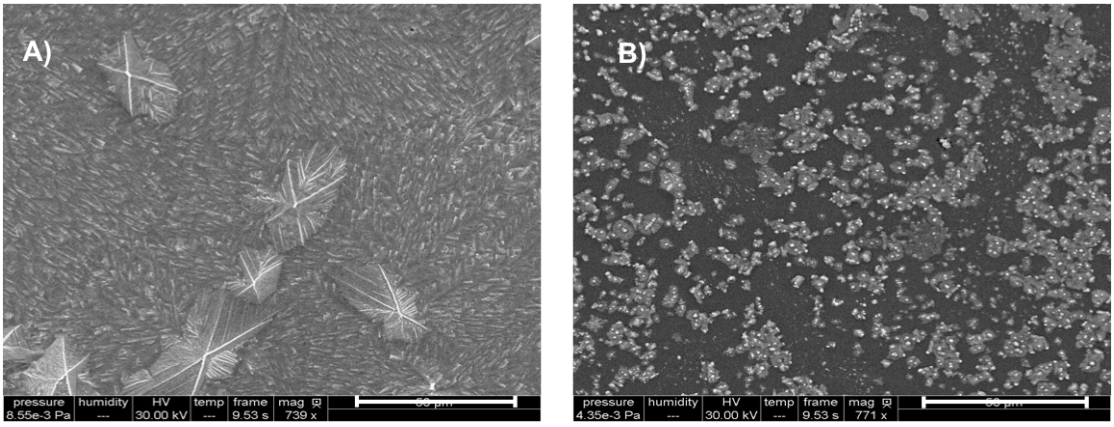

Figure 3.23. SEM images of the precipitates on gold surfaces A) before and B) after testing the solubility. The treatment involved immersing the sample in large amounts of water and changing the water every day.

The presence of Hg_2Cl_2 was chemically analyzed with a classical chemical detection reaction with ammonia, according to the following equation:

3.1 Equation

$$Hg_2Cl_2 + 2NH_3 \rightarrow Hg + Hg(NH_2)Cl + NH_4Cl$$

In Figure 3.24 one can see that the after a short exposure to ammonia vapors the sample turns black (Figure 3.22 A). Since the reaction occurs with Hg_2Cl_2 only, but not with $HgCl_2$, the color change proves the presence of Hg_2Cl_2. Consequently, it confirms that Hg^{2+} was reduced to Hg^{+} and the formed precipitate consists of Hg_2Cl_2.

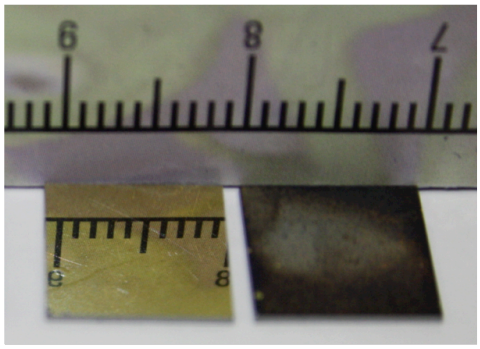

Figure 3.24. Photograph of gold-sputtered Si samples from Figure 3.22A after exposure to ammonia vapors. The right (black) sample contained precipitates after treatment with Hg^{2+} prior to the color change.

The presence of Hg_2Cl_2 implies that a redox reaction between Au and Hg^{2+} happens, which reduces the Hg^{2+}. First, a possible effect of H_2O_2 was analyzed. For that, a gold sample was treated with 1 mM $HgCl_2$ solution and PBS buffer, but without adding H_2O_2.

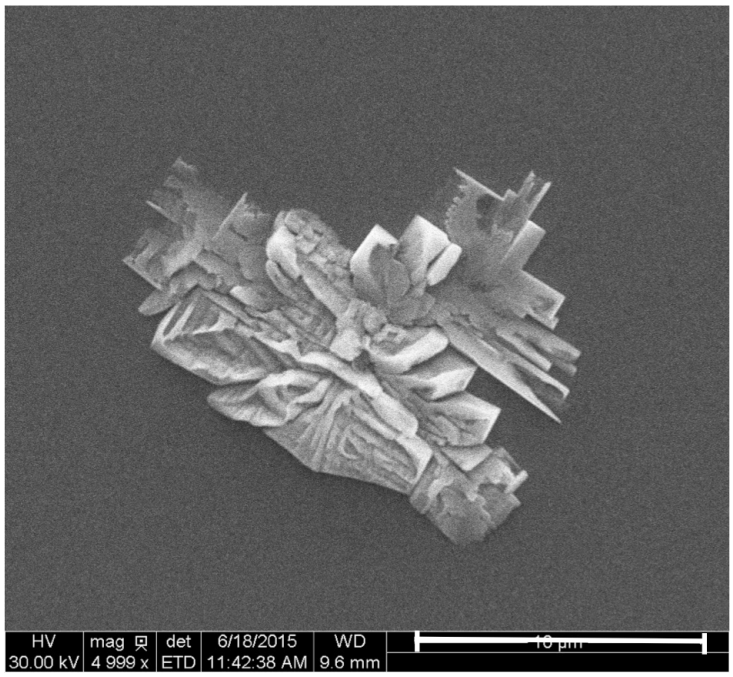

Figure 3.25. SEM image of a precipitate on the gold surface. The sample was treated with 1 mM $HgCl_2$ and 10 mM PBS buffer for 4 h. (Scale bar 10 µm)

After 4 h of reaction time, only few areas of the surface area contained small amounts of Hg_2Cl_2 precipitates on top of the gold surface (Figure 3.25). This shows that H_2O_2 is necessary for the formation of Hg_2Cl_2.

As control, silicon wafers without gold coverage were incubated in the same conditions. The SEM images did not show any precipitation and EDX spectra confirmed absence of Hg on the sample surface (Figure 3.26). Consequently, gold plays a critical role in this reaction.

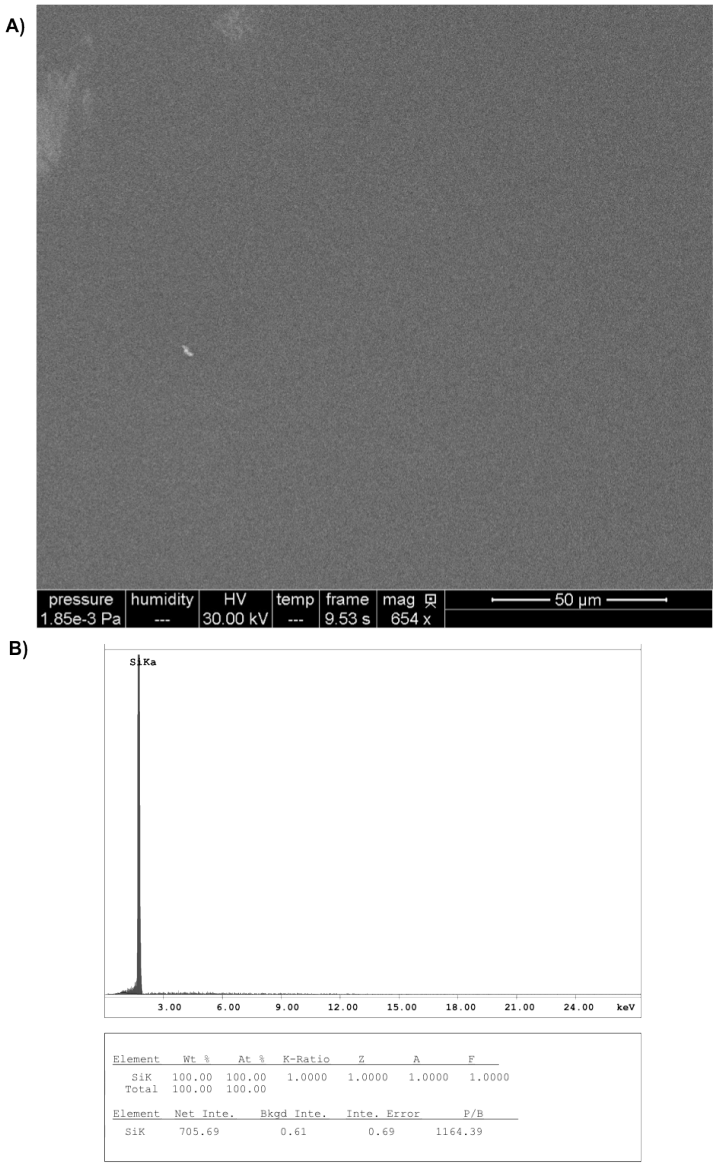

Figure 3.26. A) SEM image of a silicon wafer surface incubated over night with 1 mM $HgCl_2$, 10 mM PBS and 2 mM H_2O_2 (scale bar: 50 µm). A) EDX spectrum of the sample shown in A).

The two types of ions needed for the formation of Hg_2Cl_2 are Hg^+ and Cl^-. By removing the chloride from the reaction solution, the formation of the crystals on top of the gold surface should be suppressed. Removal of the PBS buffer resulted in the precipitation of crystals with different morphology and size

(Figure 3.27). This effect can be explained with PBS providing a significant amount of Cl^- ions to the solution, enforcing nucleation and precipitation very rapidly.

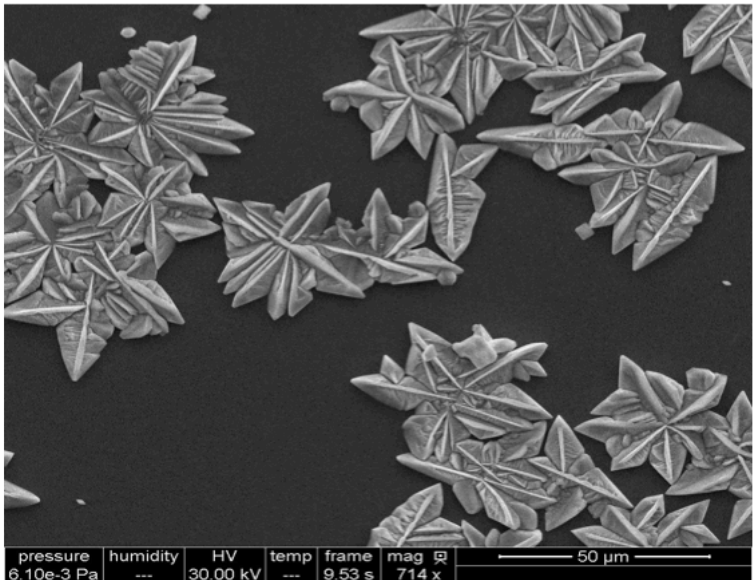

Figure 3.27. SEM image of precipitates on the gold surface. Treatment of the sample was done by immersing into a solution containing 1 mM $HgCl_2$ and 2 mM H_2O_2 over night.

The exact mechanism for the Hg^{2+} reduction is difficult to prove at this stage. One further experiment with the sputter-coated gold surface having been exposed to mercury vapors showed a strong reactivity with H_2O_2. For this experiment a gold-sputtered silicon wafer was introduced into a closed glass container containing a small droplet of liquid Hg and kept there overnight. The Hg was not in touch with the gold, but the Hg vapor should interact with the surface. The resulting gold surface showed a heavy reaction with concentrated H_2O_2. Untreated gold samples, as expected, did not show any activity. This indicates that the catalytic reactivity is related to an interaction of gold with mercury, most likely resulting in an amalgam. Such amalgam formation may be the reason for the fusion of nanoparticles observed in Figure 3.20. Therefore, the exposure to Hg^{2+} and the resulting high catalytic reactivity is very likely to originate from an intermediate Hg^0 formation and subsequent alloying with Au. From the performed experiments, it becomes clear that H_2O_2 plays an important role in this process. On the one hand, H_2O_2 may reduce Hg^{2+} to Hg^+, which would subsequently disproportionate to Hg^0

and Hg^{2+}, leaving behind some Hg^{+}, which will precipitate with Cl^{-}. However, this possible pathway implies that the splitting of H_2O_2 on gold will produce reducing agents, which cannot be easily evidenced. On the other hand, reactive oxygen may be formed on the gold, which could oxygenate the Hg^{2+} forming HgO. Such HgO, especially if freshly prepared, may not be very stable and it could decompose. Indeed, decomposition of HgO is also used in the production of mercury [122]. Regardless of the possible pathway, Hg^{0} will be generated and dissolve in Au to form an amalgam, which will act as catalyst for the decomposition of H_2O_2.

In order to clarify the nature of the previously shown H_2O_2 decomposition reaction being either a catalase- or a peroxidase-mimicking reaction, experiments with added 3, 3´, 5, 5´-tetramethylbenzidine (TMB) were performed. This chemical is commonly used as substrate for quantifying the peroxidase reaction kinetics. The negative results demonstrate that the decomposition reaction was not due to a peroxidase activity (Figure 3.28). In consequence, the reaction is described as catalase, which agrees with similar observations made by Chao-Wei Tseng et al. with platinum/gold nanoparticles [123].

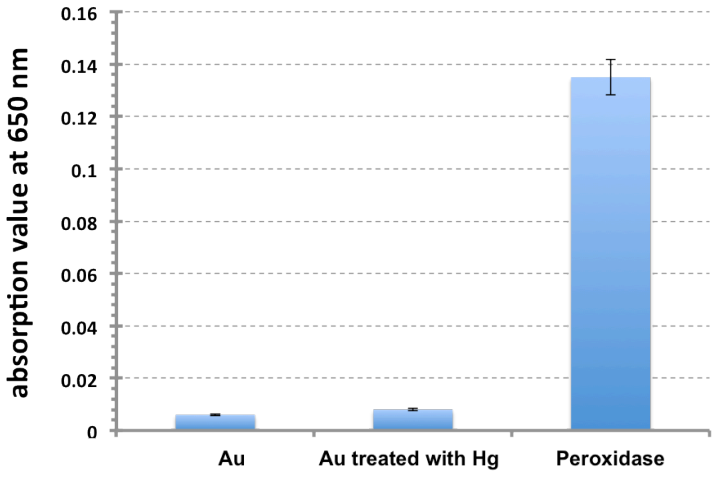

Figure 3.28. Peroxidase activity analysis performed by comparing the absorption of the oxidized state of TMB at 650 nm. The reaction was performed with the 1-Step™ TMB-Blotting Substrate Solution from Thermo scientific.

3.2.3 Summary

The effect of the mercury ions on the catalase mimetic activity was demonstrated for various metal nanoparticles encapsulated within the apoferritin cavity. The inhibitory effect on Pt-apo compounds was contrasted with an activation of the catalytic activity in case of Au-apo. The effect of mercury on Au was investigated. The enhanced reactivity is most likely related to an amalgam formation as a result from either a reduction of Hg^{2+} and disproportionation or decomposition of HgO, which will yield Hg^{0} to form an amalgam with gold. The precipitate was identified as Hg_2Cl_2, but appears to be a side product in this process.

Chapter 4

Enzyme mimetics: Ferroxidase

In the following chapter, the functionality of the ferritin protein for potential *in vitro* applications is investigated. The activities of the protein besides the naturally present functions are analyzed in a cellular environment and in biological conditions. Furthermore, the use of nanoparticles as the ferroxidase mimicking active site is evaluated [124,125]. The well-established method detailed in the previous chapter was applied for synthesizing metal nanoparticles within the cavities of human L-chain (apo-huFL) and H-chain (apo-huFH) apoferritins. Such compositions, especially with gold or platinum nanoparticles, are well-known to exhibit oxidase activities [93,94,100,124,126], giving rise to the assumption that ferroxidase activity can be induced.

The work described in the present chapter is published in the journal Chemical Communications from the Royal Society of Chemistry (RSC). Graphs, figures and parts of the text of the publication are reused in this thesis with permission of the publisher[127].

Article:

Semi-artificial and bioactive ferroxidase with nanoparticles as the active sites. L. Li, L. Zhang, **U. Carmona** and M. Knez. Chemical Communications., (2014), 50, 8021-8023

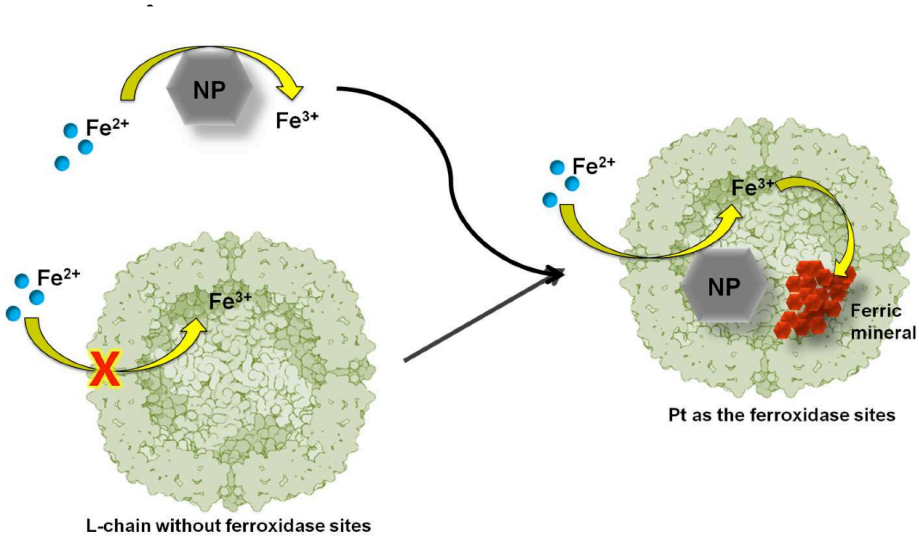

Schematic overview of the investigated catalytic reactions

4.1 Nanoparticles as active sites

Ferroxidases are important for the cellular transport and the storage of iron. This metal is essential for many biological enzymes, the O_2 transport, the immune defense, the energy metabolism, etc. Impaired ferroxidase activity is found to contribute to the generation or progress of diseases [128–130]. For example, the ferroxidase activity of ceruloplasmin is oxidatively inhibited by the Parkinson's disease [131]. The ferroxidase activity of the b-amyloid protein precursor (APP) is specifically inhibited by Zn^{2+} in Alzheimer's disease[132]. Besides APP, Zn^{2+} also inhibits the ferroxidase activity of heavy chain (21 kDa) ferritin. The L-chain (19 kDa) has no ferroxidase activity. However, in presence of L-chain proteins a more efficient mineralization of ferric ions occurs inside the cavity [133]. Thus, it appears feasible that a stable ferroxidase with efficient iron mineralization ability can be assembled from an inorganic ferroxidase mimic and L-chain proteins. The inorganic nanoparticle should oxidize ferrous ions to ferric ions, while the protein should mineralize the ferric ions, which would otherwise precipitate in an aqueous environment.

UV-vis spectroscopy was performed in order to determine the kinetics of the catalytic reactions of the composite upon iron oxidation under aerobic conditions. An absorbance peak at around 300 nm is characteristic of ferroxidase-catalyzed iron oxidation [134,135]. Rapid oxidation of iron within seconds was observed with apo-huFH, which exhibits natural ferroxidase activity (Figure 4.1A).

As expected, apo-huFL was ferroxidase inactive and the spectra at 250–300 nm showed only non-enzymatic iron oxidation. However, enzymatic iron oxidation was observed with platinum nanoparticle containing L-chain apoferritin (Pt-huFL). The stepwise progressing iron oxidation with Pt-huFL indicates that the mechanism of the nanoparticle surface-catalyzed ferroxidation is different to that of an amino acid residue-catalyzed reaction by apo-huFH, presumably related to fundamentally different binding, conversion and dissociation chemistry of substrates and products. Despite the slower conversion rate of Pt-huFL, similar total iron oxidation rates were achieved with both Pt-huFL and apo-huFH. Note that the ferroxidase activity of the

nanoparticles is material specific: encapsulated gold nanoparticles (Au-huFL) did not exhibit ferroxidase activity (Figure 4.1).

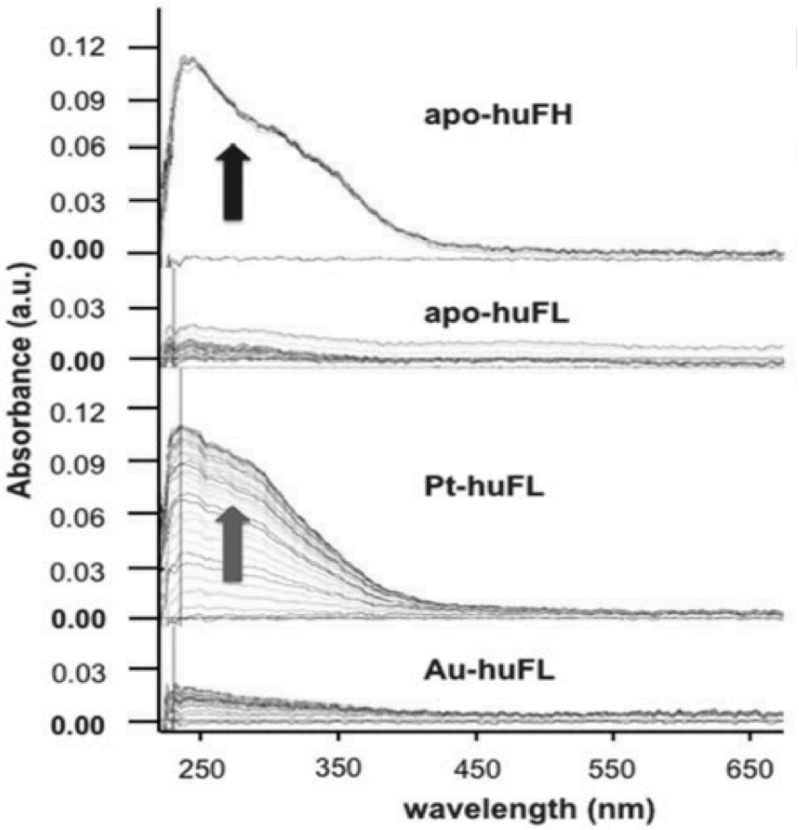

Figure 4.1. Ferroxidase activity of various apoferritins with and without Pt or Au nanoparticles, kinetically measured within 2 min of reaction time by UV-vis spectroscopy. The reaction was performed with 1 mM protein, 40 mM Fe^{2+} and 50 mM Tris at pH 7.0. Arrows indicate the ferroxidase activity evolution.

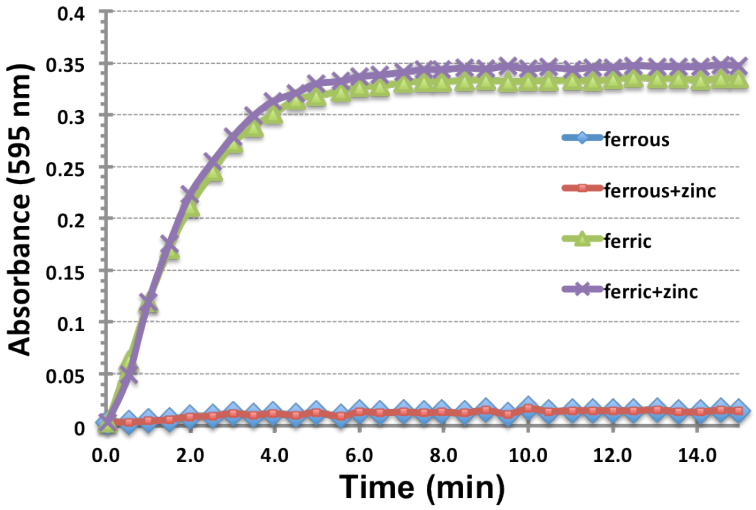

Figure 4.2. Influence of Zn^{2+} on the XO assay. 50 mM $ZnCl_2$ together with 25 µM $FeCl_3$ or 100 µM $(NH_4)_2Fe(SO_4)_2$ were added to the assay solution. The absorption at 595 nm was measured for 15 min in intervals of 30 s.

The evolution of Fe^{3+} was recorded with xylenol orange (XO). The XO assay is specific for Fe^{3+}, even in presence of Zn^{2+} (Figure 4.2), but will not react with Fe^{2+}. After 6 min almost all ferric ions present in the assay conditions were chelated. This high selectivity makes the XO assay very well suitable for the quantification of the ferric ions upon Pt-huFL catalyzed ferroxidation.

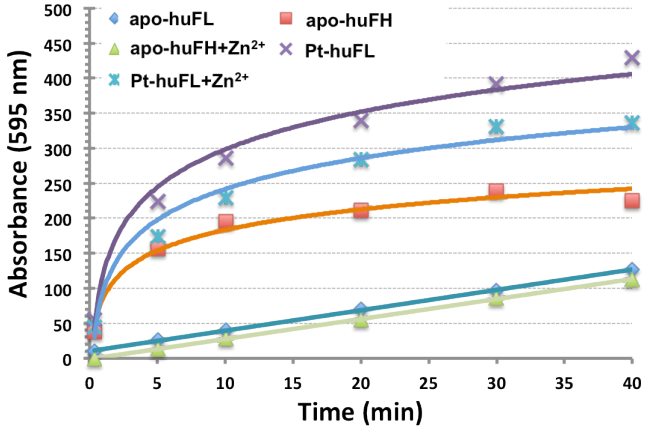

Figure 4.3. Fe^{3+} evolution over time upon reaction of various apoferritins with Fe^{2+}, with and without inhibitors, determined with the XO assay. The assay was performed with 0.2 mM protein, 10 mM Fe^{2+} and 50 mM Tris buffer at pH 7.0. The inhibition of the ferroxidase activity was performed in the presence of 10 mM Zn^{2+}.

With the XO assay, the formation of products (Fe^{3+}) is determined rather than the initial rate of ferroxidation, which allows for determination of the contribution of apo-huFL to the overall reaction. In this experiment, catalytic

conversion of ferrous to ferric ions was observed with apo-huFH and Pt-huFL and a non-enzymatic formation of ferric ions with apo-huFL (Figure 4.3). The evolution of ferric ions with apo-huFH reached a quasi plateau after 10 min, while it was incessant with Pt-huFL during the whole assay period, resulting in a higher final ferric concentration (Figure 4.3).

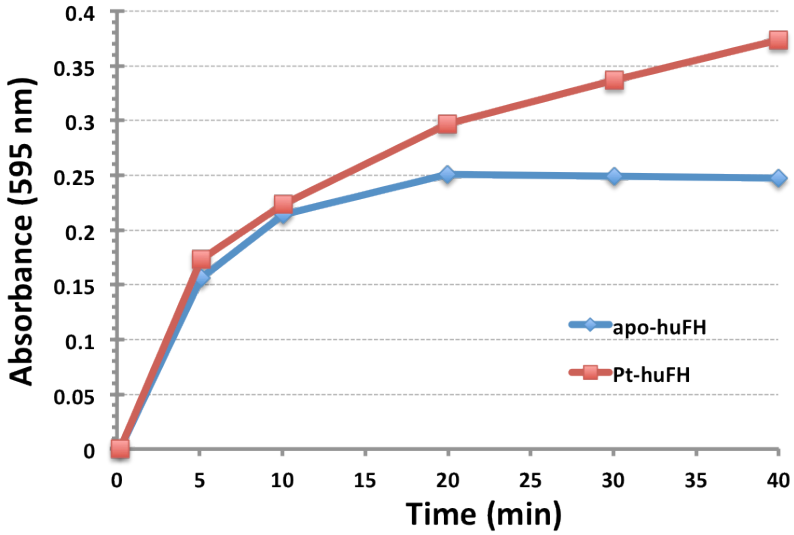

Figure 4.4 Ferroxidase activities of apo- and Pt-huFH measured with the XO assay. The assay was performed with 0.2 µM protein, 10 µM Fe^{2+} and 50 mM Tris buffer at pH 7.0.

The incessant production of Fe^{3+} with Pt-huFL indicates that the Pt nanoparticles altered the reaction mechanism and facilitated a more consistent ferroxidation than the natural ferroxidase apo-huFH (Figure 4.4). In order to verify whether or not the oxidized iron was mineralized within the hybrid ferroxidase, the iron content of the purified ferritin after the catalytic reaction was determined. The combination of Pt-nanoparticles and L-type chains showed the most efficient iron mineralization among the samples with more than 2000 iron ions per apoferritin on average (Figure 4.5). Pt-huFH showed second best values, even higher than recombinant apo-huFH.

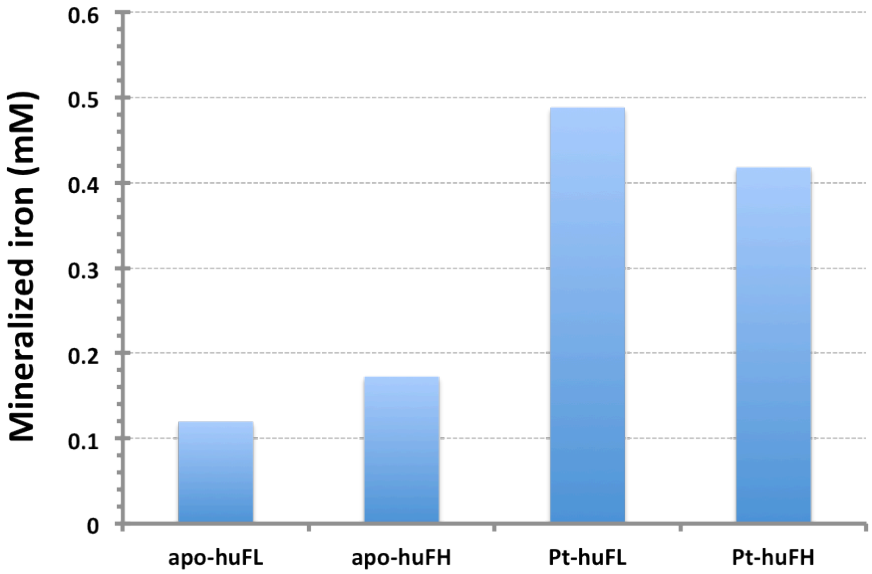

Figure 4.5. Quantification of mineralized iron in the protein after the mineralization reaction by XO.

In agreement with already published data, the ferroxidase activity of apo-huFH was strongly inhibited in presence of 10 mM Zn^{2+} (Figure 4.3). With Zn^{2+} the iron oxidation with apo-huFH turned non-enzymatic, similar to the case of the ferroxidase inactive apo-huFL. An occupation of the active site of the enzyme by Zn^{2+} may be the reason for the inhibition. This is rather unlikely to occur with nanoparticles as active sites.

According to the assay, Zn^{2+} slightly lowers the ferroxidase activity of Pt-huFL by around 10%, but does not change the manner of the iron conversion course. A similar effect was observed with Pt-huFH (Figure 4.6), which confirms that the different catalytic mechanism of Pt nanoparticles compared to enzymes induces inhibition resistance for Zn^{2+}. The small decrease of iron mineralization caused by Zn^{2+} may be due to a competitive transport of the two types of metal ions through the protein channels of apoferritin.

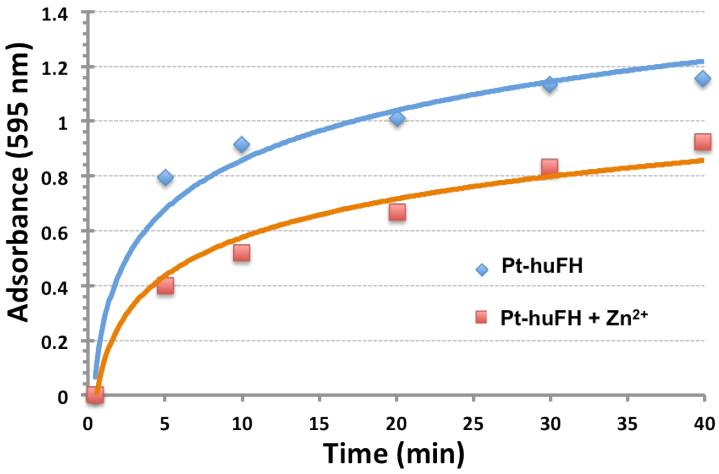

Figure 4.6. Inhibitory effect of 10 mM Zn^{2+} on the ferroxidase activity of Pt-huFH.

During the ferroxidation in mammalian apoferritins [136,137] evolution of H_2O_2 was observed. This can cause damage to ferritin in a deregulated cellular environment. The stabilities of the proteins were tested by treating recombinant L and H apoferritins and Pt-huFL compounds with H_2O_2 and Fe^{2+}. The native gel containing untreated and treated proteins confirms that H_2O_2 itself did not affect the electrophoretic mobility and band intensity of the apoferritins and Pt-huFL (Figure 4.7).

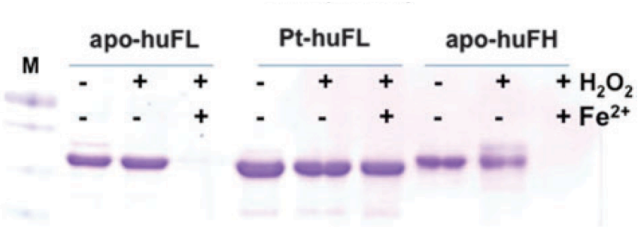

Figure 4.7. SDS-PAGE of recombinant apo-huFL, apo-huFH and Pt-huFL after treatment with 50 mM H_2O_2 and/or 500 mM Fe^{2+} for 30 min. M: protein weight marker.

However, apo-huFL or apo-huFH proteins completely degraded in simultaneous presence of both Fe^{2+} and H_2O_2 (Figure 4.7). A further observation that ferritin with a ferrihydrite core was degraded upon the treatment indicates the key role of iron (Figure 4.8). Apparently, the ferrous iron stimulated the degradation of apoferritin, regardless of its ferroxidase activity. An exception is seen with Pt-huFL. Identical treatment of Pt-huFL did

not result in protein degradation. The stabilization results from the Pt-nanoparticles being catalase and superoxide dismutase (SOD) active as described in the previous chapter. Such parallel activity efficiently detoxifies the harmful reactive oxygen species (ROS) evolving during the iron metabolism[82,95].

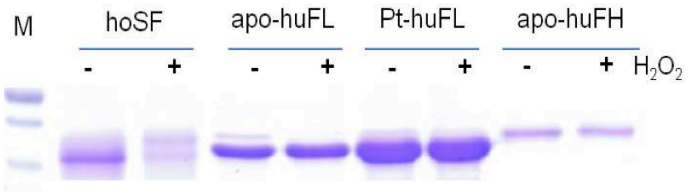

Figure 4.8. SDS-PAGE of native horse spleen ferritin (hoSF), recombinant human L and H apoferritin (apo-huFL and apo-huFH), and Pt-huFL after treatment with 100 mM H_2O_2. M: protein weight marker.

Resulting from those experiments, it can be stated that Pt nanoparticles as catalytically active sites enhance the ferroxidase activity, stability and the mineralization ability of apoferritin. Pt nanoparticles are resistant to the natural ferroxidase inhibitor Zn^{2+}, increase the resistant of the protein against ROS produced during the iron metabolism and improve the mineralization ability of apoferritin.

4.2 Bioactive Bioinorganic ferroxidase

Under natural circumstances, the human body already utilizes endogenous ferritin both as an antioxidant and for iron depletion [138,139]. It is expected that our bioinorganic ferroxidase nanozyme, especially the most active Pt-huFL, could actively influence the cellular iron level.

Normally, the cells cannot distinguish apoferritin (iron free) from ferritin (iron containing), which opens the possibility to trick the cells in an "iron-rich" delusion by incorporating Pt. *In vitro* tests demonstrate that deferoxamine (DFO), an iron-depletion drug, exhibits an iron-depletion effect on human intestinal Caco-2 cells, but not on human liver HepG2 cells (Figure 4.9 and Figure 4.10).

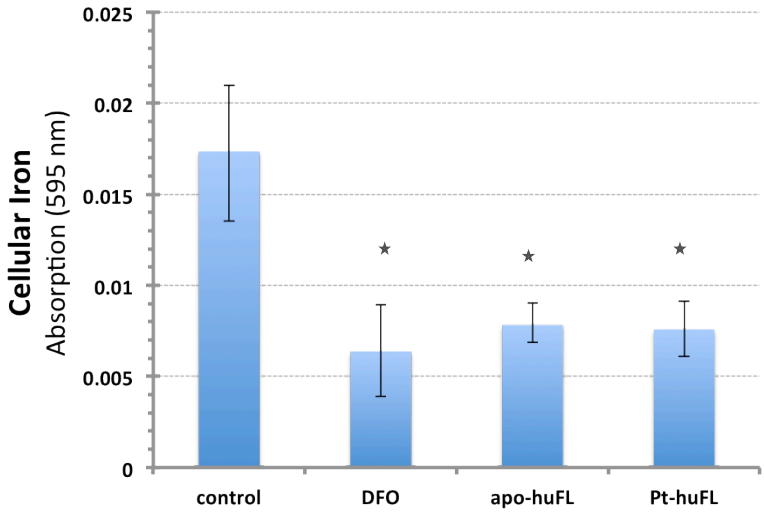

Figure 4.9. Cellular iron content of Caco-2 cells after treatment with deferoxamine (DFO, 300 mM), apo- and Pt-huFL (50 mg ml^{-1}), for 24 h. The values are presented by mean ± SD. *: $p < 0.001$.

The synthesized bioinorganic ferroxidase Pt-huFL depleted iron in both types of cells (Figure 4.9 and Figure 4.10). Furthermore, the ferritin composites did not inhibit the cellular iron uptake in the way DFO does when an excess of iron is supplemented (Figure 4.11). In such circumstances, apoferritin apparently acts as an iron sponge and a container for intracellular storage.

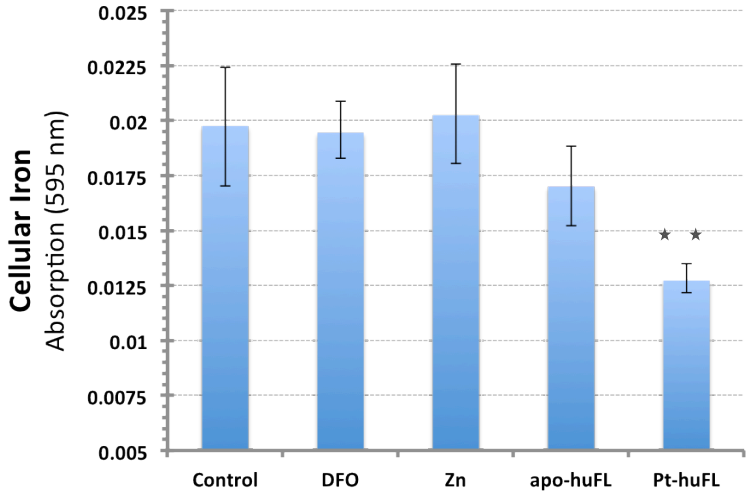

Figure 4.10. Cellular iron content in HepG2 cells after treatment with deferoxamine (DFO, 300 µM), apo- or Pt-huFL (50 µg/ml) for 24 h. The values are presented by mean ± SD. **: $p < 0.001$.

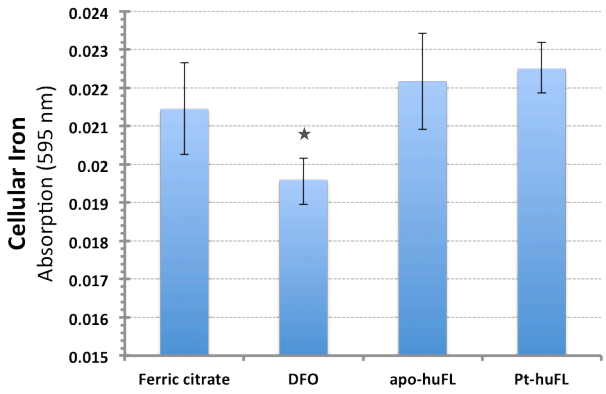

Figure 4.11. Cellular iron content in Caco-2 cells after the iron challenging with 40 μM Fe^{2+} together with 300 μM DFO , apo- or Pt-huFL (50 μg/ml) for 24 h. The values are presented by mean ± SD. *: $p < 0.05$.

In presence of Zn^{2+}, which also competitively inhibits the cellular iron uptake [140], the composites with ferroxidase activity stabilize the intracellular iron level (Figure 4.12). It seems that the ferroxidase activity of apoferritin plays a role in the cellular response to Zn^{2+}-induced inhibition. The significant difference between the ferroxidase active Pt-huFL and inactive apo-huFL indicates that the encapsulated ferroxidase-mimetic Pt nanoparticles facilitate a stabilizing effect of Pt-huFL on the intracellular iron. This observation also verifies the resistance of Pt-containing ferritin to the Zn^{2+}-induced inhibition in a cellular environment.

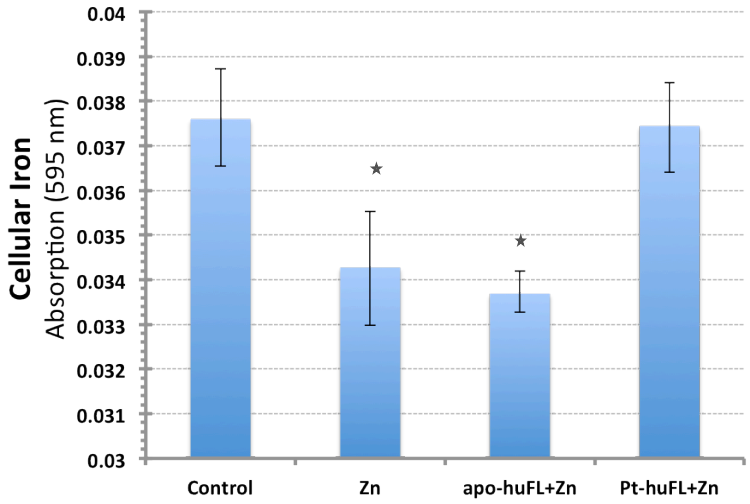

Figure 4.12. Cellular iron content in Caco-2 cells after treatment with deferoxamine (DFO, 300 mM), apo- and Pt-huFL (50 mg/ml), in presence of 40 mM Zn^{2+}. Untreated cells were used as internal control (contr.). The values are presented as mean SD. *$p < 0.001$.

In the introduction it was mentioned that the transferrin receptor (TfR) is a protein, which takes part in the iron uptake of a cell. In contrast, ferroportin is important for the iron release and an essential component in duodenal cells, which demark the critical first step the iron uptake of an organism.

Alterations in the cellular iron uptake through the transferrin receptor (TfR) and its export through ferroportin will directly influence the cellular iron content [53,55]. To address the mechanism of iron-regulation effects of Pt-huFL, the translational changes of TfR and ferroportin in Caco-2 and HepG2 cells were investigated upon treatment with DFO, apo-huFL or Pt-huFL. DFO had no effect on neither of the two iron transporters in Caco-2 and HepG2 cells (Figure 4.13). In contrast, Pt-huFL and apo-huFL increased the amount of TfR in the membranes of Caco-2 cells. Upon treatment with Pt-huFL an obvious increase of the intensity of the ferroportin band was observed in HepG2 cells. In contrast to the sole iron-depleting function of DFO, the ferritin-based composites influence the cellular iron apparently in a more biological and physiological way.

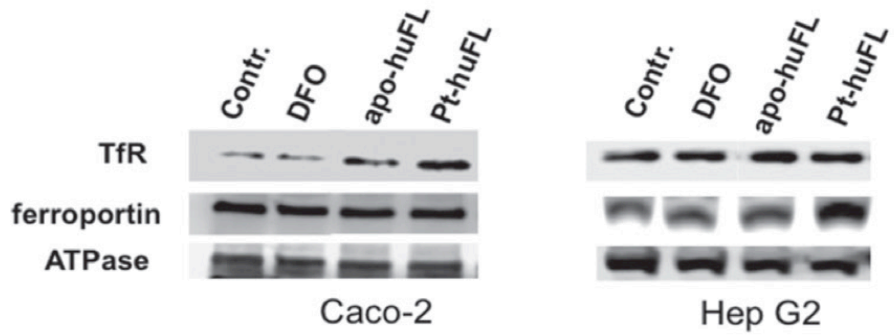

Figure 4.13. Western analysis of the transferrin receptor (TfR) and ferroportin amounts in the cell membrane fractions upon treatment with DFO, apo-huFL or Pt-huFL. ATPase was detected as the loading control.

4.3 Summary

In conclusion, the designed Pt nanoparticles encapsulated within apoferritin act as inhibitor-resistant bioinorganic ferroxidase and influence the cellular iron homeostasis. The hybrid nature of the engineered enzyme enables its cellular iron regulation in a physiologically favorable way, making beneficial

use of both the inorganic and biological constituents. The demonstrated possibility to use inorganic nanomaterials for fabrication of artificial enzymes shows new insights with great promise for enzyme design for future biomedical applications.

Chapter 5

Intrinsic properties of ferritin

The first part of this chapter describes a specific function of the L-chain protein, which was discovered upon investigation of the catalytic activity of homopolymeric L- and H-chain apoferritins. A redox reaction was designed with decoupled reduction and oxidation reactions, which were spatially separated by apoferritin proteins. While oxidized cytochrome c (Cyt-c) was used as electron acceptor under anaerobic conditions outside the apoferritin sphere, an iron oxidation inside the cavity should donate the electrons for the reduction. Neither homopolymeric human L- nor H-chain apoferritin (apo-huFL and apo-huFH) enabled a redox reaction. Heteropolymeric apoferritin, however, promoted the reaction demonstrating distinct functionality of the two different subunits. More detailed investigations of the mechanisms revealed that the H-chain protein serves as the electron source by catalyzing the iron oxidation inside the cavity, while the presence of the L-chain proteins allows for an electron transfer across the protein shell of ferritin, promoting the reduction of Cyt-c outside the cavity.

Besides, an extended analysis of the ferritin demineralization process was done. Special attention was paid to each type of the subunits of ferritin and their demineralization activity upon illumination with light or application of reduction agents. The demineralization was coupled with the Cyt-c reduction reaction. Finally, the effect of light on the cellular iron metabolism was investigated in order to gain more insight into the activity of ferritin.

The work described in the first part of the present chapter is published in the journal Chemical Communications from the Royal Society of Chemistry (RSC). Graphs, figures and parts of the text are reused with permission of the publisher [141].

Article:

Ferritin light-chain subunits: key elements for the electron transfer across the protein cage. **U. Carmona**, L. Li, L. Zhang and M. Knez. Chemical Communications. (2014), 50, 15358-15361

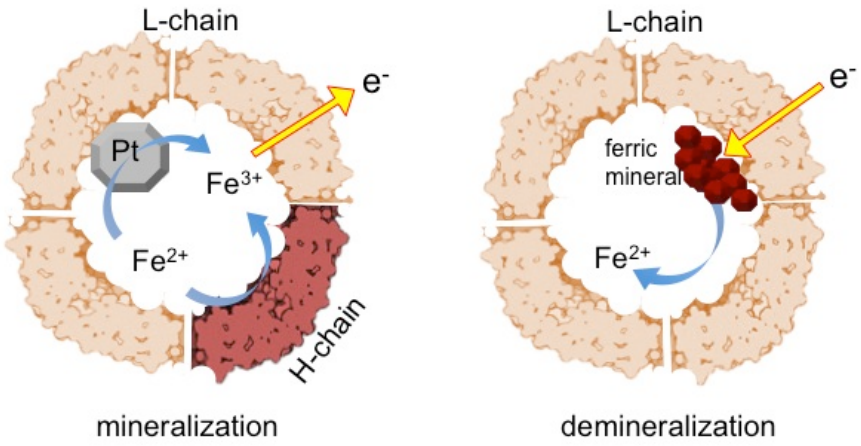

Schematic overview of the investigated reactions

5.1 The ferritin L-chain: key element for electron transport

In the earlier chapters ferritin was described as a suitable template for the synthesis of various nanoparticles, enabling a wide range of possible catalytic reactions. This range of catalytic activities may be further expanded considering that the encapsulating protein can add value to the reactivity of the synthetized hybrid compounds. Until now, only little attention was paid to the possible occurrence of such synergies. Therefore, a closer look to the intrinsic properties of ferritin is needed.

In vivo, the cytosolic ferritin has a tissue-specific ratio of H:L-chain proteins. The sole presence of L-chain protein in ferritin increases the stability and the iron mineralization ability of ferritin [136,142], but an increased fraction of the L-chain protein lowers the crystallization tendency of the mineral inside the cavity[143]. However, detailed understanding about the function of the L-chain proteins within the mineralization process is still lacking [144]. Although a catalytic activity is not identified, the L-chain protein appears to have important and specific biological roles, since all ferritin gene disorders identified so far involve the L-chain, but not the H-chain ferritin.

Initially, the intrinsic ferroxidase activity was evaluated for the recombinant apo-huFL or apo-huFH homopolymers and apo-hoSF. Since ferritin with its oxidized iron incorporated has a characteristic broad absorption peak with a maximum at 246 nm, the iron oxidation and the mineral formation was followed by UV-vis spectroscopy [134,135]. The recombinant apo-huFH has ferroxidase-active sites on each subunit, thus the apo-huFH expectedly showed a high ferroxidase activity (Figure 5.1). No ferroxidase activity was observed for apo-huFL, which was also expected, since the L-chains do not contain ferroxidase active sites. For comparison, we measured also the iron-oxidation activity of purified natural horse spleen apoferritin (apo-hoSF). Apo-hoSF is a heteropolymeric and L-chain rich apoferritin with 5-10 % H-chain content. With only 1 or 2 ferroxidase-active H-subunits per molecule, apo-hoSF showed a moderate ferroxidase activity. It oxidized iron gradually with much slower velocity than the pure H-chain apoferritin.

In aerobic conditions, the oxygen molecule acts as electron acceptor during iron oxidation and becomes reduced to water. Oxygen can easily reach the inner cavity and become reduced on-site with Fe^{2+} being oxidized. While oxygen can enter the cavity, many acceptor molecules may not be able or in need to enter the cavity of apoferritin. Cyt-c is a small heme protein and an important participant in the electron transport chain in mitochondria. With a molecular weight of around 12 kDa it is too large to pass through the channels of apoferritin and in this way enter the cavity. Since both oxidized and reduced Cyt-c show characteristic UV-vis absorption peaks, the absorption at 550 nm is well suitable to characterize the reduction reaction and was thus used in this study (Figure 5.2) [97,145].

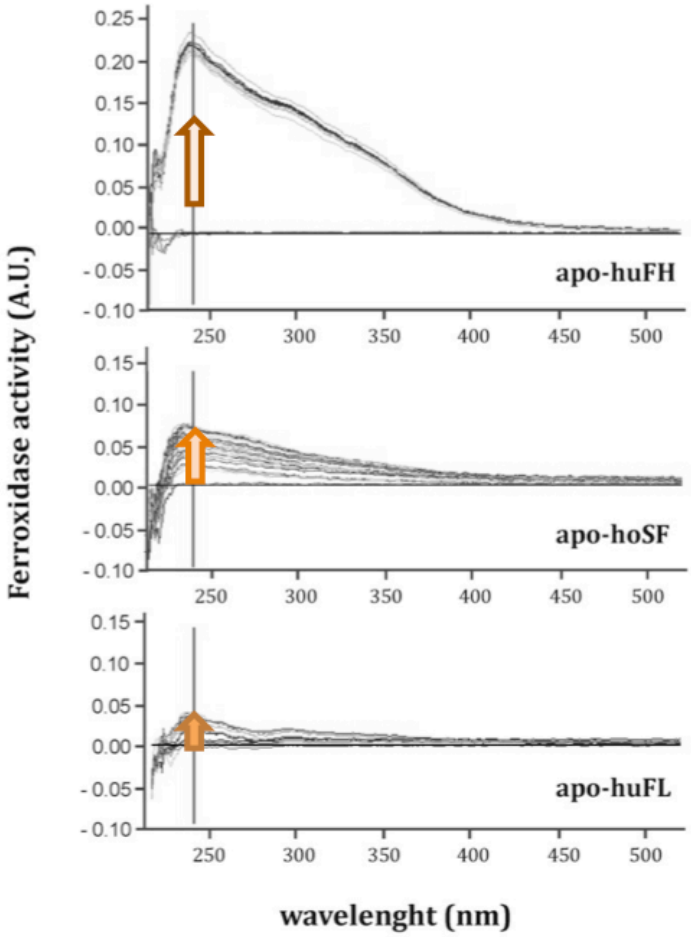

Figure 5.1. Ferroxidase activity characterized by UV-Vis spectroscopy. The reaction was carried out during 5 min with 0.15 mg/ml protein (apo-hoSF: horse spleen apoferritin; apo-huFH; apo-huFL. The arrows indicate the evolution of the peak characteristic for the iron oxidation.

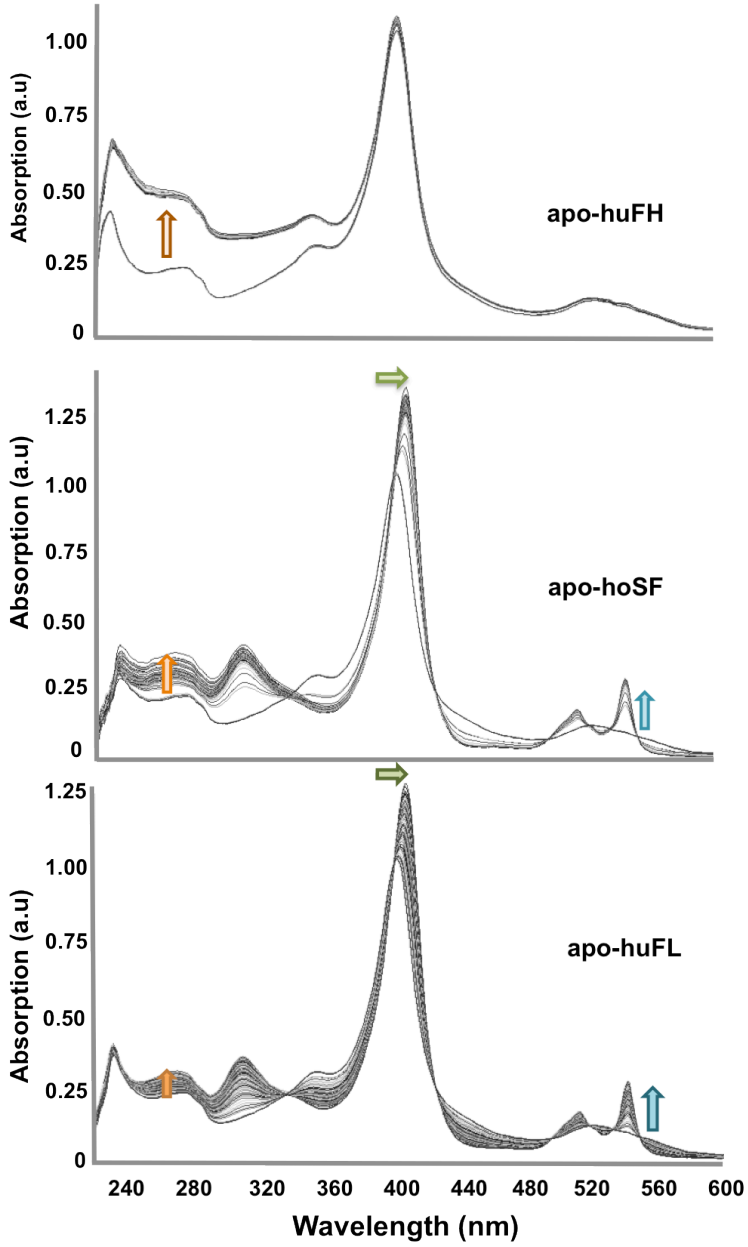

Figure 5.2. Cyt-c reduction activity measured with UV-Vis spectroscopy. The solution contained 0.15 mg/ml protein (apo-hoSF: horse spleen apoferritin; apo-huFH: human H-chain apoferritin and apo-huFL: human L-chain apoferritin), 10 μM oxidized Cyt-c, 10 mM Tris-HCl buffer at pH 7.0 and 50 μM $(NH_4)_2Fe(SO_4)_2$. Arrows indicate the evolution in the main peaks (orange: iron oxidation; green: main characteristic peak of Cyt-c; blue: reduced form of Cyt-c)

The reduction of Cyt-c was tracked by following the changes of the characteristic absorption peak at 550 nm and extracting the reaction kinetics (Figure 5.3). The reaction was set up for running in a non-oxidative environment. During the initial 90 s a quasi plateau is seen, which was used as reference value (100 % of oxidized Cyt-c). After 90 s the Fe^{2+} containing solution was added and after further 30 s the absorption spectrum was measured. After this measurement, the reaction kinetics was measured by acquiring absorption spectra in steps of 15 s.

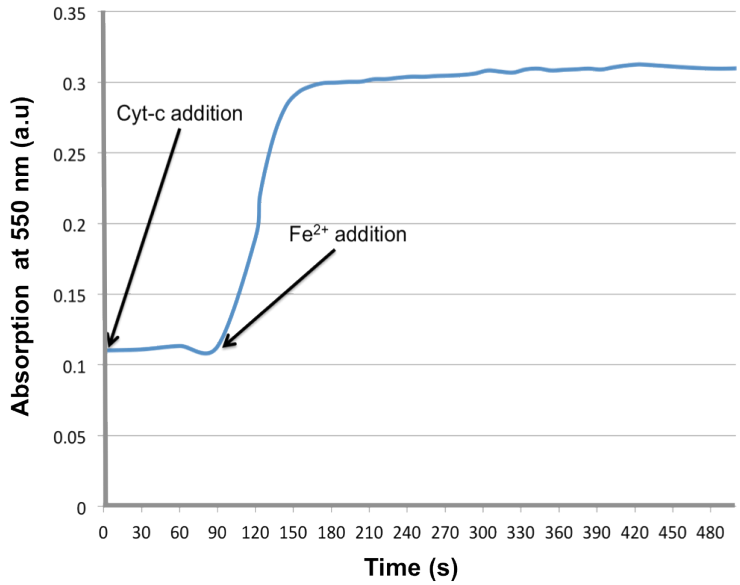

Figure 5.3. Reaction kinetics of the Cyt-c reduction. Formation of the reduced Cyt-c was followed by measuring the absorbance at 550 nm. The solution contained 0.30 mg/ml protein, 10 mM Tris-HCl buffer at pH 7.0, 10 µM Cyt-c and 50 µM $(NH_4)_2Fe(SO_4)_2$.

In agreement with previously published results, apo-hoSF catalyzed the redox reaction of Cyt-c with Fe^{2+} under anaerobic conditions (Figure 5.4). The increasing absorption between 250-300 nm shows the evolution of oxidized with progressing iron oxidation during the Cyt-c reduction (Figure 5.2). As expected, the reduction of Cyt-c was much slower with the homopolymeric ferroxidase-inactive apo-huFL (Figure 5.4). Surprisingly, however, the strongly ferroxidase-active apo-huFH also did not yield reduced Cyt-c. Its activity was similar to that of the bovine serum albumin (BSA) protein, which served as the negative control.

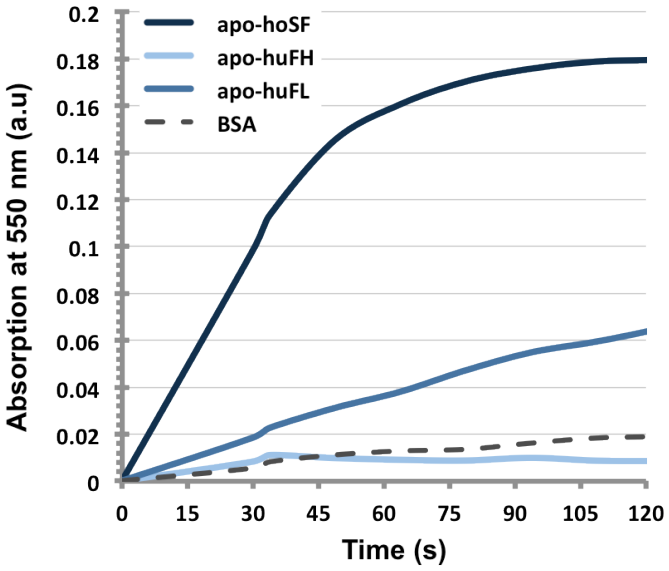

Figure 5.4. Formation of reduced Cyt-c from changes in the characteristic absorption at 550 nm over time. The reaction was carried out with 0.30 mg/ml protein, 10 µM oxidized Cyt-c and 50 µM Fe^{2+}.

In order to confirm that the different activities of the three types of apoferritin were due to the distinct properties of the two involved types of subunits, the possibility that the observed Cyt-c reduction was caused by superoxide had to be ruled out. Superoxide may be produced during the apoferritin-catalyzed iron oxidation and could affect the redox reaction [146,147].

The use of Dojindo`s tetrazolium salt as indicator confirmed that no superoxide is formed during the anaerobic iron oxidation under our experimental conditions [148]. This was further confirmed by following the kinetics of the apo-hoSF-catalyzed Cyt-c reduction with addition of superoxide dismutase (SOD), which efficiently inhibits the superoxide-induced reduction of Cyt-c[146]. The reduction of Cyt-c by apo-hoSF was not inhibited in presence of SOD (Figure 5.5), confirming that superoxide was not involved in the Cyt-c reduction in our experiments. Therefore, the L- and H-chains obviously play distinct roles in the electron transfer chain between iron and Cyt-c.

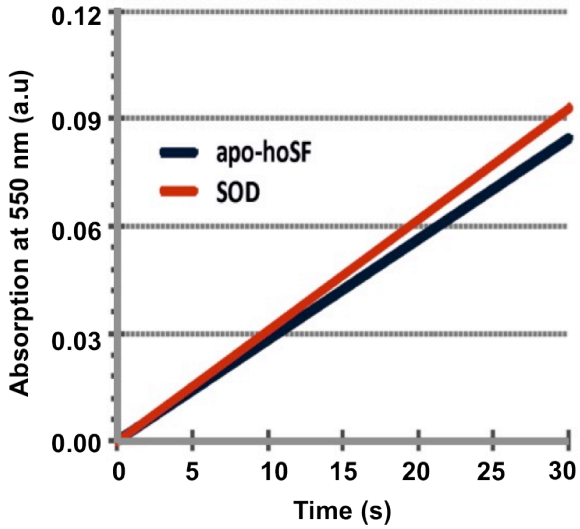

Figure 5.5. Cyt-c reduction with apo-hoSF with or without addition of 10 µg/ml superoxide dismutase (SOD).

The stronger activity of the heteropolymeric apo-hoSF in the Cyt-c reduction reaction compared to that of the homopolymeric apoferritin implies that only the combination of the two types of protein subunits makes the assembled apoferritin seriously active. The involved reaction pathway can be simplistically seen as: 1) the oxidation of Fe^{2+} to Fe^{3+}; 2) the transport of the electrons from iron across the protein shell and reduction of Cyt-c. The inability of apo-huFH to reduce Cyt-c indicates that the H-chain protein, having ferroxidase activity, can carry out the first step only. Thus it can be assumed that the L-chain proteins in the heteropolymer are responsible for the electron transfer.

In order to verify this assumption, homopolymeric apo-huFL and apo-huFH were disassembled and again reassembled in distinct proportions following the previously described method[144]. In this way a variety of heteropolymeric apoferritins containing 10, 50 and 90 % L-chain proteins on the average was obtained. Figure 5.6 shows the measured Cyt-c reduction activities of these new heteropolymeric apoferritins given as the percentage of reduced Cyt-c after 30 s reaction time. Upon increased percentage of L-chain proteins in the apoferritin molecules, the activity increased considerably. The heteropolymer with 50 % L-chain proteins had a six-fold higher activity in comparison to the H-chain homopolymer. An 18-fold increase was achieved once the apoferritin contained 90 % L-chain proteins, which roughly corresponds to the mixture in

the natural heteropolymeric apo-hoSF. Note that the activity enhancement could only be achieved with variation of the L:H proportion within the heteropolymer. A simple coexistence of H- and L- homopolymers in a 1:9 ratio in the solution did not yield any activity increase (Figure 5.6). Thus, the utilized apoferritin needs to contain L-chain proteins to transfer the electrons evolving during the iron oxidation at the H-chain protein.

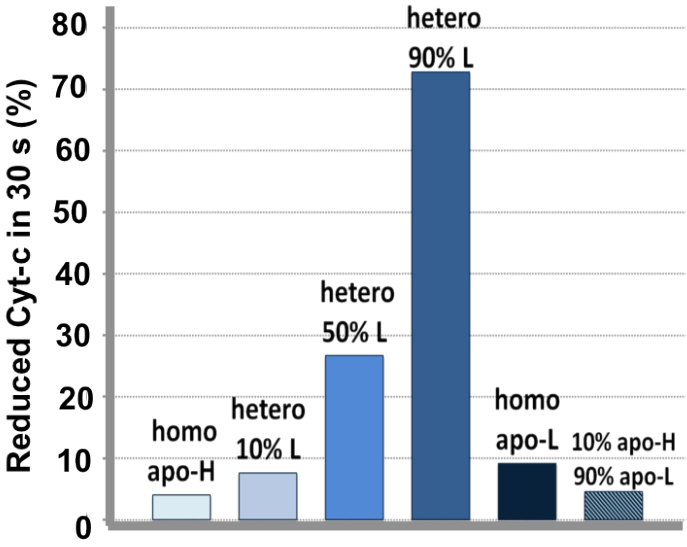

Figure 5.6. Percentage of reduced cytochrome c (Cyt-c) after 30 s of reaction time with 0.15 mg/ml protein (H- or L-chain apoferritin (apo-H or apo-L) and heteropolymeric apoferritin with the indicated L-chain protein content). 10 µM oxidized Cyt-c was added to the reaction solution.

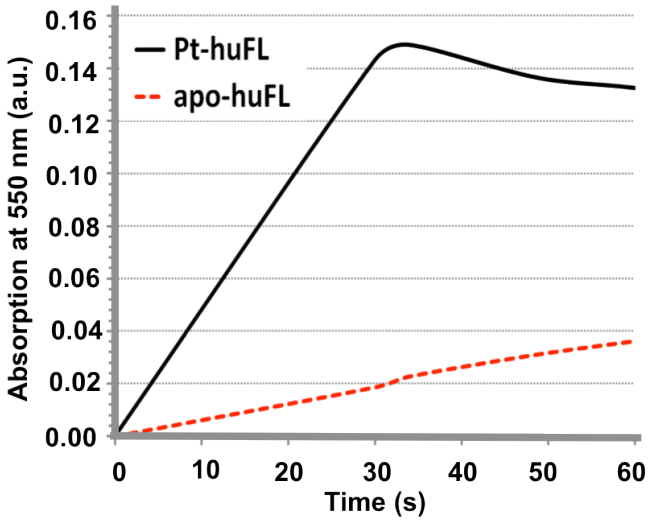

Figure 5.7. Comparison of the Cyt-c reduction by human L-chain apoferritin (apo-huFL) with or without Pt nanoparticles within its cavity (Pt-huFL).

The question occurs whether or not the interactions between H- and L-chain proteins are necessary for the electron transport. To confirm that the L-chain proteins are the only responsible unit for the electron transfer, it was necessary to find a substitute for the H-chain proteins as the electron source. Pt nanoparticles synthesized within apoferritin can act as active sites for the Fe^{2+} oxidation reaction, which was already described in the previous chapter [127]. Once synthesized within L-chain apoferritin, such artificial ferroxidases should make the H-chain proteins obsolete. We evaluated the activity of such L-chain apoferritins with Pt nanoparticles embedded in their cavity (Pt-huFL) for the reduction of Cyt-c. Indeed, the Pt-huFL was catalytically active (Figure 5.7) demonstrating that the H-chain proteins are not required for the electron transfer. The electron transfer is a specific property of the L-chain proteins.

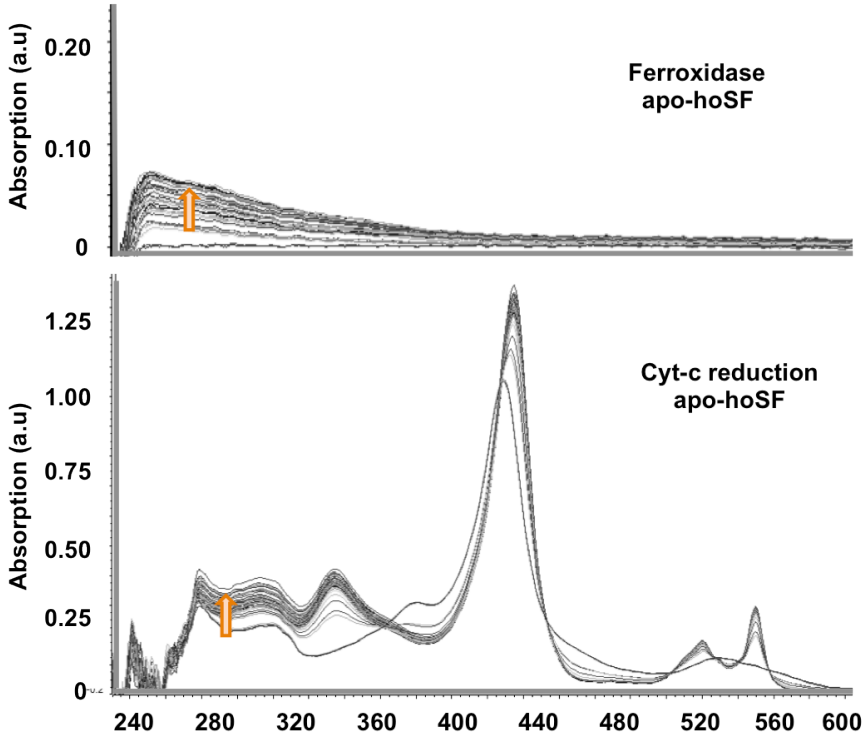

Figure 5.8. Upper spectra: Ferroxidase activity of horse spleen apoferritin (apo-hoSF) characterized with UV-Vis spectroscopy. The solution contained 0.15 mg/ml protein, 10 mM Tris-HCl buffer at pH 7.0 and 50 µM $(NH_4)_2Fe(SO_4)_2$. Lower spectra: Cyt-c reduction activity of apo-hoSF characterized with UV-Vis spectroscopy. The solution contained 0.15 mg/ml protein, 10 µM Cyt-c, 10 mM Tris-HCl buffer at pH 7.0 and 50 µM $(NH_4)_2Fe(SO_4)_2$. Arrows indicate the evolution of the peaks characteristic of the iron oxidation.

The Cyt-c reduction provides the evidence of outward electron transport from the interior iron oxidation site and facilitates the iron mineralization within ferritin (Figure 5.8). In natural circumstances this may be important for the newly synthesized apoferritin to mineralize and store excess iron. Even upon iron oxidation under aerobic conditions, the possibility for the electrons to be transferred across the protein shell may speed up the reaction while circumventing the rate determining step, the diffusion of reactants such as O_2 into the ferritin cavity [62]. But for the mineral containing ferritin the reverse electron transport was necessary in order to reduce the interior Fe^{3+} and demineralize iron where needed.

5.2 Ferritin demineralization

In order to verify whether or not the electron transport through the L-chain protein is bi-directional, NADH/FMN was used as electron donor for a demineralization of ferritin [149]. We compared the demineralization of the human homopolymeric L- and H-chain ferritin with a similar iron mineral content.

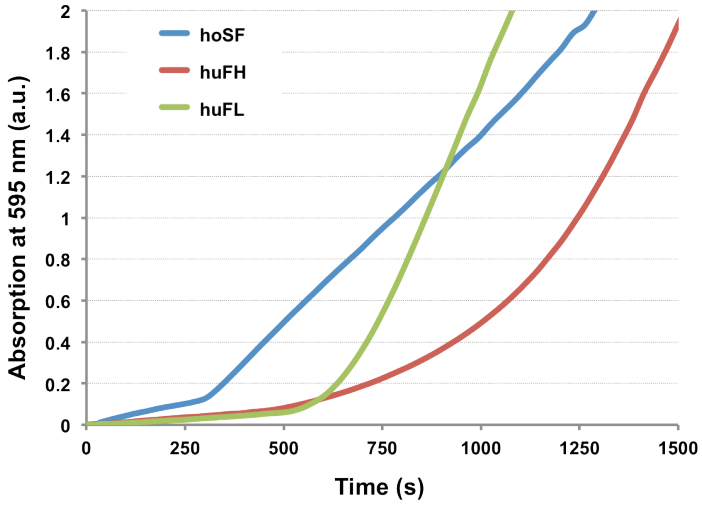

Figure 5.9. Comparison of the demineralization rate of natural horse spleen ferritin (hoSF), and recombinant human L- and H-ferritin (huFL and huFH).

As shown in Figure 5.9, the demineralization of horse spleen ferritin started more rapidly than that of huFL and huFH, but the release speed was slower than in the case of the recombinant L-chain homopolymer. The demineralization of L-chain ferritin started earlier and was faster than that of H-chain ferritin. Since NADH/FMN molecules are too large to enter the ferritin cavity, the reduction of the ferritin mineral through a direct contact with the reducing agent was avoided. The differences in the reaction velocity reflect serious differences in the electron transportability between the L- and H-chain proteins and consequently the demineralization of ferritin.

The ferritin L-chain protein can transport an electron through the protein shell in both directions [141]. From that perspective, the iron oxidation, which was facilitated with assistance of L-chain proteins, could also be inverted to a reduction of the mineral. This may be possible by applying chemistry or electromagnetic radiation, for example, light.

5.3 Light-induced demineralization

In previous studies it was proposed that the ferrihydrite core in ferritin may act as photocatalyst for redox reactions [150–152]. Such effect may result from the fact that the mineral is a semiconductor and able to generate an electron-hole pair upon irradiation with UV-vis light. The UV-Vis irradiation generates a catalyst for the redox reaction [153], but also a side effect: it can also act as a photocorrosive degrading the mineral itself [154].

The degradation of the iron mineral within ferritin and the release of iron from ferritin was studied in order to estimate the amount and availability of iron. For this purpose, light sources with various wavelengths were applied. Light emitting diodes (LEDs) were chosen, since they emit in well-defined wavelengths. Four colors, blue, green, yellow and red were used for the demineralization of horse spleen ferritin (Figure 10).

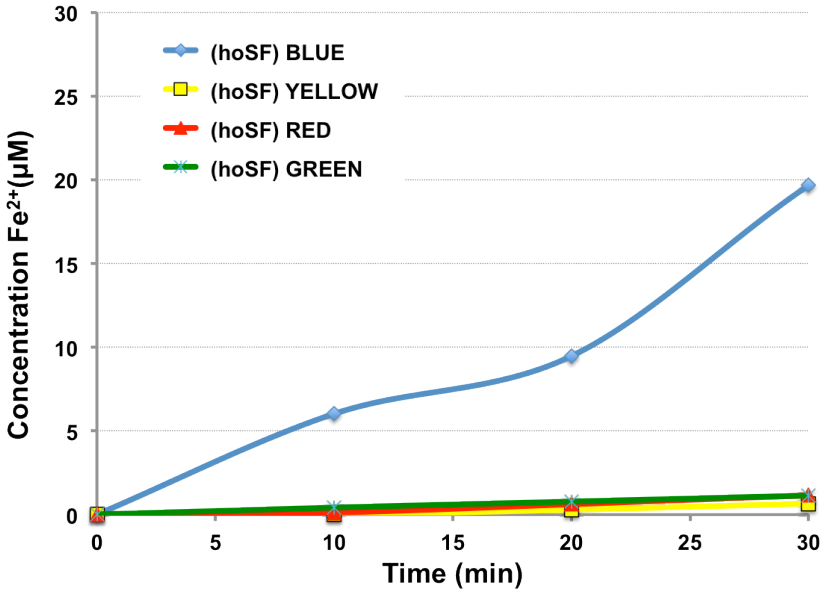

Figure 5.10. Demineralization of horse spleen ferritin (hoSF) upon irradiation with blue, green, yellow or red LEDs.

The curves in Figure 5.10 show that only the most energetic, blue light is able to reduce the ferritin mineral, while the green, yellow or red LEDs even after 30 min of irradiation had no effect on the iron. For identifying the optimal testing conditions, the light-induced reaction with horse Spleen Ferritin was further analyzed in presence of various buffers.

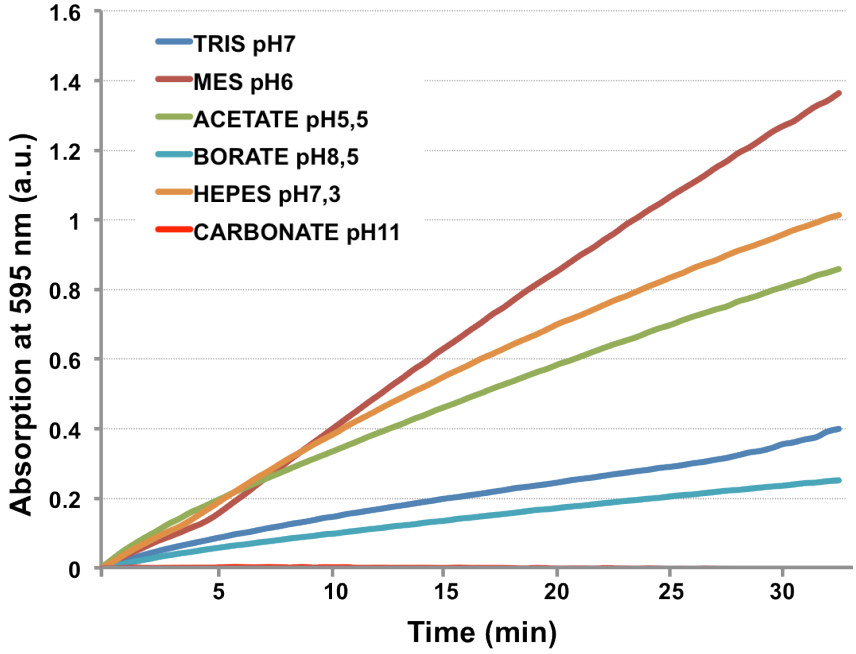

Figure 5.11. Demineralization of hoSF was quantified by measuring the complex of released iron with ferene S in presence of various buffers and pH values as indicated in the legend.

Figure 5.11 shows that in acidic conditions the release of iron from ferritin was much faster than in neutral or basic conditions, with one exception: in presence of HEPES buffer with a pH close to the physiological pH, the release of iron was faster than expected. HEPES buffer may potentially react with iron [155]. Due to this potential reactivity it was considered not being suitable for the further reactions.

Tris buffer-stabilized mineral reduction and release from ferritin can be more easily controlled over time due to the rather slow release kinetics. Furthermore, the pH is close to physiological conditions, which is optimal for the Cyt-c reduction. Therefore, Tris buffer with pH 7 was considered as the most appropriate buffer for the following experiments.

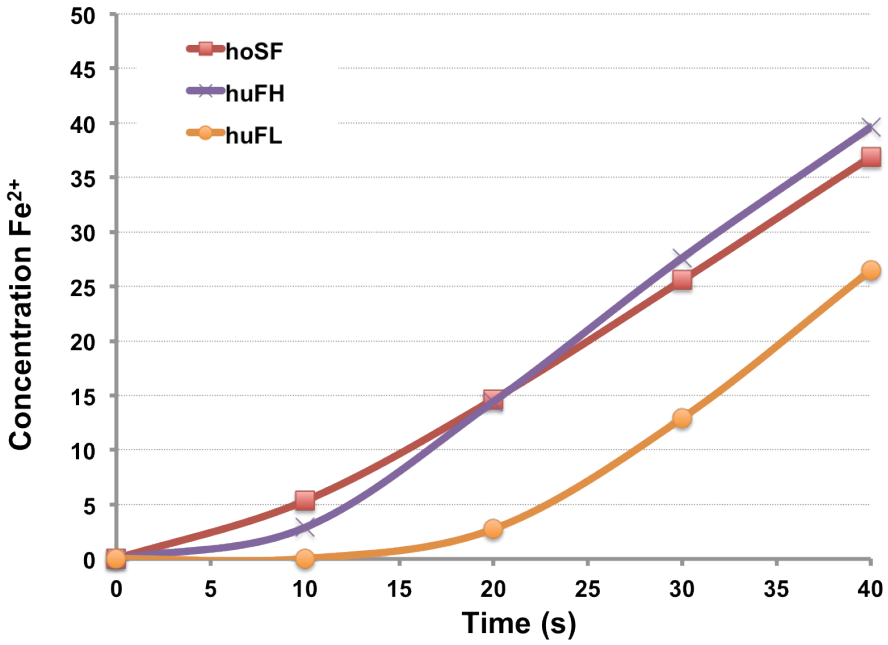

Figure 5.12. Demineralization of three different types of ferritin, horse spleen ferritin (hoSF), human H-chain ferritin (huFH) and human L-chain ferritin (huFL), quantified by measuring the complex of ferene S with the released iron.

With the defined buffer (Tris) and light source (blue LED), the demineralization of iron in horse spleen ferritin and human L- and H-chain ferritins was quantified by measuring the concentration of the complex of Ferene S with the released Fe^{2+} ions over time (Figure 5.12). It was found that the two ferritins that contain ferroxidase activity show a faster release of iron in comparison to

human L-chain ferritin that lacks such activity. Obviously, the ferroxidase activity is of importance for the demineralization. In order to verify this, an analogous experiment with the mineral without the surrounding protein was performed.

For this purpose, in advance of the demineralization reaction, proteinase K was used for the digestion of the protein shell of ferritin. This should facilitate the direct contact of the iron mineral with ferene S. The mineral was exposed directly to the light and reduced. The reduced iron was immediately complexed by Ferene S. This procedure allows analyzing the contribution of the ferritin shell to the process and at the same time confirming the degrading effect of the light on the ferritin mineral.

Figure 5.13 shows the demineralization kinetics for each of the utilized ferritin minerals. From the demineralization kinetics two differences can be seen after comparison with the experiment that included the protein (Figure 5.12).

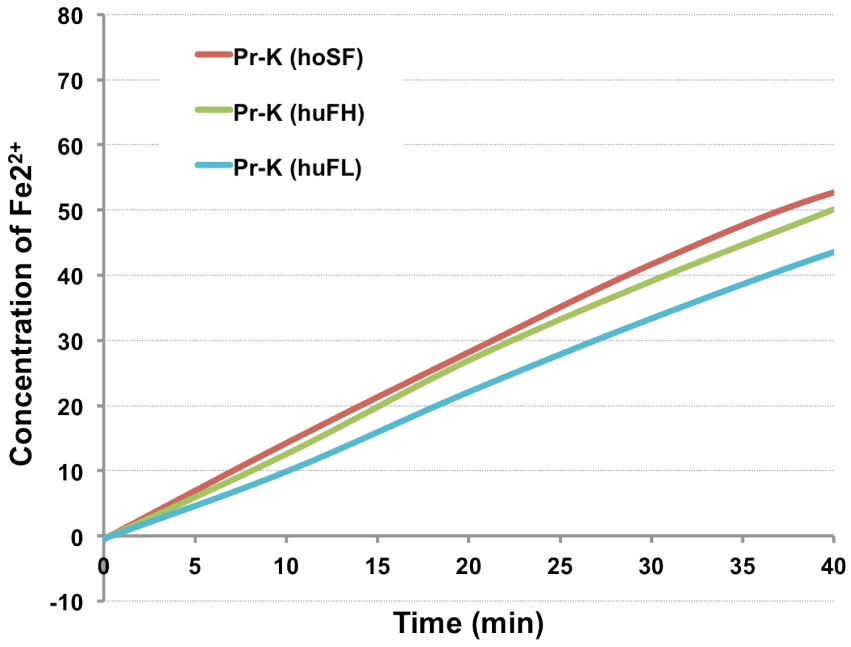

Figure 5.13. Demineralization of the minerals obtained from three different ferritins after digestion of the protein with Proteinase K (Pr-K), quantified by measuring the complex of reduced iron with Ferene S: horse spleen ferritin (hoSF); human H-chain ferritin (huFH) and human L-chain ferritin (huFL).

The first observable difference is that with the bare mineral the reduction of iron started immediately with the reaction. The second observable difference

is that the minerals formed by ferroxidase (hoSF and huFH) were more quickly reduced than the minerals initially formed within the homopolymeric L-chain apoferritin. Obviously, the mineral formed within L-chain ferritin is of slightly different nature than that in the other two cases. However, the difference between those minerals is minor and may not be of critical importance for the further experiments.

In the following experiments L- and H-ferritin in their natural form were used.

In the experiments until now, the demineralization process induced by the blue light was characterized by chelating the liberated iron with ferene S. Without any chelating agent the reduced iron would be available to act as a reducing agent for a subsequent redox reaction. In contact with Cyt-c, iron may become oxidized while reducing Cyt-c.

Blue light is able to reduce the mineral but not Cyt-c. This was confirmed by exposing Cyt-c to blue light and characterizing the reaction kinetics (Figure 5.14). The characteristic absorption peak of the reduced form of Cyt-c at 550 nm was used to follow the reaction kinetics.

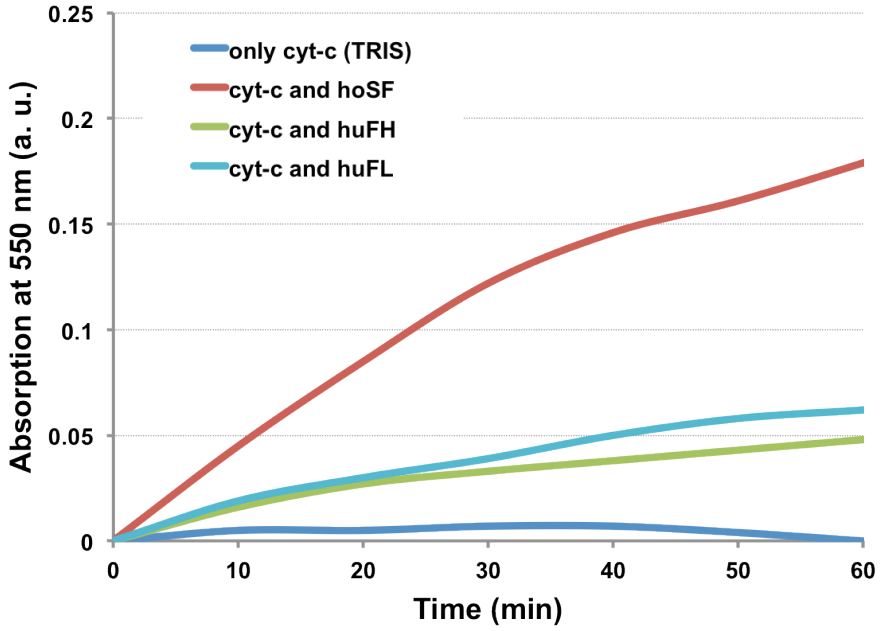

Figure 5.14. Formation of reduced Cyt-c measured from changes in the absorption at 550 nm over time. The reaction was carried out with 0.15 mg/ml protein as indicated in the legend, 10 µM oxidized Cyt-c and illumination with blue LED light.

Horse spleen ferritin showed best efficiency for reducing Cyt-c among all tested ferritins. Apparently the simultaneous presence of both L- and H-chain protein in hoSF is beneficial for reducing the mineral with light.

The light-induced reduction of Cyt-c by human L- and H-chain ferritins was considerably less efficient. Among the two ferritins, the L-chain ferritin had a slightly higher activity than the H-chain ferritin. This can be explained with the electron transport ability of L-chain proteins. Once the iron becomes oxidized, the L-chain will transport the electron across the protein shell to reduce the Cyt-c at the outer surface of the protein shell.

In contrast, H-chain ferritin did not show any evidence for electron transport properties, which would be needed to reduce the Cyt-c outside the shell in Figure 5.4. However, the Cyt-c reduction in Figure 5.14 shows similar activity to the L-chain ferritin. The reason may potentially lie in the reactive oxidative compounds that form during the reduction and re-oxidation of the iron of the mineral.

5.4 Cell culture

The previous section showed that blue light enables the reduction of the ferrihydrite mineral of ferritin. The reduced iron can be released from the protein structure and can be involved into a secondary reaction to reduce another electron acceptor. Those experimental results imply that in a biological environment light can be used to alter the cellular iron metabolism. Thus, the previously described experiments were translated to cell cultures.

For the experiments with cell cultures a setup was built, which allowed to conserve the most important cell conditions during the experiments: temperature, gas flow, atmosphere and sterile environment. The setup consists of a box with an open lateral wall were the cells can be loaded or removed. Holes in the upper part allow a better heat dissipation and temperature uniformity. All the parts or components can be easily disassembled and sterilized with ethanol or propanol and by UV irradiation.

Figure 5.15 shows a photograph of the setup with a 96 well plate for the cell cultures.

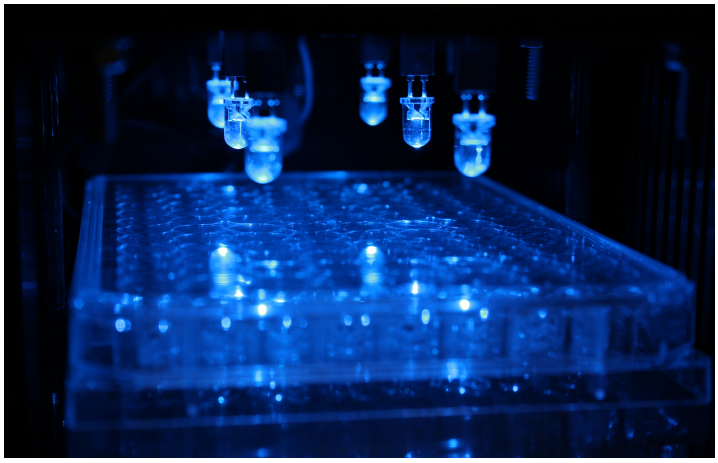

Figure 5.15. Photograph of the setup for the treatment of cells by irradiation with blue light.

Initially, the viability of the cells was quantified by comparing the survival rate of light-exposed cells to that of control cells, which did not undergo any treatment. Considering the value of the absorption obtained from the cell counting kit 8 (CCK8) for control cells being 100 %, the viability of the light-exposed cells was calculated from their absorption values (Figure 5.16). The cells were irradiated with blue light for 24, 48 and 72 h.

Two interesting observations can be made from Figure 5.16. On the one hand, upon shorter irradiation the viability of irradiated cells is higher than that of the control cells, although not significantly. On the other hand, extended irradiation induces the opposite effect. After 48 and 72 h exposure to blue light, the viability of the cells decreased seriously by in 20 and 40 %, respectively.

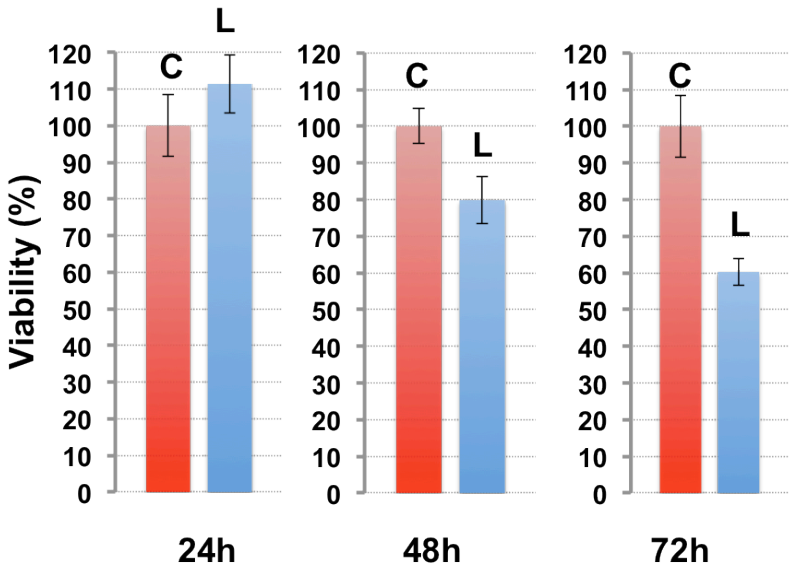

Figure 5.16. Cell viability values obtained from the Cell Counting Kit 8 (CCK-8). Red bars show the reference values of the control cells (C) and blue bars the corresponding values of cells irradiated with blue light (L). The exposure to blue light lasted for 24; 48 and 72 h.

The initial increase in viability points towards an initial enhancement of the cellular activity induced by the excess of free and available iron. However, prolonged exposure to light may induce the formation of ROS as result of the excess available Fe^{2+} and in this way lower the cell viability.

Light reduces the iron from the ferritin mineral and makes it available for the cells. In presence of excess iron, the cells tend to store it and save it for later use. The abundance of Fe^{2+} will require a higher production of H-chain apoferritin to decrease the Fe^{2+} levels and avoid the ROS production and oxidative stress. Therefore, the western blotting technique was applied to analyze the amount of H-chain subunits in irradiation-treated cells and control cells (Figure 5.17).

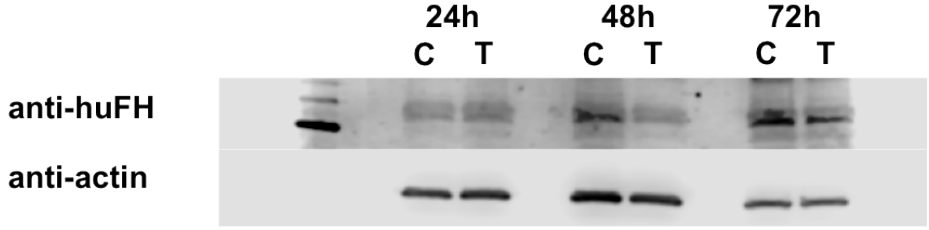

Figure 5.17. Western blot of Caco-2 cells anti-huFH and anti-actin as a protein loading control. Control (C) and treated (T) cells after exposure to blue light for 24, 48 and 72 h.

The western test clearly shows a decrease in the amount of human H-chain ferritin detected in the cells after exposure to light. After 24 h, no significant difference to the control cells is seen, but after extension to 48 and 72 h, the difference in the content of H-chain subunits in treated and control cells became apparent. In normal conditions, the amount of H-chain proteins will increase over time. Both the control and treated cells confirm this trend, but with a great difference in quantity.

Upon demineralization and enhanced release of Fe^{2+}, the cells should respond with enhanced production of H-chain proteins, which is not observed. On the contrary, the amount of the H-chain protein is decreasing with extended exposure to light. Thus, a possible damage caused by excess Fe^{2+} can be assumed. Most likely the larger amount of released iron caused an enhanced production of ROS. Those species will cause oxidative stress in the cells, negatively affecting the cellular metabolism. This can be a crucial factor for the decrease of the cell viability.

An observation related to that, but from a different perspective, was recently published by Nakashima Y. et al [156]. In their work, an enhanced ROS production induced by blue light is claimed to promote skin aging. Mitochondria are considered to be the responsible production sites of the damaging ROS, although further details were not investigated or disclosed. Mitochondria also contain ferritin, the mitochondrial ferritin, which may be the original source for the iron as catalyst for the ROS production, giving rise to the speculation that the work of Nakashima Y. et al. and the present investigation have some relation to each other.

5.5 Summary

The initial experiments in this chapter show that the electron transport is a specific function of the L-chain protein of ferritin and the first identified function of this type of protein. The results are of great importance and seriously contribute to the understanding of the biological functions of the L-chain in ferritin. Two protein subunits with distinct and complementary functionality

provide organisms flexibility for organ-specific adjustments of ferritin to meet the varying requirements and supply of iron. As shown in the aforementioned results, the iron mineralization capacity of ferritin can be adjusted simply by changing the ratio of the two subunits within the molecule. This may be one important reason for the co-existence of the ferroxidase-inactive L-chain protein and the ferroxidase-active H-chain proteins in mammals. In this light, the previously described observation of only few L-chain proteins being sufficient for altering the capacity of the ferritin for iron incorporation becomes meaningful [136,142].

The electron transport across the protein shell as a specific functionality of the L-chain protein was another piece of the puzzle for understanding the biological and medical significance of the ferritin subunits. The biological role of this protein seems to be important, since a decreased L-chain level or L/H-ratio has been observed in Parkinson's and Alzheimer diseases [157]. However, further and more detailed investigations of the transfer mechanism through the L-chain will be needed from the biochemical and biotechnical perspectives [158].

A bidirectional electron transport was demonstrated with the demineralization of the ferritin mineral by applying reducing agents. Electron donor molecules were used to reduce the iron in the mineral and release it from the ferritin cavity.

By selecting large reducing agents, a diffusion of those molecules into the ferritin cavity was hindered and the electron transport through the protein enforced. Another way for demineralization of the core uses irradiation with light. The effect of irradiation of ferritin with blue light was investigated in detail with a variety of ferritin types.

Finally, the effect of the blue light on cells was investigated, which resulted in an initial enhancement of the cell viability after the first 24 h of illumination and a significant decrease in viability after 48-72 h.

Chapter 6

Conclusions and Future work

In this thesis, the enzyme mimetic activities of natural ferritin and synthetic ferritin-based hybrid compounds were investigated. The three main parts (chapters 3, 4 and 5) of the thesis showed different approaches towards studying the properties from different perspectives. In chapter 3 the catalytic properties were in focus, describing the encapsulation of nanoparticles, their catalytic activity and the inhibition of catalytic reactions. Chapter 4 was related to biomineralization, investigating the ferroxidase activity of the hybrid compounds and their application in cell cultures. The focus of chapter 5 was on the intrinsic properties of the ferritin proteins, specifically the intrinsic properties of the L-chain protein.

In the fist part platinum nanoparticles were grown within ferritin (Pt-apo) and the resulting hybrid composite and its stability was confirmed by native gel and TEM and UV-Vis spectroscopy. The catalase and SOD mimicking activities of the hybrid compound were investigated with and without presence of inhibitors. It was found that NaN_3 could inhibit the catalase activity of Pt-apo, but not the SOD activity. In contrast, 3AT was able to inhibit both reactions. This knowledge enables to selectively inhibit one reaction without affecting the other. Furthermore, the inhibited activities can be recovered simply with the use of reducing agents, which will recover the nanoparticle surface. This was proven by XPS. This process can be adapted to further nanoparticles, which opens the possibility to detoxify intoxicated catalytic surfaces.

In close relation to the mentioned catalytic activity, in the second part the catalase activity of gold nanoparticles in presence of Hg^{2+} ions was investigated. It was found that mercury could activate the otherwise not present catalase activity of Au-apo or Au nanoparticles. Further experiments with Au films showed that mercury interacts with the gold surface, making the hydrogen peroxide decomposition reaction possible. An explanation based on a reduction of Hg^{2+} was postulated. Most likely Hg^{2+} becomes reduced Hg^{+}, which in presence of Cl^{-} precipitates as Hg_2Cl_2, but in addition disproportions to Hg^{2+} and Hg^{0}, which with gold forms a catalytically reactive amalgam.

Besides the catalase and SOD activities, a further activity of Pt-apo, the ferroxidase activity, was investigated. Once encapsulated within pure L-chain ferritin, which naturally does not show ferroxidase activity, platinum nanoparticles induce such activity. The activity and its influence on the iron homeostasis after incorporation of the composites into cells were characterized. Iron regulation is crucial for life and the possibility to adjust the iron regulation with materials that can substitute natural enzymes may have great promise for a variety of future therapies.

The foreseen applications of hybrid bioinorganic nanoparticles in the industrial production of chemicals, sensing or biomedical application are directly related to their catalytic activity. The possibility to control the activity by inhibitors and the recovery of the catalytic activity open a wide range of opportunities for industrial or biomedical processes.

In the last part the properties of the protein shell were investigated. Specifically, the intrinsic electron transport ability of the L-chain protein was identified, which was never observed before. The characterization was based on two spatially separated, but coupled reactions. An iron oxidation was performed inside the cavity of ferritin, while a reduction of cytochrome c took place outside of the ferritin at the same time. Given that the ferritin shell separated the reactions, a proceeding redox reaction is a direct evidence of the transport of electrons. While with H-chain proteins only minor reactivity was observed, with L-chain ferritin the reduction of Cytochrome c was rapid and nearly quantitative. This evidence may induce further research,

particularly towards identifying the reason why the two types of proteins are present in various tissues and why the ratio between L and H chain proteins in the body can vary between various tissues and organs.

As a last investigation, the impact of light on the demineralization of the ferrihydrite mineral inside ferritin was characterized. For this purpose, ferritin was illuminated with light of various wavelengths, which showed that the most energetic blue light was most efficient for reducing iron from the mineral. Resulting from this, it can be inferred that light can interfere into the iron homeostasis as well. If transferred to cells, the cell viability will suffer with light illumination. The experiments have shown that amount of cells after 48-72 hours of exposure to blue light was 20-30% less. Although it is not yet clear what is the determining factor for the cell death, this study may be a first step towards inducing intracellular processes and the starting point for establishing novel and controlled light therapies.

List of abbreviations

(3AT) 3-amino-1,2,4-triazole
(AAS) Atomic Absorption Spectroscopy
(AFM) Atomic force microscopy
(apo-hoSF) horse Spleen apoferritin
(apo-huFH) recombinant human Heavy-chain apoferritin
(apo-huFL) recombinant human Light-chain apoferritin
(APP) b-amyloid protein precursor
(Au-apo) Gold nanoparticle encapsulated within apoferritin
(Au-huFL) gold nanoparticle encapsulated within L-chain apoferritin
(BSA) Bovine Serum Albumin
(CCK-8) Cell Counting Kit-8
(Cyt-c) Cytochrome C
(DFO) Deferoxamine
(DNA) Deoxyribonucleic acid
(EDX) Energy-dispersive X-ray spectroscopy
(FBS) Fetal Bovine Serum
(Ferene S) 3-(2-Pyridyl)-5,6-di(2-furyl)-1,2,4-triazine-5′,5″-disulfonic acid disodium salt
(FMN) Flavin mononucleotide
(H-chain) Heavy-chain subunit
(hoSF) horse Spleen Ferritin
(huFH) recombinant human Heavy-chain Ferritin
(huFL) recombinant human Light-chain Ferritin,
(ICP-MS) Inductively coupled plasma mass spectrometry
(L-chain) Light-chain subunit
(LEDs) Light Emitting Diodes
(MES) 2-(N-morpholino)ethanesulfonic acid
(MRI) Magnetic Resonance Imaging
(MWCO) Molecular Weight Cut-Off

(NADH) Nicotinamida Adenine dinucleotide

(kDa) Kilo Dalton

($KAuCl_4$) Potassium gold(III) chloride

(K_2PtCl_4) Potassium platinum (II) chloride

(PAGE) Polyacrylamide gel electrophoresis

(PBS) Phosphate-Buffered Saline

(PMMA) Poly(methyl methacrylate)

(Pt-apo) Platinum nanoparticle encapsulated within apoferritin

(Pt-huFH) Platinum nanoparticle encapsulated within H-chain apoferritin

(Pt-huFL) Platinum nanoparticle encapsulated within L-chain apoferritin

(PtAu-apo) Platinium-gold bimetal nanoparticle encapsulated within apoferritin

(PVDF) Polyvinylidene fluoride

(ROS) Reactive Oxygen Species

(RSC) Royal Society of Chemistry

(RT) Room Temperature

(SD) Standard Desviation

(SDS-PAGE) Sodium dodecyl sulphate-polyacrylamide gel electrophoresis

(SEM) Scanning Electron Microscopy

(SOD) Superoxide Dismutase

(TBST) 25 mM Tris HCl pH 7.5; 150 mM NaCl; 0.05% Tween 20

(TEM) Transmission Electron Microscopy

(TMB) 3, 3´, 5, 5´-tetramethylbenzidine

(Trf) Transferrin

(TfR) Transferrin Receptor

(UV-Vis) Ultraviolet-Visible

(WST-1) Dojido`s water-soluble tetrazolium salt

(XO) Xylenol Orange

(XPS) X-Ray Photoelectron Spectroscopy

Bibliography

1. Whitesides, G. M. Self-Assembly at All Scales. *Science* **295,** 2418–2421 (2002).
2. Cha, S.-H. *et al.* Shape-Dependent Biomimetic Inhibition of Enzyme by Nanoparticles and Their Antibacterial Activity. *ACS Nano* **9,** 9097–9105 (2015).
3. Lee, J. H. *et al.* Biomimetic sensor design. *Nanoscale* **7,** 18379–18391 (2015).
4. Yang, M. *et al.* Self-assembly of nanoparticles into biomimetic capsid-like nanoshells. *Nat Chem* **9,** 287–294 (2017).
5. Bhattacharya, P., Du, D. & Lin, Y. Bioinspired nanoscale materials for biomedical and energy applications. *J. R. Soc. Interface* **11,** 20131067–20131067 (2014).
6. Doll, T. A. P. F. *et al*. Nanoscale assemblies and their biomedical applications. *J. R. Soc. Interface* **10,** 20120740–20120740 (2013).
7. Gerrard, J. A. in *Protein Nanotechnology*. Humana Press, **996,** 1–15 (2013).
8. Uchida, M. *et al.* Biological Containers: Protein Cages as Multifunctional Nanoplatforms. *Adv. Mater.* **19,** 1025–1042 (2007).
9. Murray, C. B., Kagan, C. R. & Bawendi, M. G. Synthesis and Characterization of Monodisperse Nanocrystals and Close-Packed Nanocrystal Assemblies. *Annu. Rev. Mater. Sci.* **30,** 545–610 (2000).

10. Yoo, J.-W. *et al*. Bio-inspired, bioengineered and biomimetic drug delivery carriers. *Nat. Rev. Drug Discov.* **10,** 521–535 (2011).

11. Yan, F. *et al*. Apoferritin protein cages: a novel drug nanocarrier for photodynamic therapy. *Chem. Commun.* 4579 (2008).

12. Bhushan, B. *et al.* Ferritin nanocages: a novel platform for biomedical applications. *J. Biomed. Nanotechnol.* **10,** 2950–2976 (2014).

13. Korendovych, I. V. & DeGrado, W. F. Catalytic efficiency of designed catalytic proteins. *Curr. Opin. Struct. Biol.* **27,** 113–121 (2014).

14. Jayasundara, D. R. *et al.* Carbohydrate Coatings via Aryldiazonium Chemistry for Surface Biomimicry. *Chem. Mater.* **25,** 4122–4128 (2013).

15. *Carbohydrate nanotechnology*. Wiley (2016).

16. Pinheiro, A. V. *et al*. Challenges and opportunities for structural DNA nanotechnology. *Nat. Nanotechnol.* **6,** 763–772 (2011).

17. Tay, C. Y., Yuan, L. & Leong, D. T. Nature-Inspired DNA Nanosensor for Real-Time *in Situ* Detection of mRNA in Living Cells. *ACS Nano* **9,** 5609–5617 (2015).

18. Li, D. *et al.* Catalytic Hairpin Assembly Actuated DNA Nanotweezer for Logic Gate Building and Sensitive Enzyme-Free Biosensing of MicroRNAs. *Anal. Chem.* **88,** 7500–7506 (2016).

19. Metals in chemical biology. *Nat. Chem. Biol.* **4,** 143–143 (2008).

20. Berg JM, Tymoczko JL, Stryer L. Biochemistry. 5th edition. New York: W H Freeman; Section 10.2, Hemoglobin Transpo. (2002)

21. Lodish H, *et al*. Molecular Cell Biology. 4th edition. New York: W. H. Freeman Section 15.8, (2000).

22. Allo, B. A., Costa, D. O., Dixon, S. J., Mequanint, K. & Rizkalla, A. S. Bioactive and Biodegradable Nanocomposites and Hybrid Biomaterials for Bone Regeneration. *J. Funct. Biomater.* **3,** 432–463 (2012).

23. Adapted from: https://en.wikipedia.org/wiki/Lipid#/media/File:Phospholipids_aqueous_solution_structures.svg (2017/04/21).

24. https://en.wikipedia.org/wiki/Liposome#/media/File:Liposome.jpg (2017/04/21).

25. Adapted from: https://en.wikipedia.org/wiki/Polysaccharide#/media/File:Glycogen_structure.svg (2017/04/21).

26. https://en.wikipedia.org/wiki/Polysaccharide#/media/File:Cellulose-Ibeta-from-xtal-2002-3D-balls.png.(2017/04/21).

27. McArdle, W. D., Katch, F. I. & Katch, V. L. *Exercise physiology: energy, nutrition, and human performance*. Lippincott Williams & Wilkins, (2007).

28. Adapted from: https://en.wikipedia.org/wiki/Protein#/media/File:Myoglobin.png. (2017/04/22).

29. Adapted from: https://en.wikipedia.org/wiki/Protein#/media/File:Myoglobin.png. (2017/04/22).

30. Adapted from: https://commons.wikimedia.org/wiki/DNA#/media/File:DNA_chemical_structure.svg. (2017/05/03) Image of Madeleine Price Bal.

31. Adapted from: http://www.publicdomainpictures.net/view-image.php?image=42718&picture=dna (2017/05/03).

32. Berg JM, Tymoczko JL, Stryer L. Biochemistry. 5th edition. New York: W H Freeman; (2002)

33. Alberts, B. *et al*. Molecular Biology of the Cell. 4th edition. New York: Garland Science; (2002)

34. Harrison, P. M. & Arosio, P. The ferritins: molecular properties, iron storage function and cellular regulation. *Biochim. Biophys. Acta BBA-Bioenerg.* **1275,** 161–203 (1996).

35. Ford, G. C. *et al.* Ferritin: Design and Formation of an Iron-Storage Molecule. *Philos. Trans. R. Soc. B Biol. Sci.* **304,** 551–565 (1984).

36. Arosio, P. & Levi, S. Ferritin, iron homeostasis, and oxidative damage. *Free Radic. Biol. Med.* **33,** 457–463 (2002).

37. Zhang, L. & Knez, M. Spherical nanoscale protein templates for biomedical applications: A review on ferritin. *J.of Nanoscience Letters*, **2**: 6 (2011).

38. Boyd, D. *et al*. Structural and functional relationships of human ferritin H and L chains deduced from cDNA clones. *J. Biol. Chem.* **260,** 11755–11761 (1985).

39. Levi, S. *et al.* Mechanism of ferritin iron uptake: activity of the H-chain and deletion mapping of the ferro-oxidase site. A study of iron uptake and ferro-oxidase activity of human liver, recombinant H-chain ferritins, and of two H-chain deletion mutants. *J. Biol. Chem.* **263,** 18086–18092 (1988).

40. Wade, V. J. *et al.* Influence of site-directed modifications on the formation of iron cores in ferritin. *J. Mol. Biol.* **221,** 1443–1452 (1991).

41. Hempstead, P. D. *et al.* Comparison of the three-dimensional structures of recombinant human H and horse L ferritins at high resolution. *J. Mol. Biol.* **268,** 424–448 (1997).

42. Harrison, P. M. & Arosio, P. The ferritins: molecular properties, iron storage function and cellular regulation. *Biochim. Biophys. Acta* **1275,** 161–203 (1996).

43. Andrews, S. C., Robinson, A. K. & Rodríguez-Quiñones, F. Bacterial iron homeostasis. *FEMS Microbiol. Rev.* **27,** 215–237 (2003).

44. Mackenzie, E. L., Iwasaki, K. & Tsuji, Y. Intracellular Iron Transport and Storage: From Molecular Mechanisms to Health Implications. *Antioxid. Redox Signal.* **10,** 997–1030 (2008).

45. Curtin, J. F., Donovan, M. & Cotter, T. G. Regulation and measurement of oxidative stress in apoptosis. *J. Immunol. Methods* **265,** 49–72 (2002).

46. Gunshin, H. Cybrd1 (duodenal cytochrome b) is not necessary for dietary iron absorption in mice. *Blood* **106,** 2879–2883 (2005).

47. Hentze, M. W., Muckenthaler, M. U. & Andrews, N. C. Balancing acts: molecular control of mammalian iron metabolism. *Cell* **117,** 285–297 (2004).

48. Wang, J. & Pantopoulos, K. Regulation of cellular iron metabolism. *Biochem. J.* **434,** 365–381 (2011).

49. Dunn, L. L., Rahmanto, Y. S. & Richardson, D. R. Iron uptake and metabolism in the new millennium. *Trends Cell Biol.* **17,** 93–100 (2007).

50. Aisen, P., Wessling-Resnick, M. & Leibold, E. A. Iron metabolism. *Curr. Opin. Chem. Biol.* **3,** 200–206 (1999).

51. Kwok, J. C. & Richardson, D. R. The iron metabolism of neoplastic cells: alterations that facilitate proliferation? *Crit. Rev. Oncol. Hematol.* **42,** 65–78 (2002).

52. Cheng, Y. *et al*. Structure of the human transferrin receptor-transferrin complex. *Cell* **116,** 565–576 (2004).

53. Macedo, M. F. & de Sousa, M. Transferrin and the transferrin receptor: of magic bullets and other concerns. *Inflamm. Allergy Drug Targets* **7,** 41–52 (2008).

54. Aisen, P. Transferrin receptor 1. *Int. J. Biochem. Cell Biol.* **36,** 2137–2143 (2004).

55. Donovan, A. *et al.* The iron exporter ferroportin/Slc40a1 is essential for iron homeostasis. *Cell Metab.* **1,** 191–200 (2005).

56. Ward, D. M. & Kaplan, J. Ferroportin-mediated iron transport: Expression and regulation. *Biochim. Biophys. Acta BBA - Mol. Cell Res.* **1823,** 1426–1433 (2012).

57. Richardson, D. R. *et al.* Mitochondrial iron trafficking and the integration of iron metabolism between the mitochondrion and cytosol. *Proc. Natl. Acad. Sci.* **107,** 10775–10782 (2010).

58. Mann, S., Bannister, J. V. & Williams, R. J. Structure and composition of ferritin cores isolated from human spleen, limpet (Patella vulgata) hemolymph and bacterial (Pseudomonas aeruginosa) cells. *J. Mol. Biol.* **188,** 225–232 (1986).

59. Liu, X. & Theil, E. C. Ferritins: Dynamic Management of Biological Iron and Oxygen Chemistry. *Acc. Chem. Res.* **38,** 167–175 (2005).

60. Douglas, T. & Ripoll, D. R. Calculated electrostatic gradients in recombinant human H-chain ferritin. *Protein Sci.* **7,** 1083–1091 (1998).

61. Bou-Abdallah, F. *et al*. Defining metal ion inhibitor interactions with recombinant human H- and L-chain ferritins and site-directed variants: an isothermal titration calorimetry study. *J. Biol. Inorg. Chem. JBIC Publ. Soc. Biol. Inorg. Chem.* **8,** 489–497 (2003).

62. Bou-Abdallah, F. *et al.* Facilitated Diffusion of Iron(II) and Dioxygen Substrates into Human H-Chain Ferritin. A Fluorescence and Absorbance Study Employing the Ferroxidase Center Substitution Y34W. *J. Am. Chem. Soc.* **130,** 17801–17811 (2008).

63. Xu, B. & Chasteen, N. D. Iron oxidation chemistry in ferritin. Increasing Fe/O2 stoichiometry during core formation. *J. Biol. Chem.* **266,** 19965–19970 (1991).

64. Treffry, A. *et al*. How the presence of three iron binding sites affects the iron storage function of the ferritin (EcFtnA) of *Escherichia coli*. *FEBS Lett.* **432,** 213–218 (1998).

65. Bauminger, E. R. & Bauminger, E. R. Ferritin, the Path of Iron into the Core, as Seen by Mössbauer Spectroscopy. *Hyperfine Interact.* **151/152,** 3–19 (2003).

66. Zhao, G. *et al.* Multiple pathways for mineral core formation in mammalian apoferritin. The role of hydrogen peroxide. *Biochemistry (Mosc.)* **42,** 3142–3150 (2003).

67. Watt, R. K., Hilton, R. J. & Graff, D. M. Oxido-reduction is not the only mechanism allowing ions to traverse the ferritin protein shell. *Biochim. Biophys. Acta BBA - Gen. Subj.* **1800,** 745–759 (2010).

68. Calò, A. *et al*. Nanoscale device architectures derived from biological assemblies: The case of tobacco mosaic virus and (apo)ferritin. *Jpn. J. Appl. Phys.* **55,** 03DA01 (2016).

69. Li, L., Zhang, L. & Knez, M. Comparison of two endogenous delivery agents in cancer therapy: Exosomes and ferritin. *Pharmacol. Res.* **110,** 1–9 (2016).

70. He, D. & Marles-Wright, J. Ferritin family proteins and their use in bionanotechnology. *New Biotechnol.* **32,** 651–657 (2015).

71. Jutz, G. *et al*. Ferritin: A Versatile Building Block for Bionanotechnology. *Chem. Rev.* **115,** 1653–1701 (2015).

72. Kramer, R. M. *et al*. Engineered Protein Cages for Nanomaterial Synthesis. *J. Am. Chem. Soc.* **126,** 13282–13286 (2004).

73. Domínguez-Vera, J. M. *et al.* Size-Controlled Water-Soluble Ag Nanoparticles. *Eur. J. Inorg. Chem.* **2007,** 4823–4826 (2007).

74. Takagi, D. *et al.* Gold-filled apo-ferritin for investigation of single-walled carbon nanotube growth on substrate. *Chem. Phys. Lett.* **445,** 213–216 (2007).

75. Okuda, M. *et al.* Self-Organized Inorganic Nanoparticle Arrays on Protein Lattices. *Nano Lett.* **5,** 991–993 (2005).

76. Iwahori, K. & Yamashita, I. Size-controlled one-pot synthesis of fluorescent cadmium sulfide semiconductor nanoparticles in an apoferritin cavity. *Nanotechnology* **19,** 495601 (2008).

77. Zhang, L. *et al.* H-Chain Ferritin: A Natural Nuclei Targeting and Bioactive Delivery Nanovector. *Adv. Healthc. Mater.* **4,** 1305–1310 (2015).

78. Bain, J. & Staniland, S. S. Bioinspired nanoreactors for the biomineralisation of metallic-based nanoparticles for nanomedicine. *Phys Chem Chem Phys* **17,** 15508–15521 (2015).

79. Meldrum, F. C. *et al*. Synthesis of inorganic nanophase materials in supramolecular protein cages. *Nature* **349,** 684–687 (1991).

80. Kalgaonkar, S. & Lönnerdal, B. Receptor-mediated uptake of ferritin-bound iron by human intestinal Caco-2 cells. *J. Nutr. Biochem.* **20,** 304–311 (2009).

81. Bretscher, M. S. & Thomson, J. N. Distribution of ferritin receptors and coated pits on giant HeLa cells. *EMBO J.* **2,** 599–603 (1983).

82. Zhang, L. *et al.* Receptor-Mediated Cellular Uptake of Nanoparticles: A Switchable Delivery System. *Small* **7,** 1538–1541 (2011).

83. Mazzucchelli, S. *et al.* Nanometronomic treatment of 4T1 breast cancer with nanocaged doxorubicin prevents drug resistance and circumvents cardiotoxicity. *Oncotarget* (2017).

84. Li, L. *et al.* Ferritin-mediated siRNA delivery and gene silencing in human tumor and primary cells. *Biomaterials* **98,** 143–151 (2016).

85. Klem, M. T. *et al.* Synthetic Control over Magnetic Moment and Exchange Bias in All-Oxide Materials Encapsulated within a Spherical Protein Cage. *J. Am. Chem. Soc.* **129,** 197–201 (2007).

86. Zhang, B. *et al.* Kinetic and Thermodynamic Characterization of the Cobalt and Manganese Oxyhydroxide Cores Formed in Horse Spleen Ferritin. *Inorg. Chem.* **44,** 3738–3745 (2005).

87. Aime, S., Frullano, L. & Geninatti Crich, S. Compartmentalization of a Gadolinium Complex in the Apoferritin Cavity: A Route To Obtain High

Relaxivity Contrast Agents for Magnetic Resonance Imaging. *Angew. Chem. Int. Ed.* **41,** 1017–1019 (2002).

88. Pan, D., Schmieder, A. H., Wickline, S. A. & Lanza, G. M. Manganese-based MRI contrast agents: past, present, and future. *Tetrahedron* **67,** 8431–8444 (2011).

89. Ceolín, M., Gálvez, N. & Domínguez-Vera, J. M. Thermal induced phase transitions and structural relaxation in apoferritin encapsulated copper nanoparticles. *Phys. Chem. Chem. Phys.* **10,** 4327 (2008).

90. Fan, R. *et al*. Fabrication of Gold Nanoparticles Inside Unmodified Horse Spleen Apoferritin. *Small* **6,** 1483–1487 (2010).

91. Abe, S. *et al.* Control of the Coordination Structure of Organometallic Palladium Complexes in an apo-Ferritin Cage. *J. Am. Chem. Soc.* **130,** 10512–10514 (2008).

92. Suzuki, M. *et al.* Preparation and catalytic reaction of Au/Pd bimetallic nanoparticles in Apo-ferritin. *Chem. Commun.* 4871 (2009).

93. Liu, X. *et al.* Apoferritin–CeO_2 nano-truffle that has excellent artificial redox enzyme activity. *Chem Commun* **48,** 3155–3157 (2012).

94. Fan, J. *et al.* Direct evidence for catalase and peroxidase activities of ferritin-platinum nanoparticles. *Biomaterials* **32,** 1611–8 (2011).

95. Zhang, L. *et al.* Reducing stress on cells with apoferritin-encapsulated platinum nanoparticles. *Nano Lett.* **10,** 219–23 (2010).

96. Gay, C., Collins, J. & Gebicki, J. M. Determination of Iron in Solutions with the Ferric–Xylenol Orange Complex. *Anal. Biochem.* **273,** 143–148 (1999).

97. Domazou, A. S. *et al.* The kinetics of the reaction of nitrogen dioxide with iron(II)- and iron(III) cytochrome c. *Free Radic. Biol. Med.* **69,** 172–180 (2014).

98. Smith, F. E. *et al*. Serum iron determination using ferene triazine. *Clin. Biochem.* **17,** 306–310 (1984).

99. McLellan, T. Electrophoresis buffers for polyacrylamide gels at various pH. *Anal. Biochem.* **126,** 94–99 (1982).

100. Carmona, U. *et al.* Tuning, inhibiting and restoring the enzyme mimetic activities of Pt–apoferritin. *Chem. Commun.* **50,** 701 (2014).

101. Hu, X. *et al.* Research progress of nanoparticles as enzyme mimetics. *Sci. China Phys. Mech. Astron.* **54,** 1749–1756 (2011).

102. Wei, H. & Wang, E. Nanomaterials with enzyme-like characteristics (nanozymes): next-generation artificial enzymes. *Chem. Soc. Rev.* **42,** 6060 (2013).

103. Moreno-Mañas, M. & Pleixats, R. Formation of Carbon−Carbon Bonds under Catalysis by Transition-Metal Nanoparticles. *Acc. Chem. Res.* **36,** 638–643 (2003).

104. Astruc, D., Lu, F. & Aranzaes, J. R. Nanoparticles as Recyclable Catalysts: The Frontier between Homogeneous and Heterogeneous Catalysis. *Angew. Chem. Int. Ed.* **44,** 7852–7872 (2005).

105. Liu, J. *et al.* Au@Pt core/shell nanorods with peroxidase- and ascorbate oxidase-like activities for improved detection of glucose. *Sens. Actuators B Chem.* **166–167,** 708–714 (2012).

106. Doctrow, S. R. *et al*. Salen Mn Complexes are Superoxide Dismutase/Catalase Mimetics that Protect the Mitochondria.

107. Liu, X. *et al.* Apoferritin-camouflaged Pt nanoparticles: surface effects on cellular uptake and cytotoxicity. *J. Mater. Chem.* **21,** 7105 (2011).

108. Yang, Y. *et al*. Purification and characterization of a new laccase from Shiraia sp.SUPER-H168. *Process Biochem.* **48,** 351–357 (2013).

109. Carmona U. Functional Modification of Apoferritin for Catalysis and Drug Delivery. Master Thesis (2013) .

110. Sies, H. Oxidative stress: from basic research to clinical application. *Am. J. Med.* **91,** 31S–38S (1991).

111. Vajda, S. *et al.* Subnanometre platinum clusters as highly active and selective catalysts for the oxidative dehydrogenation of propane. *Nat. Mater.* **8,** 213–216 (2009).

112. Hentze, M. W. *et al.* A cis-acting element is necessary and sufficient for translational regulation of human ferritin expression in response to iron. *Proc. Natl. Acad. Sci. U. S. A.* **84,** 6730–6734 (1987).

113. Koppenol, W. H. Reactions involving singlet oxygen and the superoxide anion. *Nature* **262,** 420–421 (1976).

114. Hall, R. D. & Chignell, C. F. Steady-state near-infrared detection of singlet molecular oxygen: a stern-volmer quenching experiment with sodium azide. *Photochem. Photobiol.* **45,** 459–464 (1987).

115. Liu, J. *et al.* Screening of inhibitors for oxidase mimics of Au@Pt nanorods by catalytic oxidation of OPD. *Chem. Commun.* **47,** 10981 (2011).

116. Mummey, M. J. & Schmidt, L. D. Decomposition of NO on clean Pt near atmospheric pressures. *Surf. Sci.* **109,** 29–42 (1981).

117. Stamenkovic, V. *et al.* Changing the Activity of Electrocatalysts for Oxygen Reduction by Tuning the Surface Electronic Structure. *Angew. Chem. Int. Ed.* **45,** 2897–2901 (2006).

118. Yan, L. *et al.* Fluorescent sensing of mercury(ii) based on formation of catalytic gold nanoparticles. *The Analyst* **138,** 4280 (2013).

119. Jiang, X. *et al*. Peroxidase-like activity of apoferritin paired gold clusters for glucose detection. *Biosens. Bioelectron.* **64,** 165–170 (2015).

120. Long, Y. J. *et al.* Visual observation of the mercury-stimulated peroxidase mimetic activity of gold nanoparticles. *Chem. Commun.* **47,** 11939 (2011).

121. Schopf, C. *et al*. Investigation of Au–Hg amalgam formation on substrate-immobilized individual Au nanorods. *J Mater Chem C* **3,** 8865–8872 (2015).

122. Taylor & Francis. *Biogeochemical cycles of elements*. (2005).

123. Tseng, C.-W. *et al*. Detection of mercury ions based on mercury-induced switching of enzyme-like activity of platinum/gold nanoparticles. *Nanoscale* **4,** 6823 (2012).

124. Sennuga, A., van Marwijk, J. & Whiteley, C. G. Multiple fold increase in activity of ferroxidase–apoferritin complex by silver and gold nanoparticles. *Nanomedicine Nanotechnol. Biol. Med.* **9,** 185–193 (2013).

125. Sennuga, A., van Marwijk, J. & Whiteley, C. G. Ferroxidase activity of apoferritin is increased in the presence of platinum nanoparticles. *Nanotechnology* **23,** 35102 (2012).

126. Douglas, R. *et al*. Recurrent excitation in neocortical circuits. *Science* **269,** 981–985 (1995).

127. Li, L. *et al*. Semi-artificial and bioactive ferroxidase with nanoparticles as the active sites. *Chem. Commun.* **50,** 8021 (2014).

128. Liehr, J. G. & Jones, J. S. Role of iron in estrogen-induced cancer. *Curr. Med. Chem.* **8,** 839–849 (2001).

129. Fernandez-Real, J. M., Lopez-Bermejo, A. & Ricart, W. Cross-Talk Between Iron Metabolism and Diabetes. *Diabetes* **51,** 2348–2354 (2002).

130. Cherukuri, S. *et al.* Unexpected role of ceruloplasmin in intestinal iron absorption. *Cell Metab.* **2,** 309–319 (2005).

131. Olivieri, S. *et al.* Ceruloplasmin Oxidation, a Feature of Parkinson's Disease CSF, Inhibits Ferroxidase Activity and Promotes Cellular Iron Retention. *J. Neurosci.* **31,** 18568–18577 (2011).

132. Duce, J. A. *et al.* Iron-Export Ferroxidase Activity of β-Amyloid Precursor Protein Is Inhibited by Zinc in Alzheimer's Disease. *Cell* **142,** 857–867 (2010).

133. Theil, E. C., Behera, R. K. & Tosha, T. Ferritins for Chemistry and for Life. *Coord. Chem. Rev.* **257,** 579–586 (2013).

134. Pfaffen, S. *et al*. Mechanism of Ferrous Iron Binding and Oxidation by Ferritin from a Pennate Diatom. *J. Biol. Chem.* **288,** 14917–14925 (2013).

135. Bou-Abdallah, F. *et al*. The Putative 'Nucleation Site' in Human H-Chain Ferritin Is Not Required for Mineralization of the Iron Core †. *Biochemistry (Mosc.)* **43,** 4332–4337 (2004).

136. Baraibar, M. A. *et al*. A mutant light-chain ferritin that causes neurodegeneration has enhanced propensity toward oxidative damage. *Free Radic. Biol. Med.* **52,** 1692–1697 (2012).

137. Zhao, G. *et al*. Is Hydrogen Peroxide Produced during Iron(II) Oxidation in Mammalian Apoferritins? †. *Biochemistry (Mosc.)* **40,** 10832–10838 (2001).

138. Tsuji, Y. *et al.* Coordinate Transcriptional and Translational Regulation of Ferritin in Response to Oxidative Stress. *Mol. Cell. Biol.* **20,** 5818–5827 (2000).

139. Pietsch, E. C. Nrf2 Mediates the Induction of Ferritin H in Response to Xenobiotics and Cancer Chemopreventive Dithiolethiones. *J. Biol. Chem.* **278,** 2361–2369 (2003).

140. Tallkvist, J., Bowlus, C. L. & Lönnerdal, B. Functional and molecular responses of human intestinal Caco-2 cells to iron treatment. *Am. J. Clin. Nutr.* **72,** 770–775 (2000).

141. Carmona, U. *et al*. Ferritin light-chain subunits: key elements for the electron transfer across the protein cage. *Chem Commun* **50,** 15358–15361 (2014).

142. Luscieti, S. *et al.* Mutant Ferritin L-chains That Cause Neurodegeneration Act in a Dominant-negative Manner to Reduce Ferritin Iron Incorporation. *J. Biol. Chem.* **285,** 11948–11957 (2010).

143. St. Pierre, T. G. *et al.* Organ-specific crystalline structures of ferritin cores in?-thalassemia/hemoglobin E. *Biol. Met.* **4,** 162–165 (1991).

144. Santambrogio, P. *et al.* Production and characterization of recombinant heteropolymers of human ferritin H and L chains. *J. Biol. Chem.* **268,** 12744–12748 (1993).

145. Van Gelder, B. F. & Slater, E. C. The extinction coefficient of cytochrome c. *Biochim. Biophys. Acta* **58,** 593–595 (1962).

146. McCord, J. M. & Fridovich, I. Superoxide dismutase. An enzymic function for erythrocuprein (hemocuprein). *J. Biol. Chem.* **244,** 6049–6055 (1969).

147. Vandewalle, P. L. & Petersen, N. O. Oxidation of reduced cytochrome *c* by hydrogen peroxide: Implications for Superoxide assays. *FEBS Lett.* **210,** 195–198 (1987).

148. Ukeda, H. *et al.* Spectrophotometric Assay of Superoxide Anion Formed in Maillard Reaction Based on Highly Water-soluble Tetrazolium Salt. *Anal. Sci.* **18,** 1151–1154 (2002).

149. Tosha, T. *et al.* Ferritin Protein Nanocage Ion Channels: Gating by n-terminal extensions. *J. Biol. Chem.* **287,** 13016–13025 (2012).

150. Petrucci, O. D. *et al*. A ferritin mediated photochemical method to synthesize biocompatible catalytically active gold nanoparticles: size control synthesis for small (~2 nm), medium (~7 nm) or large (~17 nm) nanoparticles. *RSC Adv* **4,** 3472–3481 (2014).

151. Watt, R. K., Petrucci, O. D. & Smith, T. Ferritin as a model for developing 3rd generation nano architecture organic/inorganic hybrid photo catalysts for energy conversion. *Catal. Sci. Technol.* **3,** 3103 (2013).

152. Keyes, J. D. *et al*. Ferritin as a photocatalyst and scaffold for gold nanoparticle synthesis. *J. Nanoparticle Res.* **13,** 2563–2575 (2011).

153. Nikandrov, V. V. *et al*. Light induced redox reactions involving mammalian ferritin as photocatalyst. *J. Photochem. Photobiol. B* **41,** 83–89 (1997).

154. Saenz, N. *et al.* Insights on the (Auto)Photocatalysis of Ferritin. *Inorg. Chem.* **55,** 6047–6050 (2016).

155. Welch, K. D., Davis, T. Z. & Aust, S. D. Iron Autoxidation and Free Radical Generation: Effects of Buffers, Ligands, and Chelators. *Arch. Biochem. Biophys.* **397,** 360–369 (2002).

156. Nakashima, Y., Ohta, S. & Wolf, A. M. Blue light-induced oxidative stress in live skin. *Free Radic. Biol. Med.* **108,** 300–310 (2017).

157. Friedman, A. *et al*. Ferritin as an important player in neurodegeneration. *Parkinsonism Relat. Disord.* **17,** 423–430 (2011).

158. Glover, S. D. *et al.* Photochemical Tyrosine Oxidation in the Structurally Well-Defined α_3 Y Protein: Proton-Coupled Electron Transfer and a Long-Lived Tyrosine Radical. *J. Am. Chem. Soc.* **136,** 14039–14051 (2014).

Cover figure is an adapted figure from:

Rose, AS. *et al*. *Web-based molecular graphics for large complexes.* ACM Proceedings of the 21st International Conference on Web3D Technology (Web3D '16): 185-186, (2016).
AS Rose and PW Hildebrand. *NGL Viewer: a web application for molecular visualization.* Nucl Acids Res (1 July 2015) 43 (W1): W576-W579 (2015).

List of publications

Ferritin-Mediated siRNA Delivery and Gene Silencing in Human Tumor and Primary Cells. Li L, Muñoz-Culla M, **Carmona U**, Lopez MP, Yang F, Trigueros C, Otaegui D, Zhang L, Knez M. *Biomaterials* **(2016)** 98. 143-151

H-Chain Ferritin: A Natural Nuclei Targeting and Bioactive Delivery Nanovector. Zhang L, Li L, Di Penta A, **Carmona U**, Yang F, Schöps R, Brandsch M, Zugaza JL, Knez M. *Advance Healthcare Materials* **(2015)** 4. 1305–1310

Synthesis, molecular docking and design of Tetrahydroquinolines as acetylcholinesterase inhibitors. Gutiérrez M, Arévalo B, Martínez G, Valdés F, Vallejos G, **Carmona U** and San Martin A. *Journal of Chemical and Pharmaceutical Research* **(2015)** 7. 351-358

Ferritin light-chain subunits: key elements for the electron transfer across the protein cage. **Carmona U**, Li L, Zhang L, Knez M. *Chemical Communications* **(2014)** 50. 15358-15361

Semi-artificial and bioactive ferroxidase with nanoparticles as the active sites. Li L, Zhang L, **Carmona U**, Knez M. *Chemical Communications* **(2014)** 50. 8021-8023

Tuning, inhibiting and restoring the enzyme mimetic activities of Pt–apoferritin. **Carmona U**, Zhang L, Li L, Münchgesang W, Pippel E, Knez M. *Chemical Communications* **(2014)** 50. 701-703

Antifungal Activity of Tetrahydroquinolines against Some Phytopathogenic Fungi. Gutiérrez M, **Carmona U**, Vallejos G, Astudillo L. *Z. Naturforsch* **(2012)** 67. 551-556

Acknowledgements

There are many people I would like to acknowledge for their help and support during the realization of this work.

First of all, I am thankful to my supervisor, Prof. Dr. Mato Knez, for both his kindness and professionality. I am very grateful to him for having given me the opportunity to perform a summer internship in the group back in 2012, which enabled me to realize a master thesis, and finally a PhD thesis. You are a great supervisor. I really enjoyed the time in the group, even though there were hard times (Science is like that!). I do not regret anything. You taught me a lot about science: how to do it, how to think, etc. Your support was essential to reach this point. It was always a pleasure to discuss with you scientific issues. You were always very helpful.

I would also like to thank Dr. Lianbing Zhang for being so knowledgeable and helpful. I learnt all the secrets about how to operate in the lab from you. You were patient with me, helped me in each of the crucial steps in this project, and the most important thing, you introduced me into the fascinating world of ferritin - this nanometric ball that sometimes drives me crazy!

I would also like to mention Dr. Le Li. Many experiments with cell cultures would have been impossible to perform without your help. You had the patience to teach a “chemist” how to work with cells. Thanks a lot for that!

Thanks to Mikel Beltrán, for solving all kinds of “technical problems” both inside and outside the lab. Hasierako harreratik laguntzeko prest egon zarelako, laborategi barruan eta baita laborategitik kanpo ere. Zuk eskatu bezala euskaraz idatzita, eskerrik asko guztiagatik. I am also grateful to Dr. Fan Yang for these 5 years in the Nanomaterials lab. I will always remember our collaborations and the “Chinese lessons” on Friday afternoons. Together we had a great time.

Your patient and support were essential to me; Ana Zuzuarregi and Itxasne Azpitarte, thanks a lot to both of you. Zuei ere ez dakit nola eskertu eskeinitako laguntasun guztia. Taldekide izan gara baina zuek eskainitako babesa haratago doa, nire asperraldiko txapak aguantatu dituzue, eta benetan biharra nuenean lagundu didazue.

I am also grateful to past and present members of the Nanomaterials group; Dr. Nagore Ibarra, Weike Wang, Sarai Garcia, Dr. Ana Beloqui, Dr. Jaime DuMont, Dr. Keith Gregorczyk. Thanks for creating this nice working environment. It was nice to discuss with you, to help each other. I think the great environment that we have in the group makes everything much easier.

Besides, I would like to thank Prof. Dr. Davide Prosperi and his people from the NanoBioLab at the University Milano-Bicocca in Italy for such an interesting stay. Especially, I would like to mention and thank Chiara Tullio. You helped me a lot, introduced me to the NanoBioLab, showed me Milano and taught me Italian. Grazie mile!!!

Back in nanoGUNE, I would like to thank all nanopeople community that I met during these years. I really had a great time with all the nice people I met. It was a pleasure to share nice moments with you all, such as “hamaiketako-s” or lunch times. Eskerrik Asko!!!

Azkenik, bost urte hauetan, nanoGUNEtik kanpo baina uneoro nire alboan egon diren pertsona guzti horiei eskertu nahi diet. Nere guraso, Ixiar eta Pepini, Itsaso, arrebiai eta gainerako familixiari, nik baino gehixau prozesu honetan sinistu eta aurrera etaraten lagundu doztazuelako. Kuadrilako lagunairi, erdi abandonauta euki arren Oñatira bueltaitten nintzan bakoitzian esku-zabalik hartzen ninduzuelako. Ezin ahaztu Donostiako lagunartia, zuek izan zai nere buruko minak kentzeko erremeixorik onenak (espero zuei pasau ez izana). Azkenik Maddi zuri, nere eguneroko gora-behera danak aguantaittiakin nahiko ez eta bajoi momentutan motibau eta aurrera itten lagundu doztazulako.

Eskerrik asko danoi benetan!!!